



University
of Glasgow

Marco, Bigatti (2015) *Quantitative studies of the structure and chemistry of materials at the nano- and atomic-scale*. PhD thesis.

<http://theses.gla.ac.uk/6393/>

Copyright and moral rights for this thesis are retained by the author

A copy can be downloaded for personal non-commercial research or study, without prior permission or charge

This thesis cannot be reproduced or quoted extensively from without first obtaining permission in writing from the Author

The content must not be changed in any way or sold commercially in any format or medium without the formal permission of the Author

When referring to this work, full bibliographic details including the author, title, awarding institution and date of the thesis must be given

Quantitative Studies of the Structure and Chemistry
of Materials at the Nano- and Atomic-Scale

Marco Bigatti

Submitted in fulfilment of the requirements for the
PhD in Physics

School of Physics and Astronomy
College of Science and Engineering
University of Glasgow

May 2015

Abstract

In this thesis electron microscopy was employed to characterise the nanoscale and atomic scale structure and chemistry of organic and inorganic materials.

In chapter 4, the thin film morphology of the organic blend of [poly(9,9-dioctylfluorene-co-benzothiadiazole)] (commonly referred as F8BT) and poly[9,9-dioctylfluorene-co-N-(4-butylphenyl)-diphenylamine] (abbreviated as TFB) was investigated, mainly by bright field transmission electron microscopy (BF-TEM).

F8BT and TFB are conjugated polymers, which are candidates to replace inorganic semiconductors in many applications because of their simple preparation and processing procedures. The phase separation of the F8BT:TFB blend was investigated at different compositions. Polymer domains were found in the thin film, with sub-micrometer size which varies with concentration. The 1:1 weight ratio sample showed sub-micrometer TFB rich areas in a F8BT matrix, while the 1:4 weight ratio thin film presented F8BT phases, whose areas are mostly below $0.02 \mu m^2$, in a TFB layer. Since some electronic applications, especially in optoelectronics, show increased efficiency after addition of quantum dots in the polymer blend, the effect of CdSe quantum dots on the phase separation of the organic blend was investigated together with their effect on the nanoscale morphology. The CdSe quantum dots were found to aggregate in clusters with limited dispersion within the polymer domains, which did not present significantly morphology changes as a consequence of quantum dots (QDs) addition.

The atomic structure and chemistry of the inorganic $Ba_{6-3x}Nd_{8+2x}Ti_{18}O_{54}$ microwave ceramic was quantitatively investigated in chapter 4, using high resolution scanning transmission electron microscopy (HR-STEM) and electron energy loss spectroscopy (EELS). These materials are an essential part of telecommunication systems, they can be found in components such as resonators and antennas, on account of their high permittivity, temperature stability and the very low dielectric loss at microwave frequencies. The unit cell was refined with sub-Å precision based on extensive data analysis of HR-STEM images and the unit cell structure showed no significant changes as a consequence of changes in composition or cooling rate after annealing. Ba was found to substitute preferentially to specific Nd atomic columns in the structure, and these trends apply across the whole composition range. These results were confirmed by comparisons with image simulations and provided a starting point for improved refinements of X-ray data.

Contents

1	Introduction	18
1.1	Relevance of morphology study and nanocharacterisation	18
1.2	Inorganic-Organic Blends	19
1.2.1	Conjugated Polymers	19
1.2.2	Electroluminescence and Optoelectronic Devices	20
1.2.3	Quantum Dots in Optoelectronic Devices	22
1.3	Barium Neodymium Titanate Atomic Structure Study	23
1.3.1	Theory of Dielectrics	24
1.3.2	Physical Properties of Microwave Ceramics	26
1.3.3	Atomic Structure and Crystallography	27
1.3.4	Aim of this Work	29
2	Experimental Techniques	31
2.1	Introduction	31
2.2	Relevance of TEM in Morphology Study	31
2.3	Working Principles and Physics of Electron Microscope	32
2.3.1	Structure of TEM	32
2.3.1.1	Vacuum System	32
2.3.1.2	Electron Related Components	33
2.3.1.3	Illumination and Imaging System	37
2.3.2	Maximising Resolution of Electron Microscope	44
2.3.2.1	TEM	45
2.3.2.2	STEM	46
2.3.3	Electron Optics	47
2.4	Electron Scattering and Studying Materials in TEM and STEM	53
2.4.1	Elastic Scattering and imaging	54
2.4.1.1	Diffraction Contrast TEM Imaging	57
2.4.1.2	Mass-Thickness Contrast	57
2.4.1.3	HAADF STEM imaging	58
2.4.2	Inelastic Scattering and Spectroscopy	61
2.4.2.1	Theory of Inelastic Scattering	61
2.4.2.2	EELS	68
2.5	Conclusions	74

3	Data Analysis Methodology	75
3.1	Introduction	75
3.2	Principle of Statistical Analysis	75
3.3	Algorithms for the Quantifying Atomic Resolution Imaging and Spectroscopy	76
3.3.1	Atomic Structure Refinement from HAADF Imaging	77
3.3.1.1	Atomic Column Position Refinement	77
3.3.1.2	Elliptical Fitting of non-round Columns	86
3.3.1.3	Atomic Resolution Quantification of Column Cation Content	88
3.4	Principle of STEM Image Simulation	93
4	Atomic Structure and Chemistry of $Ba_{6-3x}Nd_{8+2x}Ti_{18}O_{54}$	96
4.1	Introduction	96
4.2	Literature Review	97
4.2.1	Physics of Microwave Dielectric	97
4.2.2	Advantages and Disadvantages of Possible Compounds	98
4.2.2.1	Relevance of $Ba_{6-3x}Nd_{8+2x}Ti_{18}O_{54}$	99
4.2.3	Applications	99
4.2.4	Crystallography	100
4.3	Structural and Chemical Model of Barium Neodymium Titanate	102
4.3.1	Atomic Structure Refinement from Atomic Resolution STEM images	103
4.3.1.1	Cations Sites	103
4.3.1.2	Elongated Sites	109
4.3.1.3	Titanium Sites	112
4.3.2	Atomic-Scale Chemical Ordering	116
4.3.2.1	Grains Chemical Ordering	116
4.3.2.2	Phase Boundary Chemical Ordering	121
4.4	Conclusions and Suggested Future Work	124
5	Morphology Study of Organic-Inorganic Compounds	126
5.1	Introduction	126
5.2	Literature Review	127
5.2.1	Reasons of Interest and Applications	127
5.2.2	Physics of Conductive Organic Materials and QDs Thin Films . . .	127
5.2.3	Relevance of CdSe QDs incorporated in F8BT:TFB	130
5.2.4	Relevance of TEM in Morphology Studies of Organic Materials . .	131
5.3	Preparation of Specimens	132
5.4	Results and Discussion	133
5.4.1	Analysis of F8BT:TFB Polymer Blend	133
5.4.2	Analysis of CdSe Quantum Dots in F8BT:TFB Polymer Blend . . .	139
5.5	Conclusions	145

6	General Conclusions and Suggested Future Work	146
6.1	General Conclusions	146
6.1.1	Atomic Structure and Chemistry of $Ba_{6-3x}Nd_{8+2x}Ti_{18}O_{54}$ Microwave Dielectric	146
6.1.1.1	Proposed Complementary Characterisation of $Ba_{6-3x}Nd_{8+2x}Ti_{18}O_{54}$	147
6.1.2	Morphology Study of Organic-Inorganic Compounds	147
6.1.2.1	Proposed Polymers-QDs Blend Characterisation Improvement	148

List of Tables

2.1	Comparison of different electron guns [69, 73]. Crossover size is the smallest diameter of the beam produced by the gun focusing field. Brightness represents the current density over a steradian.	34
2.2	Accelerating voltages, related relativistic wavelengths, and final resolution, according to Rayleigh criterion. The collection semi-angle β is considered to be 0.8°	45
2.3	List of some of the available signals in a TEM, relative techniques for analysis, and provided information.	54
2.4	List of some of the detectable edges in EELS spectroscopy, beside the related ionisation orbital. Electron is promoted from that state to the first available empty one, which generally depends on the sample (e.g. the $M_{4,5}$ edge of <i>Ba</i> corresponds to a $3d \rightarrow 4f$ transition).	67
3.1	Parameters for elemental quantification from EELS spectra in Digital Micrograph. For all these elements, the angles were set to 30 mrad for convergence semi-angle and 31mrad for the collection. Beam energy was 100 keV. The power law formula was used for background fitting, cross sections were calculated using Hartree-Slater model by Digital Micrograph. Integration range was used for both cross section σ_k and element intensity integration I_k	89
3.2	List of theoretical X-ray k_{AF_e} values for <i>Ba</i> (based L edge) and <i>Ti</i> (K edge), according to different theories [69].	92
4.1	List of some of the available MW ceramics, together with their value of $Q \times f_0$, permittivity and crystal structure [58].	98
4.2	Site symmetry operations with respect to [010] direction, for Pnma and Pna2 ₁ space groups [210].	100
4.3	Coordinates from statistical analysis of <i>Ba</i> and <i>Nd</i> cations for x=0 sample (annealing ratio 60 °C/hr).	105
4.4	Coordinates from statistical analysis of <i>Ba</i> and <i>Nd</i> cations for x=0.3 sample (annealing ratio 60 °C/hr).	105
4.5	Coordinates from statistical analysis of <i>Ba</i> and <i>Nd</i> cations for x=0.4 sample (annealing ratio 60 °C/hr).	106

4.6	Coordinates from statistical analysis of <i>Ba</i> and <i>Nd</i> cations for $x=0.5$ sample (annealing ratio 60 °C/hr).	106
4.7	Coordinates from statistical analysis of <i>Ba</i> and <i>Nd</i> cations for annealing ratio 1 °C/hr ($x=0$ composition).	107
4.8	Coordinates from elongated sites model, for annealing ratio 1 °C/hr ($x = 0$ composition), and from Tang [66]. Differences in some coordinates of <i>Ba</i> and <i>Nd</i> [2] sites are bigger because the Tang model did not include any elongation. However, there is a general similarity between the other coordinates. In addition, Tang's model corresponds to a different orientation of the cell, so the relative symmetry operations were applied to reach comparable coordinates. Standard deviation can not be estimated as precisely as in previous models, but comparison with Rivetveld X-ray refinements and Dr. Probe simulations show good match (see fig. 4.7).	111
4.9	Coordinates from statistical analysis of <i>Ti</i> sites for $x=0$ sample (1°C/hr annealing ratio).	115
4.10	<i>Ba</i> fraction in <i>Nd</i> sites. These values are plotted in fig. 4.14 and 4.16.	120
4.11	Ratios of <i>Ba</i> to <i>Ti</i> in the grains and boundary of the two samples. Possible formulas are suggested.	124
5.1	Average values of normalised brightness and relative percentages as referred to illumination in empty areas. Some examples of acquisition areas are presented in fig. 5.13. Values above 100% are due to extremely bright areas near the edge of some specimens, as a result of the Fresnel fringe.	143

List of Figures

1.1	Photon absorption and exciton creation in polymers. HOMO and LUMO orbitals correspond to the two main energy levels. When a photon with an energy bigger than the energy gap is absorbed, an electron is promoted to the LUMO level and a hole is left in the HOMO one. The bound state of the two particles is called exciton (shown as a blue ellipse).	21
1.2	Schematics of possible interaction between quantum dots and conjugated polymers, based on Bhattacharyya[35]. Energy transfer is caused by electron decay: the energy causes an excited state in the other material and can ultimately lead to a hole transition. The charge separation is the final condition in case of hole or electron transfer. Energy levels are approximated and different configurations are possible.	23
1.3	The perovskite structure of $BaTiO_3$ is shown on the left, while $Ba_{6-3x}Nd_{8+2x}Ti_{18}O_{54}$ configuration is presented on the right. In $BaTiO_3$, Titanium is inside the octahedra formed by Oxygen atoms (in red), while Barium (in green) sits in between those. The unit cell is shown on the bottom left, delimited by black lines. In the $Ba_{6-3x}Nd_{8+2x}Ti_{18}O_{54}$ structure on the right, Nd and Ti atoms are shown in orange and light blue respectively: they form a perovskite structure, as shown in the dashed rectangle. Barium (in green) presents a different arrangement. The unit cell is shown within solid black lines. Oxygen is not displayed for simplicity.	28
2.1	Schematic diagram of an electron trajectory (in blue) in a magnetic field B . z is the direction of the electron beam. The trajectory of electrons is helical, so images undergo rotation.	35
2.2	Schematic of a electromagnetic lens. The current in the coils generates a magnetic field (shown as blue dashed lines) which is concentrated in the gap of the soft Fe case, near the optical axis (the black vertical line). This field deflects the electrons, because of Lorentz's force (see eq. 2.1).	36

2.3	Schematic of Bright Field TEM illumination system, based on Willams and Carter [69]. C2 lens is switched off in this situation, while it is useful for different techniques. Ratio d_i/d_o represents the magnification of the electron gun probe for this illumination setting. Note that in this schematic demagnification setting is reported, since normally a smaller beam is preferable. Angles, such as α , are exaggerated to illustrate the effect of lenses. Typical angles are in the range of 10-100 mrad. Scan coils are not shown for simplicity.	39
2.4	Schematic diagram of STEM probe formation and scan process, based on Willams and Carter [69]. Angles are exaggerated to illustrate the effect of lenses and scan coils.	41
2.5	Schematic of Bright Field TEM imaging, based on Willams and Carter [69]. Angles are exaggerated to illustrate the effect of lenses. Typical angles are in the range of 10-100 mrad. The objective aperture is located on the back focal plane (bfp).	42
2.6	Schematic of diffraction pattern imaging, based on Willams and Carter [69]. Angles are exaggerated to illustrate the effect of lenses. Typical angles are in the range of 10-100 mrad	43
2.7	STEM probe and detectors, based on Willams and Carter [69]. The terms Bright Field, Annular Dark Field, and High Angle Annular Dark Field have been abbreviated to BF, ADF, and HAADF respectively. . .	44
2.8	Effect of spherical aberration of a lens. At focal length the rays do not converge in a single point because of spherical aberration. z is the direction of the electron beam.	47
2.9	Schematics of simplest multipole lenses. Poles are shown in red and blue, to distinguish polarity, the black lines represent the magnetic field and the central shape is the form of the beam in the lens field. Original electron beam section is circular.	49
2.10	Nion and CEOS schematics of Aberration corrected systems for STEM microscopy. Q stands for quadrupole lens, O for octupole, OL for Objective Lens, H for hexapole, TL for transfer lens. Both systems have a second set of lenses (Q3-O3-Q4 and TL2) to compensate distortions from the first ones, while they also shape the beam.	51
2.11	An example of two Ronchigrams with and without aberration correction. A central undistorted area, where aberrations are corrected, can be noticed in both images. Its size increases with aberration correction and results in better image quality. Outer zones, corresponding to higher angles, are clearly deformed because higher order aberrations come into play, as illumination angle increases. The yellow circle in the aberration corrected Ronchigram corresponds to 38.65 mrad. Courtesy of Dr. Sam McFadzean.	52

2.12	Schematic of an aperture. β is the collection angle. The electrons presenting a collection angle larger than β are blocked by the aperture: this is one of the mechanism to control the electron beam and the relative angle. Apertures can also be used to reduce aberrations related to high angles, by limiting the collection angle β	52
2.13	Some of the signals generated by interaction of an electron beam with a specimen in a TEM.	53
2.14	Huygens description of propagation of waves. The electron beam is approximated as a plane wave, while atoms act as centre of scattering and produce spherical waves (back propagation is not shown for simplicity). Wavefronts are represented in different colour according to direction and order of diffraction.	55
2.15	Schematics of Bright Field(BF) and Annular Dark Field(ADF) detector in STEM. K_p is the transverse wavevector of the illumination, K_f is the corresponding value for electrons scattered towards the detector and Q is the desired spatial frequency for the final image (see the description of eq. 2.21 for details). The range of values for these wavevectors is limited by apertures and convergence illumination. Angles are exaggerated. . .	59
2.16	EELS spectrum at low energies of a Zirconium alloy specimen. The Zero Loss Peak (ZLP) is clearly seen on the left, at 0 eV, while the <i>Zr</i> plasmon peak is located at about 17 eV. Courtesy of Kirsty Annand. .	69
2.17	An example of EELS core loss spectrum of $Ba_{6-3x}Nd_{8+2x}Ti_{18}O_{54}$. Here, <i>Ti</i> , <i>Ba</i> , and <i>Nd</i> peaks are labelled with the related EELS edges, they correspond to those used later in this work. Additional features in the 500-600 eV region were not considered but are likely due to oxygen and further titanium contribution to the spectrum.	70
2.18	EELS spectrum with background (in red) and signal (in black). Ionisation thresholds can be clearly identified, after background subtraction. .	71
2.19	HAADF image of $Ba_{4.5}Nd_9Ti_{18}O_{54}$ along [010] direction. Columns of atoms are parallel to b-axis and number of atoms in each of them is assumed to be similar, given that little thickness variation is noticeable. <i>Ba</i> and <i>Nd</i> sites are brighter and clearly visible, <i>Ti</i> can be noticed between the cations, even though it is more dim. Oxygen is not visible in this image.	74
3.1	HAADF image of a $BiFe_{0.5}Mn_{0.5}O_3$ specimen. The perovskite structure is evident and the bright Bi atoms can be distinguished from the dimmer Fe and Mn ones. Oxygen is not visible. Two precipitates can be seen in the centre of the image. Courtesy of Dr. I. MacLaren.	79
3.2	Coordinates from the fitting process on fig.3.1. Some sites were not fitted correctly, but the perovskite structure is conserved.	80

3.3	Unit cells' identification from coordinates of fig. 3.2. The wide black dots correspond to the sites of the first unit cell, which was defined by selecting individual coordinates. The other cells, which are marked by black squares, were identified by a semi-automated script.	81
3.4	Overlap of unit cells from fig. 3.3, aligned accordingly to the central bismuth site. The distribution of coordinates can be seen in the corners.	82
3.5	Slight rotations of data in fig. 3.4, in order to align the bottom sites to horizontal axis. In the left image, the same rotation was applied to all coordinates. The angle of the rotation was calculated accordingly to the average position of the sites. In the right picture, each cell was rotated by a different angle, according to the position of its bottom sites. . . .	83
3.6	Shear correction on data from fig. 3.5. In the left image, the correction was based on the average position of the sites on the left-hand side, which were (on average) vertically aligned. In the right picture, the correction aligned vertically the positions of the sites on the left-hand side in each cell.	84
3.7	a) Centre of mass calculation of the central site, from the data shown in the left image of fig. 3.6, corresponding to the "Average approach". b) Centre of mass calculation of the central site, from the data shown in the right picture in fig. 3.6, corresponding to the "Cell-Wise approach".	85
3.8	Comparison between the unit cells of each method. The main difference can be noticed in the central point. Error bars correspond to 3σ (standard deviation).	86
3.9	Zoom of HAADF acquisition of $Ba_{4.5}Nd_9Ti_{18}O_{54}$ along [010] direction. $Nd[2]$ and Ba sites elongation are marked with black and red arrows respectively, presenting a rough alignment. The sites with similar orientation are linked with dashed red line.	87
3.10	Schematics of an elongated atomic column site. The misalignment of an atom in the column result in the oblong projection, which is recorded by HAADF microscopy.	87
3.11	EELS-SI areal density image of Barium and Neodymium. The colour bar shows a considerable difference between the intensities of EELS signal of the two elements	90
3.12	EELS-SI areal density image of Neodymium in a specimen with $x = 0.5$ composition. The colour bar shows the signal intensity. The influence of specimen thickness can be easily noticed, as intensity gradually decreases from left side of the image to right side of the image.	91

3.13	First stages of image simulations. Initial electron beam (top black arrow) interacts with first slice, modelled by convolution with $Q_1(k)$, and propagates as described by $P_1(k)$. This results in a new wavefunction $\Psi_1(k)$ which undergoes the same steps with $Q_2(k)$ and $P_2(k)$. The same procedure applies iteratively for all following slices.	94
4.1	Reconstruction of $Ba_{4.5}Nd_9Ti_{18}O_{54}$ unit cell as seen from [010] b-axis. Nd , Ba and Ti sites are labelled with corresponding numbers, while oxygen sites are shown as red spheres. Barium atoms are surrounded by five titanium atoms in a roughly pentagonal shape, while Neodymium by four.	101
4.2	Reconstruction of $Ba_{4.5}Nd_9Ti_{18}O_{54}$ cations as seen from [010] c-axis. Neodymium and Barium sites are labelled with corresponding numbers. Due to symmetry considerations, in paragraph 4.3.2 $Nd[5]$ and $Nd[4]$ sites are considered equivalent to $Nd[1]$ and $Nd[3]$ respectively.	104
4.3	Plot of cations in the unit cell of $Ba_{6-3x}Nd_{8+2x}Ti_{18}O_{54}$ at various concentration (represented by value x). Distances are represented as fractions of lattice constants, which is 22.3479 Å for X and 12.2021 Å for Z respectively. Error bars correspond to 3σ	108
4.4	Plot of cations in the unit cell of $Ba_{6-3x}Nd_{8+2x}Ti_{18}O_{54}$ at various cooling rates. Distances are represented as fractions of lattice constants, which is 22.3479 Å for X and 12.2021 Å for Z respectively. Error bars correspond to 3σ	109
4.5	On the left, an example of distribution of tilt angles in Ba sites. Odd and even refer to different orientations of the tilt in the crystal structure, presented in the right image, which shows the angles of Ba sites. They are mostly oriented along two main directions, corresponding to blue and red arrows. $Nd[2]$ sites orientation are not considered in these figures, but they present a similar distinction (shown as black arrows in fig. 3.9).	110
4.6	New unit cell model for $Ba_{6-3x}Nd_{8+2x}Ti_{18}O_{54}$ with tilt in Ba and $Nd[2]$ sites, overlapped over a HAADF image. Tilt is represented as misalignment of such atoms along the [010] direction. A slight misalignment can be noticed in the bottom model cells because of drift distortions in the HAADF image.	111
4.7	Comparison of HAADF data and simulations of our model of a unit cell. a) Real HAADF data with direction of elongation of Ba and $Nd[2]$ sites. b) and c) HAADF data from a wedge specimen with increasing thickness: simulations of our model are overlapped in the white rectangles. This comparison can be used to estimate the thickness of the specimens. . .	112
4.8	Fitting results on fig. 2.19. Some sites were not fitted correctly, but the Pnma structure is conserved.	113

4.9	Perimeters identification from coordinates of fig. 4.8. The wide red dots correspond to the perimeter of the first unit cell, which was defined by selecting individual coordinates. The other perimeters, which are marked by black squares, were identified by a semi-automated script. It is worth noting the fitting process vertically mirrors the image, so the coordinates are inverted when compared to fig. 2.19 and 4.8.	114
4.10	Comparison between the unit cells from the “Average” and “Cell-Wise” approaches, based on cells identified in fig. 4.9.	115
4.11	Comparison between areal densities of Ba and Nd . Raw map on the left shows few yellow sites, where both cations are present. Ba areal density is more clear and shows its presence in Nd sites, which are labelled with dashed white circles and the corresponding number of Neodymium site (mostly $Nd[2]$ and $Nd[3]$).	116
4.12	Comparison between amount of Ba and Nd in our findings and the formula from the literature [206], $Ba_{6-3x}Nd_{8+2x}Ti_{18}O_{54}$, for different x values. All samples in this plot present a cooling ratio of 60 °C/hr. Error bars correspond to 1σ	117
4.13	Comparison between amount of Ba and Nd in our findings and the formula from the literature [206], $Ba_6Nd_8Ti_{18}O_{54}$, for different cooling ratios. All samples correspond to $x = 0$ composition, so the corresponding formula is the same for all three specimens. Error bars correspond to 1σ	117
4.14	Comparison between amount of Ba in Nd sites for the various compositions (x value comes from $Ba_{6-3x}Nd_{8+2x}Ti_{18}O_{54}$). A clear trend can be seen for both x values and Nd sites. Error bars correspond to 1σ	118
4.15	Schematic of $Ba_{4.5}Nd_9Ti_{18}O_{54}$ cations’ elemental occupation, from [010] c-axis. Ba sites (shown as green spheres) are entirely composed of Barium atoms, while Nd ones (the orange spheres) present some Ba content: a corresponding fraction of the sphere is then coloured in green. The distances between Nd and Ba sites are indicated by arrows: a bigger distance corresponds to a lower Ba content. Due to symmetry considerations, $Nd[5]$ and $Nd[4]$ sites are considered equivalent to $Nd[1]$ and $Nd[3]$ respectively.	119
4.16	Comparison between amount of Ba in Nd sites for various cooling rates. A trend can be seen for both anneal and Nd sites. Error bars correspond to 1σ	120
4.17	HAADF data from two phase boundaries analysed in this section. These images come from a $Ba_{6-3x}Nd_{8+2x}Ti_{18}O_{54}$ sample with $x = 0$ composition, annealed at 1 °C/hr.	121
4.18	EELS spectra from phase boundary and nearby grains.	122
4.19	Oxygen k-edge spectra from phase boundary and nearby grains.	122

4.20	Elemental maps of Ba, Nd, Ti and O of phase boundaries in $Ba_{6-3x}Nd_{8+2x}Ti_{18}O_{54}$ sample ($x=0, 1$ °C/hr). The investigated area correspond to a part of the grain boundary shown in fig. 4.17a.	123
5.1	Final stages of phases evolution in F8BT:TFB thin film according to Kim <i>et al.</i> [160]. The phases are formed by either local fluctuation of density (in 1:1 ratio samples) or nucleation (when components are heavily unbalanced). Solvent evaporation promotes the glass transition, which freezes the phases configuration (schematic on the left). Then <i>p</i> -xylene continues to evaporate: in presence of air, F8BT, TFB, and <i>p</i> -xylene show a coffee stain behaviour, where the F8BT concentrates at the edges in a crater-like shape. TFB forms a capping layer on top, because its surface energy is lower than that of F8BT (schematic on the right). For the same reason, the interface with the substrate is composed by TFB.	129
5.2	Schematic of OLED with quantum dots. These nanoparticles act as recombination centres for the charges, because of favourable energy levels, promoting photon emission [1].	130
5.3	Transmission electron microscopy and AFM height images of F8BT:TFB 1:1 weight ratio thin film. The AFM data are provided Dr. Kalloudis, Edinburgh University.	134
5.4	Transmission electron microscopy and AFM height images of F8BT:TFB 1:4 weight ratio thin film. The AFM data are provided Dr. Kalloudis, Edinburgh University.	134
5.5	An example of TEM image F8BT:TFB 1:1 weight ratio and corresponding phase identification by use of manual threshold (areas in red). The lower picture is a part of the upper image where the phases are more clear. Background subtraction and FFT filtering were applied on the original TEM image before the phase identification.	135
5.6	An example of AFM height image F8BT:TFB 1:1 weight ratio (courtesy of Dr. Kalloudis, Edinburgh University) and corresponding phase identification by use of manual threshold (areas in red). The corresponding surface areas are shown in fig. 5.7.	136
5.7	An example of areas' histogram of detected phases in 1:1 weight ratio sample (from AFM data in fig. 5.6). The huge quantity of small areas (i.e. the leftmost column) is due to noise in the image, while the actual areas are believed to be in the order of $0.1-0.15 \mu m^2$	137
5.8	Surface area histograms of phases in 1:1 weight ratio samples, from AFM and TEM images. Noise tends to introduce a high number of small areas (the leftmost column), which are not entirely presented. There seems to be a relevant fraction of areas below $0.2 \mu m^2$ for the TEM data and $0.25 \mu m^2$ for the AFM histogram.	138

- 5.9 Surface area histograms of phases in 1:4 weight ratio samples, from AFM and TEM images. Noise tends to introduce a high number of small areas. The average area seems to be approximately below $0.02 \mu m^2$ for the TEM data and concentrated between 0.02 and $0.05 \mu m^2$ in the AFM histogram. These values are well below those of the 1:1 ratio sample (which are in the order of $0.2 \mu m^2$). 138
- 5.10 Surface area histograms of phases in 1:4 weight ratio samples mixed with QDs, from TEM images. Noise tends to introduce a high number of small areas, but the two measures do not agree: the average area seems to be between 0.4 and $0.1 \mu m^2$ 139
- 5.11 BF-TEM image of F8BT:TFB 1:4 thin film with quantum dots. The phase-separated polymer blend domains and the segregated QDs (resembling a black cloud) are presented in the image. Three different regions (area 1, 2 and 3) in the interface of F8BT and TFB domains were studied for QD detection. 140
- 5.12 HAADF STEM images of F8BT:TFB 1:4 thin film with quantum dots. The phase-separated polymer blend domains, consisting of the dark matrix and grey areas, and the QDs (the white regions) are presented in the image. The position of the beam after the measurement is marked in the top. Image acquired by Dr. McFadzean. 141
- 5.13 BF-TEM images of a F8BT:TFB 1:4 thin film without QDs (on the left) and with QDs (on the right). Areas of investigation of F8BT, TFB and beam intensity are marked: measured F8BT phases are shown in black, TFB domains in red and empty areas in blue. The brightness of the images was normalised, as shown by the colour bar beside the images. 142
- 5.14 BF-TEM images and intensity profiles of F8BT:TFB 1:4 thin film with quantum dots (zoom of areas 1,2 and 3 from fig.5.11). Three different regions (area 1, 2 and 3) in the interface of F8BT and TFB domains were studied for QD detection. Intensity profiles were taken across the red boxes of area 1(a), area 2(b) and area 3(c). Intensities were averaged over the width of the quantum dot. Dashed white rectangles are placed above the low intensity regions of quantum dots. Their size is approximately 2nm, as expected. 144

Acknowledgement

I would like to thank my supervisor Dr. Ian MacLaren, Senior Lecturer in Physics at the University of Glasgow. His helpfulness, patience and support helped me massively, almost as much as his scientific guidance. This thesis would not have been possible without him.

I need to thank my second supervisor and head of the MCMP group Prof. Robert Stamps, for his help and advice during troubled moments of my PhD.

I am also very grateful to Dr. Michail Kalloudis, PhD at the University of Edinburgh for his collaboration and help in many aspects of my PhD, probably beyond what he first expected when we started to work together. I also want to thank his group, in particular Dr. Vasileios Koutsos, Reader at the School of Engineering, The University of Edinburgh and Dr. Paul Clegg, Senior Lecturer in the School of Physics, The University of Edinburgh.

I wish to express my appreciation to all the MCMP group for their assistance and the pleasant and joyful working environment. A special mention to the technical staff, especially Dr. Sam McFadzean, for their constant help, from the first teaching sessions to the very end of my research. I specifically want to thank my colleagues Shabir Ravji, Aaron Naden, Pedro Parreira, Ciaran Ferguson, Pablo Borys, Francisco Trindade, Scott Smith, Rair Macedo, Joanna Bobynko and Kirsty Annand for all the time together during the past years, both within and outside the department.

I also want to mention Amir Ali for his contribution to the analysis of unit cells, which was carried on during his summer project.

A special thought for all my family and my friends, which always made me feel welcome at home, no matter how much time passed since the last meeting. Equally, thanks to all my friends in Glasgow and in Scotland, especially Nico Gawronski.

Finally I want to thank Sandy Wotton and Zora Hlacova, which (in different ways) allowed me to be here, in the first place.

Author's Declaration

This thesis has been written by myself and details the research I have carried out within the MCMP group, under the supervision of Dr. Ian MacLaren, Prof. Robert Stamps and Prof. Joachim Loos in the school of Physics and Astronomy at the University of Glasgow from 2010-2014.

The work described is my own except where otherwise stated.

This thesis has not previously been submitted for a higher degree.

Chapter 1

Introduction

1.1 Relevance of morphology study and nanocharacterisation

Miniaturisation and nanotechnology have greatly increased the interest in morphology and characterisation on microscopic scale, at micrometer, nanometer, and even atomic lengths. This is essentially due to physics effects and phenomena acting on such minuscule distances and providing functionality and improved performances to technological devices. It is then necessary to investigate materials, interfaces and even entire devices on that scale, with both good resolution and in situ analysis of chemistry and structure, as all of these can be relevant for final applications. Good comprehension of morphology, elemental structure and local composition can provide essential feedback for efficiency of devices and improve means of production.

This thesis is meant to provide an insight on nanocharacterisation, focusing particularly on two different materials: an organic polymer blend mixed with quantum dots and an inorganic crystalline ceramic. These two materials require investigations on a different scale and distinct analyses, so a perception of characterisation of two separate field of research is presented here. In this introductory chapter the reasons behind this research are discussed, with details of technological and economic relevance of these materials. This also requires a brief introduction to the basic physical effects involved in the applications. In chapter 2 a fundamental description of electron microscopy is presented, in order to better understand results, challenges and scope of the analyses. Chapter 3 deals with data analysis and simulation of resulting models, in order to explain the process which led to our result and provide details to replicate our method.

Chapter 4 presents our structural and chemical studies of microwave ceramics, with atomic modelling of the material and characterisation of stoichiometry in relation with production parameters. In chapter 5 the investigation of organic blend of polymers, with and without quantum dots, is described: the morphology and interaction of the blend with the nanoparticles are examined. Finally, chapter 6 summarises the results and conclusions of this work, presenting possible follow-ups, developments and

applications of this research.

1.2 Inorganic-Organic Blends

This study is focused on polymer blends, which are a simple and effective compound characterised by interfaces on a micrometer scale. However, they need to be studied to understand the interaction of the materials and their morphology, which can be linked to performances and efficiency of real devices. Here, the focus is on different blends (1:1 and 1:4 weight ratio) of F8BT:TFB (corresponding to poly(9,9-dioctylfluorene-co-benzothiadiazole) and poly[9,9-dioctylfluorene-co-N-(4-butylphenyl)-diphenylamine]), which are electron and hole conductive polymers respectively. Their interface is crucial for the optoelectronic phenomena which make it an interesting compound for LED (Light Emitting Diode) and photovoltaic devices (see section 5.2.1).

Moreover, the introduction of inorganic nanoparticles is believed to further improve the functionality [1], so the addition of cadmium selenide (CdSe) quantum dots (QDs) in the blend is studied here to understand its effect on morphology, preparation of the material and interfaces.

Most related devices are based on thin films (about a micron thick or less) which we will investigate here: we focus on bright field electron microscopy (BFTEM) to analyse morphology on micrometer scale, together with a description of QDs distribution which require a further effort to resolve nm features.

1.2.1 Conjugated Polymers

Conjugated polymers are a new kind of conductive and semiconductor material which could replace inorganic semiconductors like silicon in a number of devices [2, 3, 4, 5, 6], as they do not require expensive production, facilities and processing, possibly at the expense of shorter durability. Their conduction is based on the bonding and antibonding p orbitals (also referred to as π and π^*) which extend along the polymer backbone and act like elongated molecular orbitals, in which charges can move [7]. Both electron and hole-transport polymers are available (called n and p-type, respectively), so they constitute an alternative to inorganic semiconductors. Moreover, preparation of such materials and related interfaces is much more simple [8] than that of inorganic semiconductors. Since their invention [9, 10] they created a growing interest for technological applications, as transistors [11, 12, 13] and integrated circuits [14, 15]. Electroluminescence effect was also detected in these materials [16], which led to optoelectronic devices, such as LEDs [7], solar cells [17, 18, 19], full colour display [20] and even lasers [21, 22, 23, 24]. Most recent results include organic memory storage devices [25], wavelength specific photodetectors [6], integrated optical detection with polymer optical fiber [26] and detection of X-ray and alpha particles [27, 28, 29, 30]. In particular, F8BT and TFB were investigated with regards to charge transport and mobility [31],

electroluminescence of F8BT nanofibers [32] and a TFB electron blocking layer in a near infrared photodetector [33]. A polymer blend of F8BT and TFB was investigated, in a research on the optimisation of green LED performances[34]. More details on the literature regarding the F8BT:TFB blend can be found in 5.2.

Even though working prototypes exist, there is a need of studying the best preparation parameters in order to optimise performances and production.

1.2.2 Electroluminescence and Optoelectronic Devices

Electroluminescence refers to emission of photons from a material as a consequence of an electrical current. It is caused by recombination of electron and hole couples (also called excitons), where the first decays from a higher band (typically the conduction band) to a lower energy level occupied by holes (such as the valence band): this is called radiative recombination. The electrical current support the phenomenon by supplying charges for recombination and photon emission (see fig. 1.1).

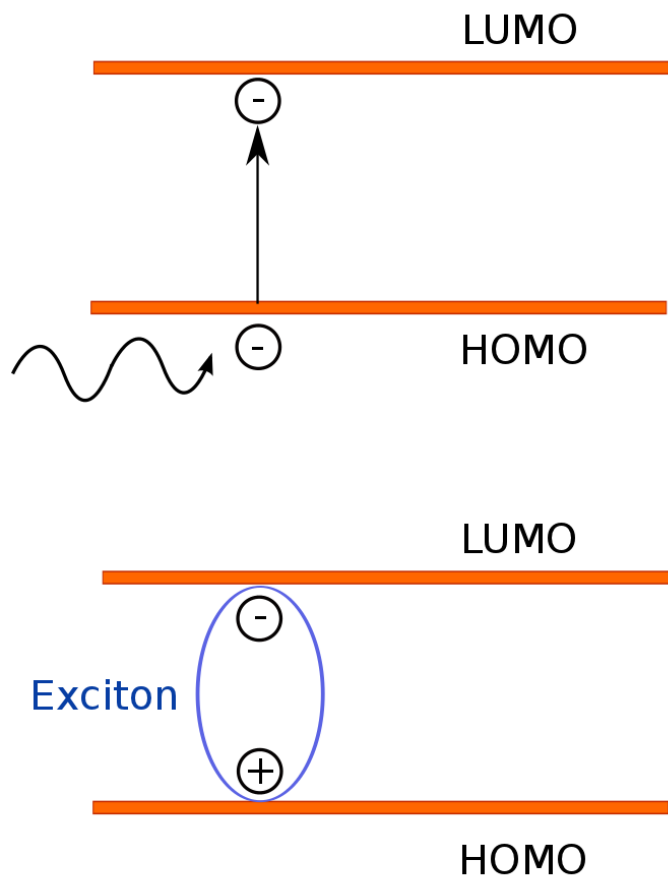


Figure 1.1: Photon absorption and exciton creation in polymers. HOMO and LUMO orbitals correspond to the two main energy levels. When a photon with an energy bigger than the energy gap is absorbed, an electron is promoted to the LUMO level and a hole is left in the HOMO one. The bound state of the two particles is called exciton (shown as a blue ellipse).

HOMO and LUMO are originated by interaction between atomic orbitals in the molecule: in the case of conjugated polymer the π and π^* orbitals overlap, forming the HOMO and LUMO wavefunctions which cause the delocalisation of electrons along the polymer [7]. Since the structure of polymers is not typically rigid, vibrations and rotation of molecules can result in changes of the energy level of orbitals, coupling between orbitals of different polymer chains is possible too, resulting in exciton migration [35]. As a consequence, the energies of the orbitals can vary, causing the range of emission wavelength to be wider than inorganic semiconductor, up to about 50-100 nm [8], with both blue [36, 37] and red tails [38, 39].

The efficiency of an optoelectronic material or device can be described by external quantum efficiency (EQE): it is the ratio of radiative recombination to the number of charge carriers, because a non-radiative process may happen as well. In fact, an

electron decay can also release energy as heat, in form of phonons. These processes are heavily influenced by the molecular orbitals of the material and by the presence of impurities or doping, which can add energy states to the band structure of the material.

The external quantum efficiency can be influenced by morphology and interfaces, as n and p-type materials need to coexist to provide electron and hole conduction respectively, while interfaces are essential for emission and absorption of photons. In the case of LEDs for example, both hole and electrons can be found at the interfaces, promoting radiative recombination and emission of photons. Alternatively, in the case of solar cells and photodetectors, a photon promotes an electron to a higher energy orbital, leaving a hole in the original level. The two charged particles form a bound state called exciton, which moves based on a diffusion behaviour. If the exciton encounters an interface it can split into the two charges, which move to the relative n and p-type material, to contribute to the current.

1.2.3 Quantum Dots in Optoelectronic Devices

Quantum dots are crystalline nanoparticles with a few nm diameter, containing about 1500 atoms [40]. They are typically composed of elements of II and VI of the periodic table such as CdSe, CdS and ZnO [41]. These nanoparticles show excitons formation, in case of interaction with photons whose energy is bigger than the energy gap of the material [41]. Since the quantum dots can be smaller than the characteristic radius of the exciton (called Bohr radius), it is considered to be confined within the quantum dots. As a result, both electron and hole, which are involved in the exciton state, are held inside the nanoparticle [42, 43]. This confinement of charges in QDs results in discrete energy levels, instead of continuous energy bands of bulk materials, causes optical and electronic properties to change [44]. For example, the energy gap is affected by the size of the quantum dot [45]: the energy gap is an important factor in optical properties, so changes in the size of QDs result in varying optical properties due to the differences in energy gaps [41]. A well known example is the different colour luminescence of quantum dots with various sizes. Another interesting optical property is the wide absorption spectrum, which is useful in solar cells, and narrow emission, to the advantage of biolabelling applications [41].

Quantum dots have beneficial effects when mixed with conjugated polymers in optoelectronic devices. For example, changes of shape or size can modify the energy band arrangement and can promote exciton splitting and energy transfer between inorganic nanoparticles and organic materials [46]. This behaviour is due to the relative alignment of energy levels between the quantum dots and the conjugated polymers. Since the size of the nanoparticles influences their energy states, the alignment can be modified by choosing an suitable diameter.

The modified energy states result in efficient energy exchange and charge transfer between quantum dots and conjugated polymer blends. The energy transfer is mediated by dipole-dipole interactions: in this process, the energy of an exciton, which is an

excited state, is transferred across the interface to the other material. This follows the relaxation of the original exciton, causing the decay of the electron to its ground state, while the transferred energy results in an excited state in the other material and the creation of an exciton[35]. This process could also lead to charge transfer, which corresponds to exciton splitting, if the energy levels are suitable. An example of these mechanisms are shown in fig. 1.2.

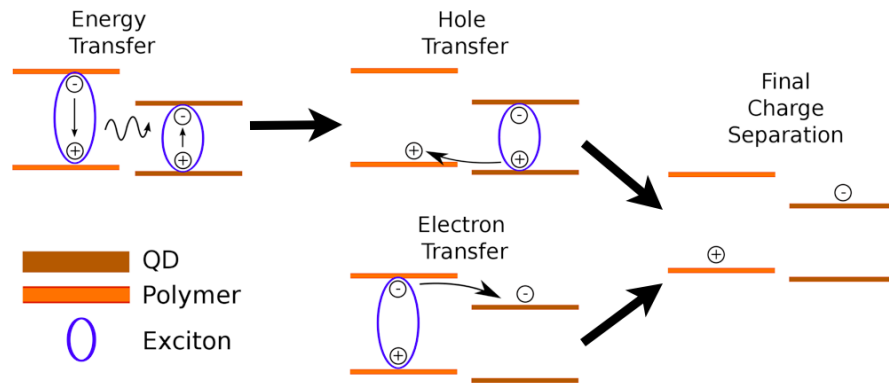


Figure 1.2: Schematics of possible interaction between quantum dots and conjugated polymers, based on Bhattacharyya[35]. Energy transfer is caused by electron decay: the energy causes an excited state in the other material and can ultimately lead to a hole transition. The charge separation is the final condition in case of hole or electron transfer. Energy levels are approximated and different configurations are possible.

The interaction of quantum dots and polymer blends resulted in many advantages: QDs were found to increase photoconductivity (increase of conductivity after illumination)[35], charge mobility between nanoparticles and properly arranged polymers [47], as well as exciton dissociation. This last effect is attributed to additional energy transfer from plasmon, which promotes the separation of excitons [35]. These improvements led to the introduction of quantum dots in many conjugated polymer devices: LED [48, 49, 50], solar cells [51, 52, 53], sensors and various biological applications [41].

1.3 Barium Neodymium Titanate Atomic Structure Study

Barium Neodymium Titanate, $Ba_{6-3x}Nd_{8+2x}Ti_{18}O_{54}$, is a microwave (MW) ceramic, which is a class of dielectric materials of great interest for telecommunication applications, especially for portable ones, such as mobile phones or wireless devices, which are the biggest drivers for this research. MW dielectric play a huge role in the diffusion and development of telecommunication devices, mobile phones in particular, and are linked

to miniaturisation. Mobile phones had a huge market expansion in the 1990s and new models became increasingly small and lightweight, while long antennas became more and more integrated inside the phone itself and did not represent a cumbersome extension anymore. This was also due to miniaturisation of MW dielectrics components which caused the global ceramics market to be worth hundreds of millions dollars [54], influenced by the diffusion of mobile phones.

The miniaturisation of important components of telecommunication equipment, such as antennas, resonators and filters, was based on the invention of the dielectric resonator [55], which allows to tune in the desired frequency, in order to communicate to the intended network or devices. This device relies on the resonance of a standing electromagnetic wave inside a small dielectric puck, shaped as cylinder or rectangle [56]. This resonator is normally few cm wide or less and the production simply requires to shape the appropriate material in the right form and size. Moreover, it is mechanically stable and there is a remarkable flexibility of the design, since small changes can modify the resonating frequency and the polarisation mode. This is necessary in order to couple such components with the rest of the devices, particularly with waveguides or transmission lines [56]. The limitations and constraints of the resonator are mostly related to the material itself: the value of permittivity at high frequency determines the size of the component, while the dielectric loss of the material limits the frequency selectivity and results in the inefficient use of bandwidth. Also, the temperature response is mainly dependent upon the material. Microwave ceramics are suitable for telecommunication application and are responsible for miniaturisation, efficiency of frequency tuning and finally the range of operating temperatures of the components, which heavily influences the performances of the entire device.

In order to understand the working principles, the properties and suitability of MW ceramics, we need to introduce some concepts from the theory of dielectrics.

1.3.1 Theory of Dielectrics

One of the most important property of dielectrics is the relative permittivity (ε_r), which describes the behaviour of the material when exposed to an electromagnetic field. In the most simple case, which is a linear dielectric without any ferroelectric polarisation, ε_r is defined as a proportionality factor between electrical displacement field D and electric field E

$$D = \varepsilon_r \varepsilon_0 E \tag{1.1}$$

where ε_0 is the vacuum permittivity equal to $8.8541878 \times 10^{-12}$ F/m [57]. However, ε_r is not constant with frequency and a more precise description requires to account for that. So in the case of a oscillating electric field

$$D_0 e^{-i\omega t} = \varepsilon_0 \varepsilon_r E_0 e^{-i\omega t} \quad (1.2)$$

where D_0 and E_0 are the amplitude of the polarisation and electric field, ω is the frequency and t is the time [57]. ε_r is then described as a complex function:

$$\varepsilon_r = \frac{D_0}{E_0} (\cos\delta + i \sin\delta) \quad (1.3)$$

where δ is the loss angle [57]. The real and imaginary parts of ε_r are significant and have specific physic equations: the first is related to propagation of the electromagnetic field, while the second represents the energy loss in the material. An alternative and common definition of permittivity is in terms of refractive index n

$$\sqrt{\varepsilon_0 \varepsilon_r} = n + ik \quad (1.4)$$

where k is the extinction coefficient [57]. The permittivity is also a function of the frequency, but we always refer to values of ε_r at about 3 GHz [58]: this is the relevant frequency (called “carrier wave”) for telecommunication devices, which are the main expected applications of $Ba_{6-3x}Nd_{8+2x}Ti_{18}O_{54}$.

Relative permittivity is also relevant for the induced polarisation density P , as it is related to susceptibility χ [57]:

$$\chi = \varepsilon_r - 1 \quad (1.5)$$

$$P = \varepsilon_0 \chi E \quad (1.6)$$

so relative permittivity can be intuitively linked to polarisation (P) of a material, which indicates some properties of perovskite structure (see 1.3.3), such as the possibility for cations to move within the unit cell as a response to electric field. This has been formalised in the Clausius-Mossotti (CM) equation, which states the dependency between permittivity, ε_r , and polarisability, α , as

$$\frac{\varepsilon_r - 1}{\varepsilon_r + 2} = \frac{4\pi}{3} \sum_j N_j \alpha_j \quad (1.7)$$

where N_j is the concentration of a given element and j refers to the various atoms in the crystal. α represents the microscopic polarisability of the dipole moment induced by electromagnetic radiation [57].

1.3.2 Physical Properties of Microwave Ceramics

The main reason behind the use of these ceramics are high relative permittivity ε_r , which is related to reduction of component size, high quality factor Q , used to select the desired frequency, and good thermal stability (τ_f) of the resonating frequency for everyday use in a reasonable range of temperature.

The high value of relative permittivity, ε_r , allows miniaturisation of resonators and filters while keeping the same working frequency f_0 , according to the following formula [58]

$$f_0 \approx \frac{c}{D\varepsilon_r^{1/2}} \quad (1.8)$$

where c is the speed of light in vacuum ($2.998 \times 10^8 m/s$), D is the diameter of the resonator.

The formula above predicts how the diameter D of a toroidal resonator can be reduced as ε_r increases, thus justifying interest in high permittivity materials: this is the principal reason for use of ceramics in these devices, as they can reach values as high as 90, in case of $Ba_{6-3x}R_{8+2x}Ti_{18}O_{54}$ [59] (R stands for suitable rare earth elements, x accounts for variations in composition).

The second essential parameter for the choice of a material for resonator is quality factor Q , which is linked to both selectivity and power loss. It represents how much the desired frequency f_0 is amplified while the rest is attenuated. An equivalent definition is the ratio between energy of f_0 and power loss. Mathematically, it can be defined in different ways

$$Q = \frac{f_0}{\Delta f} \quad (1.9)$$

or, alternatively

$$Q = 2\pi f_0 \frac{\text{energy stored}}{\text{power loss}} \quad (1.10)$$

where Δf is the range of frequency (also called bandwidth) attenuated less than 3dB when compared to f_0 , so it shows how much of the spectrum is amplified as the f_0 frequency. A similar formulation includes energy of resonating wave and corresponding loss. An alternative representation of Q is

$$Q \approx 1/\tan \delta \quad (1.11)$$

where δ is again the loss angle and its tangent represents the ratio between real and imaginary component of permittivity, which translates roughly as ratio between propagation and absorption of electromagnetic waves in the material

$$\tan \delta = \frac{\omega \text{Re}(\varepsilon) + \sigma}{\omega \text{Im}(\varepsilon)} \quad (1.12)$$

where ω is the angular frequency and σ the conductivity. Since we are dealing with dielectrics materials, σ is normally negligible.

According to theory, Q should be inversely proportional to f_0 , as shown in the following formula [60], so $Q \times f_0$ is frequently reported as a rough, frequency-independent, indication of selectivity. Its values are in the range of 10,000-300,000 [59].

$$Q \approx \left(\frac{\omega_T^2}{\gamma} \right) f^{-1} \quad (1.13)$$

where ω_T is the resonant frequency of the optical mode of phonons and γ is the damping factor. However experimental values of $Q \times f_0$ were found to decrease for increasing f , possibly because of the processing and ultimately grains size. The reason behind this is that larger grains resonate at lower frequencies and they are more likely to find defects in wider areas, while smaller ones (used for higher frequencies), are mostly defect free [58]. A more accurate parameter is the value of Q at a given frequency, i.e. 30,000 at 3GHz is a common requirement for base stations [58].

Thermal stability of resonant frequency is the last essential property required by devices, in order to tune in the desired signal over the range of temperature of everyday use. The frequency shift due to temperature needs to be few parts per million (ppm), typically less than $\pm 2 \text{ppm}/^\circ\text{C}$, and to compensate thermal expansion of the device. The temperature coefficient for frequency is defined as [58]

$$\tau_f = - \left(\frac{1}{2} \tau_\varepsilon + \alpha_L \right) \quad (1.14)$$

where τ_ε is the temperature coefficient of permittivity and α_L is the linear expansion coefficient of the material.

1.3.3 Atomic Structure and Crystallography

The microwave dielectrics often present a perovskite structure (e.g. SrTiO_3) or, at least, a partial resemblance: these are called complex perovskite structures[58]. The perovskite configuration is therefore relevant for these materials. The general composition is ABO_3 , where A represents one or more cations of big atomic radius while

B is the second smaller cation. For example, Ba atoms are normally in the centre of octahedra formed by the oxygen atoms, encapsulating the A cations (see fig. 1.3). The complex perovskite structures have a similar arrangement in part of their unit cells: the $Ba_{6-3x}Nd_{8+2x}Ti_{18}O_{54}$, which is a complex perovskite, presents Nd sites surrounded by TiO_6 octahedra, in a perovskite fashion. On the other hand, Ba atoms in this material show a different configuration: they are considered pentagonal sites, as each Ba column has five neighbouring Ti atoms (see fig. 1.3). More precisely, the $Ba_{6-3x}Nd_{8+2x}Ti_{18}O_{54}$ crystal is described as a tungsten-bronze structure, with an orthorhombic unit cell and $Pnma$ space group symmetries (see 4.2.4 for more details).

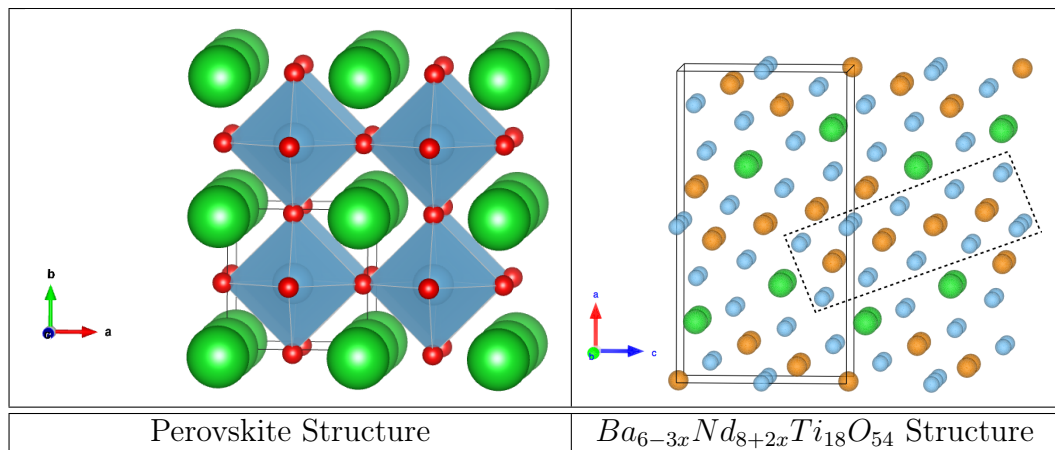


Figure 1.3: The perovskite structure of $BaTiO_3$ is shown on the left, while $Ba_{6-3x}Nd_{8+2x}Ti_{18}O_{54}$ configuration is presented on the right. In $BaTiO_3$, Titanium is inside the octahedra formed by Oxygen atoms (in red), while Barium (in green) sits in between those. The unit cell is shown on the bottom left, delimited by black lines. In the $Ba_{6-3x}Nd_{8+2x}Ti_{18}O_{54}$ structure on the right, Nd and Ti atoms are shown in orange and light blue respectively: they form a perovskite structure, as shown in the dashed rectangle. Barium (in green) presents a different arrangement. The unit cell is shown within solid black lines. Oxygen is not displayed for simplicity.

The A cation is then able to move between the octahedra and react to oscillating electromagnetic waves. This behaviour is part of the response to electric field and it can be interpreted as increased polarisation, even though it is not due to electron cloud displacement. In fact, the movement of the A cation causes ionic polarisation, where an ion is displaced similarly to the electrons' orbitals (but in the opposite direction) as a consequence of an electric field: the result is an additional adjustment of the lattice and a stronger polarisation of the material. This is valid as far as the deformation does not introduce a permanent polarisation, as in ferroelectric materials.

The configuration of sites in the crystal was related to the relevant properties of microwave dielectrics. Namely, the dielectric constant and the temperature coefficient for frequency, τ_f , were found to be proportional to the volume of the unit cell in perovskite-like materials, such as $Ba_{6-3x}R_{8+2x}Ti_{18}O_{54}$ (where R represents a rare earth element)

[61]. These results were also linked to tilt and misalignment of TiO_6 octahedra, which affect the size of the cell [61].

Many other factors are involved in the properties of ceramics, on various levels and length scales, from lattice considerations to grains sizes or even impurities [59]. In this work we mostly focused on production parameters, namely composition and annealing temperature and their effect on atomic structure. Slower annealing is known to improve cation ordering in some MW ceramics and, possibly as a consequence, the quality factor (Q) [62, 63, 64]. As a possible interpretation, the entire crystal structure has also been directly linked to intrinsic loss of dielectrics [65], formalised as oscillation damping factor γ in the following formula

$$\tan \delta = \left(\frac{\gamma}{\omega_T^2} \right) f \quad (1.15)$$

where ω_T is the resonance frequency of optical phonons, which describe the response of the lattice to electromagnetic waves. Cation ordering, or any other structural changes, then seem to affect damping, loss tangent, and Q .

Annealing effect on structure of $Ba_{6-3x}Nd_{8+2x}Ti_{18}O_{54}$ is not known, but higher degree of order was generally found to enhance selectivity [59]: investigation of a possible relation is further discussed in chapter 4.3. At the same time, cation ordering was investigated in relation to changes of composition, since substitutional Ba was consistently found in Nd sites. The role of impurities and doping was reported in literature [59], with both positive and negative effects on relevant properties: in this study, the affects of intentional and unintentional composition changes on the structure was investigated. Finally grain boundaries play a role, mostly related to trapped impurities which concentrate there. This confinement proved to be relevant and beneficial for another MW ceramic, $(Zr, Sn)TiO_4$ [59], therefore, the composition of boundaries in the specimens used in this study was also investigated.

1.3.4 Aim of this Work

Since the properties of $Ba_{6-3x}Nd_{8+2x}Ti_{18}O_{54}$ are closely related to its crystallographic structure and composition, which are investigated in this work and compared with the ongoing research on similar materials. In this current study, atomic structure and composition of barium neodymium titanate, $Ba_{6-3x}Nd_{8+2x}Ti_{18}O_{54}$, was analysed. Together, results from a previous study using X-ray diffraction [66] and a complementary description of chemistry impurities were integrated in this current study. This work was carried out on different samples, with a set of varying production parameters (composition and annealing ratio), in order to understand the influence of production on crystalline structure.

Atomic resolution data were collected for us at SUPERSTEM facility by high resol-

ution microscopy technique (see 2.4.1.3 for details) and chemical characterisation was performed together with the structural one, in order to collect a complete set of data for a precise model. Statistical treatment of data was carried out to account for the large amount of noise during the data collection and to build a new accurate model of the material as it changes its preparation conditions.

Also a new kind of 3D characterisation was introduced, in order to overcome the limitation of projection in transmission microscopy. Our conclusions were integrated and validated by X-ray diffraction refinements and simulations (see section 4.3).

Chapter 2

Experimental Techniques

2.1 Introduction

The understanding of the basic principles of electron microscopy and related techniques is essential for the comprehension of the scope of this work, the necessary steps involved in preparation of specimens and finally the interpretation of results. A first general overview of the techniques is provided in this chapter, starting with basic concepts of microscopy (section 2.3) and electron optics (section 2.3.3), followed by the theory underlying the investigation, namely elastic and inelastic electron scattering (section 2.4.1). After the presentation of such phenomena, related instruments and their working principles is described: Bright-Field TEM (section 2.4.1.1), EELS spectroscopy (section 2.4.2.2) and STEM (section 2.4.1.3). This chapter ends with the analysis of results and their interpretation for each technique. When relevant, a description of single components of the instrument is presented (section 2.3.3).

2.2 Relevance of TEM in Morphology Study

Transmission electron microscopy (TEM) is able to include different analysis techniques in a single instrument. Instrumental setups and various types of interaction between an electron beam and the specimen can be exploited to probe different characteristics. Electron elastic scattering is best suited to study the morphology of the material on different scales: Bright Field TEM (BFTEM) is based on a wide interaction of electrons over hundreds of nm or microns wide areas; scanning TEM (STEM) employs instead on a sub-nm probe which is scanned across the material for a higher spatial resolution. On the other hand, inelastic scattering allows spectroscopy studies of chemistry and stoichiometry, based on energy losses of electrons: the technique is called electron energy loss spectroscopy (EELS). These analyses are detailed later in this chapter, as they are widely used in this work. Many other characterisation methods are available, for example crystallographic or magnetic studies (diffraction pattern and Lorentz microscopy, respectively), however they are not relevant for this work.

The huge range of analyses available in TEM has led to its use in various fields

of research. One may immediately think of nanotechnology and material science, but also polymers, organic and biological samples have been studied with this technique: biology and medicine benefit hugely from TEM and it is used massively in those field of research. This capability is due to the great flexibility of TEM (and possible variants), which may provide exceptional spatial resolution for both imaging and spectroscopy. This allows the study of various characteristics of a material, for example its crystallography [67], its magnetic behaviour [68] or chemical composition [69, 70].

It is also worth mentioning the post-processing data analyses, which can directly create models from TEM data, which then integrate 3D or functional simulations.

As a result, most effects and properties which are confined in a μm or smaller scale may be effectively investigated by some form of TEM.

2.3 Working Principles and Physics of Electron Microscope

2.3.1 Structure of TEM

The structure of an electron microscope hardly resembles that of common optical microscopes because of specific requirements of electrons: first, an electron beam has to be formed and shaped with appropriate electron optics; secondly, a vacuum is necessary for the propagation of electrons towards the specimen and detectors. It also prevents electrostatic breakdown, which would be caused by the high operating voltages.

2.3.1.1 Vacuum System

The vacuum system is essential for the functioning of the electron microscope and it is based on a series of vacuum pumps and stages, in order to provide the different levels of vacuum required by the sections of the microscope. For example, a field emission electron gun (FEG) may need a pressure in the order of 10^{-9}Pa [71, 72], while the column, where the electron beam is shaped and projected on the specimen, requires approximately 10^{-7}Pa [69]. Atmospheric pressure is about 10^5Pa , so the difference is more than ten order of magnitude and it needs to be separated between following stages of increasing vacuum. In the first one, there is a pressure drop from normal atmosphere to 10^{-1}Pa (normally called rough vacuum), by means of roughing pumps. These are typically reliable rotating pumps which, unfortunately, risk to introduce some contamination because of the lubricating oil used in the moving components. They are based on a rotating element and valves which mechanically suck air in its chamber and push it out to the exterior. A second stage brings the vacuum down to the desired value, normally 10^{-7}Pa (called high vacuum): typically turbomolecular pumps are used to achieve those values, even though diffusion pumps are suitable as well. Turbomolecular pumping is based on coaxial alternated rotating and stationary blades, where the first

ones transfer momentum to gas molecules to push them towards the stationary blades, which channel them outside the pump itself. A separate second stage, still connected to roughing pumps, is used for FEG electron gun which has special vacuum requirement: $10^{-9} Pa$ (ultra high vacuum) as mentioned before. It uses some ion pumps based on a double working principle: it emits electrons which ionise gas molecules and sputter Ti atoms from a target. Ionised gas is attracted by the anode and the Ti atoms deposit on the chamber trapping more gas molecules [69].

2.3.1.2 Electron Related Components

Here the various basic components of the microscope structure are presented to show how the electron beam is created by electron guns, modified by lenses and measured by detectors. In the section 2.3.1.3 the structure and working principles of the electron microscope are presented.

Electron Guns The electron guns are the first part of the illumination system as they provide the electron beam. Their main role is to grant the desired brightness (defined as the current density over the solid angle of the electron gun) and probe size, which is further modified by the rest of the illumination system. The differences between guns are mainly due to the mechanism of electron emission, which is either thermoionic effect or field emission. Thermoionic guns generally use a sharp LaB_6 tip, because its low work function helps electron emission. If it is heated up to 1700 C° its electron have enough energy to leave the crystal. This type of gun grants good brightness and stability but the beam size is large (the initial diameter is $10\ \mu\text{m}$) and following lenses can not reduce it by large means. Therefore, electron guns are mainly used to illuminate and analyse “wide” areas of the specimen, which is suitable for BFTEM (see 2.4.1.1).

Field emission guns, on the other hand, can produce a very bright beam of smaller size so they are more suited for STEM (it was actually invented for that purpose [71, 72]), for high resolution techniques (e.g. high angle annular dark field, HAADF) and EELS spectroscopy, because they all require a tiny electron probe (see 2.4.1.3 and 2.4.2.2). They provide huge brightness of the beam, together with a sharp probe size and phase coherence. They exploit huge electrical field (in the order of 10^{10} V/m) on sharp tips to extract electrons from crystal which were previously thinned down to reduce the emission area. This is only few nm wide. Also crystal orientation is carefully chosen to increase electron yield, resulting in high phase coherence. Schottky FEG employs heating too, in order to improve electron emission, at the cost of increased source size and energy spread. Cold FEG operates at 300K and provides a source size as little as $0.7\ \text{\AA}$ [73] and results in a small energy spread, but it requires ultra-high vacuum (about $10^{-9} Pa$). A comparison of the mentioned guns is shown in table 2.1.

	LaB_6	Schottky FEG	Cold FEG
Crossover Size [nm]	10^4	15	0.07
Brightness [A/m^2sr]	5×10^{11}	5×10^{12}	10^{13}
Energy Spread [eV]	1.5	0.7	0.3
Operating Temperature [K]	1700	1700	300

Table 2.1: Comparison of different electron guns [69, 73]. Crossover size is the smallest diameter of the beam produced by the gun focusing field. Brightness represents the current density over a steradian.

In this work a LaB_6 gun was used to perform BFTEM analysis and a cold FEG was employed for STEM microscopy.

It is also worth mentioning the importance of the high-tension (HT) unit, which provides stable power supply to the electron gun. It is required to generate the extraction fields around the electron source, which helps to control the brightness and shape of the electron flux.

Electron Lenses There are many electron lenses within an electron microscope in order to manipulate the electron beam shape and convergence angle.

The preferred design of electron lenses is based on magnetic field and electromagnets, so they are conventionally called magnetic lenses. Their working principle is based on the Lorentz force, which results in an acceleration of electrons that do not travel exactly parallel to the optical axis of the microscope, along the centre of the instrument. The Lorentz force is given by:

$$\vec{F} = -e(\vec{E} + \vec{v} \times \vec{B}) \quad (2.1)$$

e is the magnitude of the charge of the electron, \vec{E} is the electric field (normally zero in an electromagnetic lens), \vec{v} is the velocity of the electron and \vec{B} is the magnetic field. The effect of this force is an acceleration perpendicular to the optical axis that leads to electrons spiralling around the centre of symmetry of the lens, with a radius r and cyclotron frequency ω_c are given by following formulas.

$$r = \frac{mv_{\perp}}{eB} \quad (2.2)$$

$$\omega_c = \frac{eB}{m} \quad (2.3)$$

where v_{\perp} is the component of velocity perpendicular to the axis, B is the absolute value of the magnetic field and m is the mass of the electron.

The trajectories of electrons in a magnetic field are helical (see fig. 2.1) so the image formed by such electrons undergoes a rotation that depends on magnetic field, which also sets the “strength” of the lens in this situation. However, rotation of image is frequently compensated automatically from inverse rotation by other lenses.

The “helical” effect is essential to influence the propagation of electrons, as they tend to spiral around the direction of the magnetic field \vec{B} . Electrons would otherwise spread without much control, away from the optical axis.

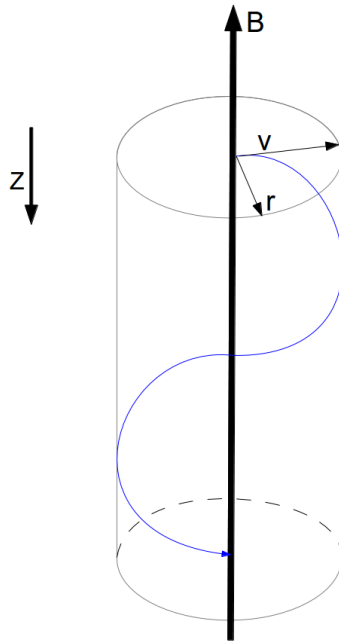


Figure 2.1: Schematic diagram of an electron trajectory (in blue) in a magnetic field B . z is the direction of the electron beam. The trajectory of electrons is helical, so images undergo rotation.

Thanks to a properly shaped magnetic field, the effect of a cylindrical magnetic lens on an electron beam is similar to that of a convex lens on light rays (see fig.2.2) in the paraxial approximation, that is for small angles, so it satisfies the thin lens equation [74]

$$\frac{1}{f} = \frac{1}{s} + \frac{1}{s'} \quad (2.4)$$

where f is the focal length, s is object distance and s' image distance.

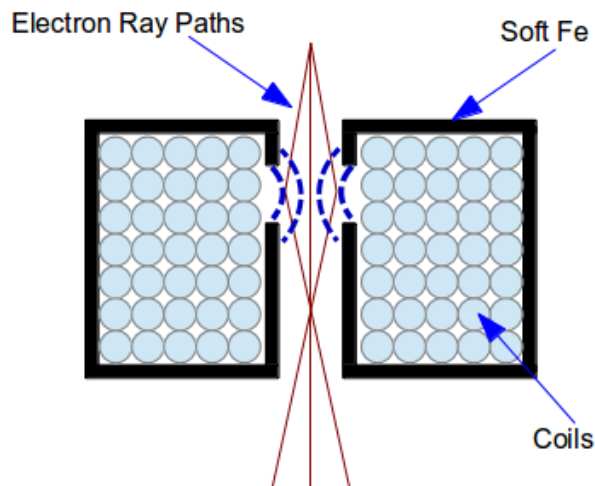


Figure 2.2: Schematic of a electromagnetic lens. The current in the coils generates a magnetic field (shown as blue dashed lines) which is concentrated in the gap of the soft Fe case, near the optical axis (the black vertical line). This field deflects the electrons, because of Lorentz’s force (see eq. 2.1).

The magnetic field in an electron lens is easily controlled by a simple change of current, which results in a change of focal length. This allows different configurations to be selected and switched in an electron microscope (e.g. change of magnification, image to diffraction mode) by changing currents in the various lenses. The magnetic hysteresis has to be considered in case of substantial change of operating conditions, because magnetic field response is not linear, so the effect of the lens on the beam could be imprecise. In fact, there is a “memory” effect in ferromagnets which counteracts the magnetisation and the linear response. It may be necessary to compensate for the residual field before setting a new value with the desired precision. Appropriate materials with low coercivity, such as soft iron, can reduce the hysteresis but this non-linearity remains, as it is an intrinsic property of ferromagnets.

Detectors Electron microscopes usually have a viewing screen to visualise the electron intensity, which relies on ZnS grains’ fluorescence. However, it is normally used for preparation of appropriate imaging conditions, while the acquisition and recording employ digital detectors, because they simplify storage and processing. These sensors are either charged-couples device (CCD), semiconductor p-n junctions or scintillators. A CCD detector is commonly found in digital cameras and it is based on transistor-like structure of metal-dielectric-semiconductor layers. A bias voltage creates a depletion region in the semiconductor, near the dielectric: when this detector is hit by a high energy electron, it creates a electron-hole couple which is separated by the bias field.

The charged particles are then collected in the semiconductor and its charge can be measured: it is proportional to energetic electrons intensity [69]. This detector is highly efficient and reliable, since it is based on well-understood semiconductor technology. It can also provide high resolution and frame rate (with the appropriate readout strategy). These detectors are the most expensive but they present good response, even to low energy electrons in a microscope.

Semiconductor junction detectors use a similar working principle, because a depletion region is employed again, either between p and n doped zones or at a metal-semiconductor interface (Schottky diode design). Again, an electron-hole couple is created and split, but its effect in this device is an increase of current, which is measured. When compared to CCD, these detectors are more noisy, insensitive to low energy electron and less reliable, but also cheaper. They use similar technology, so good resolution and frame rate can also be achieved.

Scintillators are similar to fluorescent viewing screen, since an energetic electron yields a photon by cathodoluminescence. This photon then enters in a photomultiplier and interact with a photocathode which releases a single electron, because of the photoelectric effect. This triggers the creation of more electrons from the multiplier by secondary electron emission, which results in a measurable electric signal. This structure is very sensitive to low signals, because in principle even a single electron can be detected. Scintillators have a low level of noise when compared to semiconductor detectors and exhibit a much faster time response than other detectors. However, they are less reliable than other designs [69].

All these detectors are suitable for high energy electrons, either on-axis (for BFTEM) or slightly off-axis (ADF, HAADF). STEM requires higher frame rate because it is based on sequential and fast analysis of a large number of pixel: since each acquisition requires a time in the order of μs , scintillators are preferred for STEM because of their fast response time [69]. Similarly electron spectroscopy, such as EELS, employs scintillators or CCD detectors to measure electrons, after they have been filtered according to their energies. This way, a plot of energy-dependent intensities can be created [70].

2.3.1.3 Illumination and Imaging System

The electron microscope has a complicated structure which includes many lenses and detectors for various analysis. It can be divided into two parts, the illumination and imaging one, separated by the specimen. The first forms the electron beam of the desired size, which is significantly different between the techniques, such as BFTEM and STEM.

First the electron beam is produced by the electron gun, which is meant to provide an intense and stable illumination, while the illumination system manipulates the beam to control its size and convergence angle, since different techniques require dedicated settings. BFTEM uses a convergent beam of variable size to illuminate the area of interest. A diffraction pattern (DP) ideally needs the beam and the optical axis to be

parallel to each other (see section 2.4.1.1 for details). STEM and EELS are based on smallest possible electron probe, obtained by a convergent beam. In order to fulfil these necessities, a number of lenses, scan coils and apertures are located inside the column (see fig. 2.3), beside an optional aberration corrector (see section 2.3.3). The first lenses after the gun are called condenser lenses: typically the first, called C1, modifies the size of the beam from the gun, by creating a crossover before the second lens, C2, which can help to set the convergence angle (α) of the beam. However, in fig. 2.3 the C2 lens is switched off because other lenses are usually present in the illumination system (in order to grant more flexibility), such as C3 lens, which sets the value of α . These additional lenses are necessary to switch between different illumination condition, such as BFTEM and DP, which require convergent and parallel beam respectively [69].

Another important characteristic of the illumination system is the size of the electron probe on the specimen. This is influenced by the electron gun (see par. 2.3.1.2), but the set of condenser lenses can modify its width. The magnification of a lens is defined as the ratio d_o/d_i , where d_o is the distance between the object plane and the lens, d_i is the distance between the lens and the image plane. In fig. 2.3, the magnification refers to the C3 lens: d_o is then the distance between C3 and C1, because the object plane is located on this first lens, which acts as a virtual object plane; d_i is the distance between C3 and the specimen. This particular configuration in fig. 2.3 refers to the highest demagnification possible, since a small electron probe is desirable to increase the brightness of the probe.

Magnification of the electron beam can be then modified by setting the strength of the lenses and the possibility applies to the incident angle α (see fig. 2.3). It is also relevant to note the C2 aperture helps to constrain the size of the beam and stop electrons from unwanted angles [69] (see paragraph 2.3.3 for more information about the apertures).

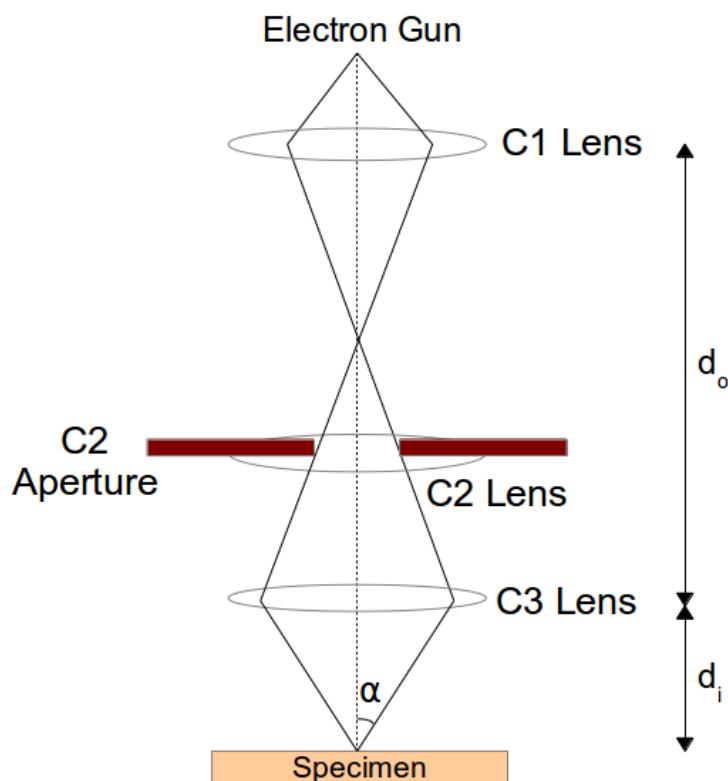


Figure 2.3: Schematic of Bright Field TEM illumination system, based on Williams and Carter [69]. C2 lens is switched off in this situation, while it is useful for different techniques. Ratio d_i/d_o represents the magnification of the electron gun probe for this illumination setting. Note that in this schematic demagnification setting is reported, since normally a smaller beam is preferable. Angles, such as α , are exaggerated to illustrate the effect of lenses. Typical angles are in the range of 10-100 mrad. Scan coils are not shown for simplicity.

An important parameter is the focus of the convergent beam: if the crossover point is on the sample, the C3 lens is focused, which corresponds to the “in focus” condition. If the crossover is beyond the specimen, the lens is underfocused (negative focus). On the contrary, if the crossover is before the sample, an overfocus is present.

Most parameters of the illumination system, such as focus, angle of convergence

and beam size are influenced by many of the lenses and aperture, so the components are ultimately controlled by a computer to provide desired values.

On the other hand, the STEM illumination system focuses on the reduction of the probe size and its raster movement across the specimen (see fig. 2.4). This setting exploits scan coils, which vary the local magnetic field to tilt the beam at a requested angle. A set of two coils can scan the beam across the specimen. In the BFTEM illumination condition the coils place the beam along the optical axis, in the centre of the column. Scanning coils are not shown in fig. 2.3 for sake of simplicity. In STEM, the C1 creates a crossover which allows C2 lens and aperture to set the collection angle of the electron probe. The scan coils raster it and C3 renders the beam parallel to the optical axis [69].

A more detailed description of the STEM techniques is presented in 2.4.1.3.

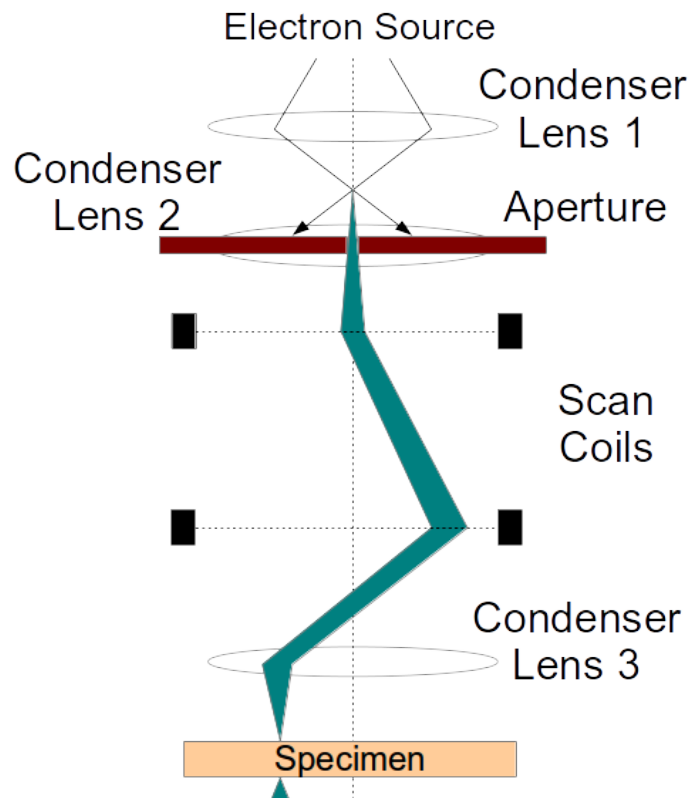


Figure 2.4: Schematic diagram of STEM probe formation and scan process, based on Willams and Carter [69]. Angles are exaggerated to illustrate the effect of lenses and scan coils.

The BFTEM imaging system magnifies the outgoing electron beam which has interacted with the specimen and focus them towards the detector (see fig. 2.5). Again, a combination of lenses and aperture can allow good flexibility of imaging conditions. Objective lens, the related aperture and the intermediate lens can change magnification and work in both image and diffraction mode (see section 2.4.1.1 for details on DP). The beam then propagates to the projector lens, for final magnification and optimisation for detectors.

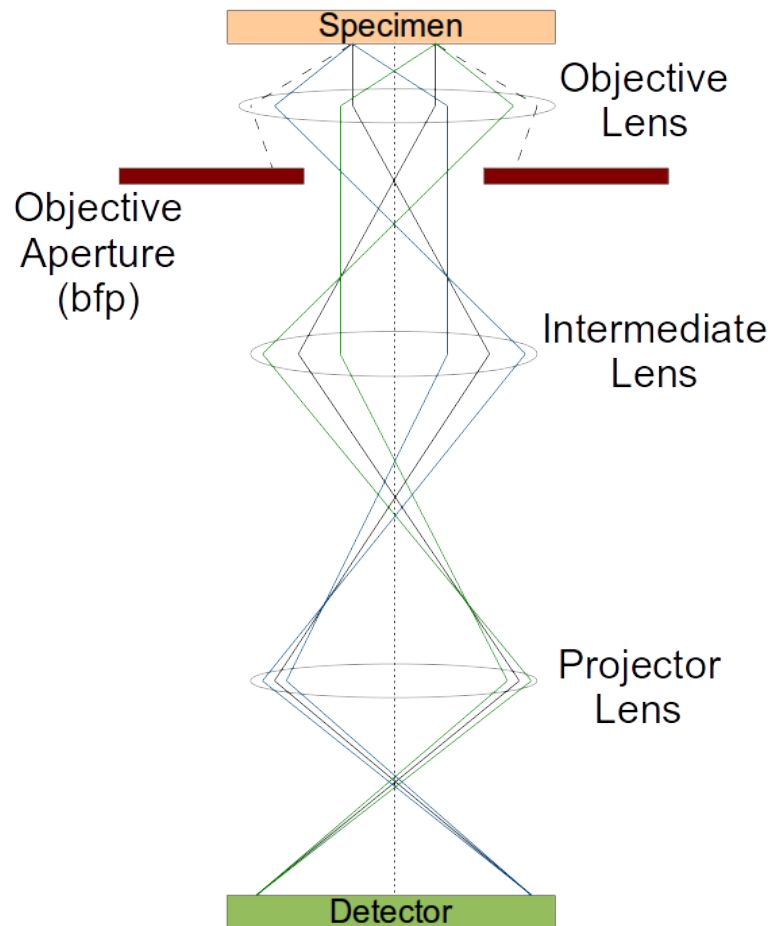


Figure 2.5: Schematic of Bright Field TEM imaging, based on Willams and Carter [69]. Angles are exaggerated to illustrate the effect of lenses. Typical angles are in the range of 10-100 mrad. The objective aperture is located on the back focal plane (bfp).

The contrast in BFTEM images is formed by difference in intensity of coherent electron waves. They are scattered by the specimen and projected in different directions, but only the electrons which pass through the sample at low angle of scattering are collected by the BFTEM detector, which is on the optical axis (see fig. 2.7). This imaging technique reflects the morphology of the sample, as well as changes in density and thickness. See section 2.4.1.1 and 2.4.1.2 for more details on contrast and 2.4.1 for a discussion on interaction between electrons and the specimen.

Another possible configuration for the imaging system is diffraction mode (see fig. 2.6), where diffraction patterns are projected on the detectors. The main difference is the strength of the intermediate lens, for which the back focal plane (bfp) now acts as a object plane in this configuration. The diffraction pattern lies on the bfp, so it is transferred to the image plane of the intermediate lens, then to the projector lens and the detector.

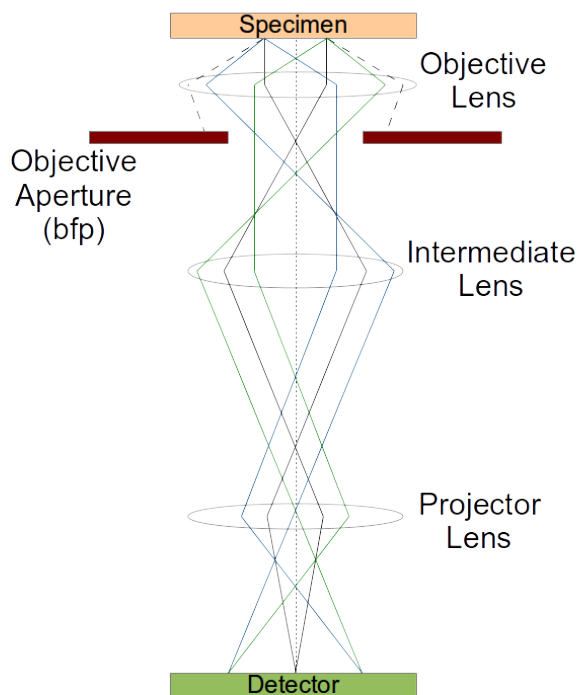


Figure 2.6: Schematic of diffraction pattern imaging, based on Willams and Carter [69]. Angles are exaggerated to illustrate the effect of lenses. Typical angles are in the range of 10-100 mrad

There are almost no lenses employed in the STEM imaging system: the electrons that exit from the specimen are collected by detectors placed below the specimen [75] (see fig. 2.7), while a post-specimen lens can simply converge the beam on the detectors. The collection angle β is relevant because different techniques are based on electrons within a given range of angles. There are dedicated detectors for each analysis, which collect electrons up to about 200mrad, such as HAADF detectors. The size of STEM investigation area corresponds to the scanning zone, the resolution depends on the size of the probe itself.

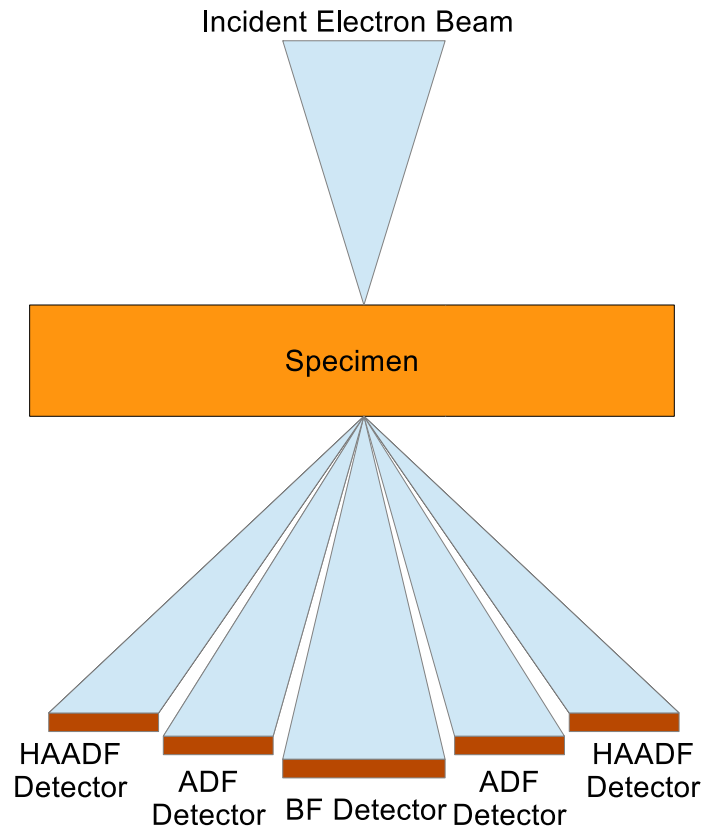


Figure 2.7: STEM probe and detectors, based on Willams and Carter [69]. The terms Bright Field, Annular Dark Field, and High Angle Annular Dark Field have been abbreviated to BF, ADF, and HAADF respectively.

2.3.2 Maximising Resolution of Electron Microscope

The main reasons for the invention of electron microscope [76] and the use of electrons in general is the improvement of resolution when compared to optical microscopy. The latter uses typically visible light, whose photons have a wavelength in the order of hundreds of nm, so any detail below that size can not be investigated properly. This was formalised with the Rayleigh criterion [77], which defines the resolution (δ) in terms of wavelength λ

$$\delta = \frac{0.61\lambda}{n\sin\beta} \quad (2.5)$$

where n is the refractive index of the viewing medium and β the semi-angle of collection of the imaging lens.

Electrons, on the other hand, have a wavelength which depend on the accelerating voltage and can then be reduced, as the voltage V and λ are almost inversely proportional, as shown in the following formula.

$$\lambda = \frac{h}{\left[2m_0eV\left(1 + \frac{eV}{2m_0v^2}\right)\right]^{1/2}} \quad (2.6)$$

where e is the charge of electron, V is the voltage applied to it, m_0 is their rest mass, v their velocity [69]. Electron wavelengths of the order of pm can be achieved, with obvious improvement of resolution (which now allows atomic imaging). For instance, a typical accelerating voltage of 100kV yields a 0.00370 nm wavelength, which can be reduced to 0.00087 nm for a 1MV (see tab. 2.2 for more details). However, electron optics problems reduce the collection angle β degrading the performances and resolution. More details are discussed in sec. 2.3.3.

2.3.2.1 TEM

As mentioned before, electron microscopes were invented to reach high resolution (δ), which is defined as the smallest distance that one can resolve. The Rayleigh criterion (see eq. 2.5) states the importance of wavelength λ , but the collection angle β has to be considered as well. In particular, $n\sin\beta$, which is called the numerical aperture or NA, represents a limiting factor: it ranges from unity or even above (in case of light microscopy) to about 0.6 in electron microscopes. This happens because of constraints of the instrument: n is always 1, the value of the vacuum, while β is normally quite small in such microscopes (of the order of 0.6-0.8°) because electron optics introduce distortion at higher angles (see 2.3.3). The resolution is then proportional to the wavelength and this justifies the use of electrons, since their wavelength depends on operating voltage of the microscope. This seems to suggest that a proper voltage would grant any desired resolution (see 2.2), so voltages in the range of 80kV-1MV are used in electron microscopes while, in this work, we used 100-200 kV for STEM and TEM respectively. However, the small value of β really worsens the final result.

Accelerating Voltage (kV)	Relativistic Wavelength (nm)	Resolution (nm) ($\beta = 0.8^\circ$)
100	0.00370	0.16165
200	0.00251	0.10966
300	0.00197	0.08607
1000	0.00087	0.03801

Table 2.2: Accelerating voltages, related relativistic wavelengths, and final resolution, according to Rayleigh criterion. The collection semi-angle β is considered to be 0.8°.

Further improvement of resolution is now mostly linked to the increase of β , which is limited by the poor quality of electron lenses. A wider collection angle would cause distortion in the electron beam and eventually degrade the quality of the results. This is caused by aberrations, a non-ideal behaviour of lenses which depends on β (among other parameters) and typically worsens when such angle increases.

2.3.2.2 STEM

A different technique used to improve resolution is Scanning TEM (STEM), which is based on creation of smallest possible electron probe to scan the area of interest, while collecting the outgoing beam. The resolution is then fixed by the size of the probe, which is the quadratic sum of three contributions[78]:

1. Source Size

$$d_s^2 = \frac{4I_{probe}}{\pi^2 Br \alpha^2} \quad (2.7)$$

where $Br = \frac{j}{\pi \alpha^2}$ (j is the current density), α the probe convergence angle, I_{probe} is the probe current.

2. Diffraction (also called Abbe Limit)

$$d_d^2 = \frac{(1.2\lambda)^2}{\alpha^2} \quad (2.8)$$

where λ is the wavelength of the electrons

3. Aberrations (as a first approximation)

$$d_{sph} = 2C_s \alpha^3 \quad (2.9)$$

where C_s is the spherical aberration coefficient and its value is about 1-3 mm in most lenses or well below in case of high resolution microscopy (see 2.3.3).

The value of α is roughly 0.6-0.8°, because electron lenses present distortion at higher angles (see 2.3.3), so a wider value of α would mostly introduce artefacts instead of any improvement. The size of the electron probe is essential for the resolution in STEM, because it influences the area of the specimen which interacts with the beam. This results in a single intensity value from the STEM detector (or spectrum, in case of EELS, see sec. 2.4.2.2) which will be represented as a pixel in the final image: this area is then the smallest available detail of the specimen. Since the source size can not be significantly improved by the illumination system, the diameter of the probe and ultimately the resolution are limited by Abbe diffraction limit, so it is paramount to use the biggest possible collection angle. Unfortunately wider angles introduce aberrations which worsen the resolution.

2.3.3 Electron Optics

Electron Lenses and Aberrations The effect of electron lenses is commonly described by use of the paraxial approximation, which essentially assumes small angles between the optical axis and the trajectories of photons (or electrons). Unfortunately, the requirements of a better resolution are based on bigger angles as stated by Abbe diffraction limit (see eq. 2.8 and par. 2.3.2.2), so the paraxial approximation is no longer a proper description of the optics. Differences and non-ideal behaviours are called aberrations, which can be divided into chromatic and geometric. The first produce deviation of electrons' paths because of their energy differences; the geometric aberration is instead influenced by the convergence angle β and by the azimuthal angle φ , so that focal length changes according to position or incoming angle of the beam. A simple example of geometric distortion is the spherical aberration (see fig. 2.8), where a different convergence angle changes the focal length of the lens. This shows how a wider angle introduces distortion and degrades the image quality, instead of improving the resolution.

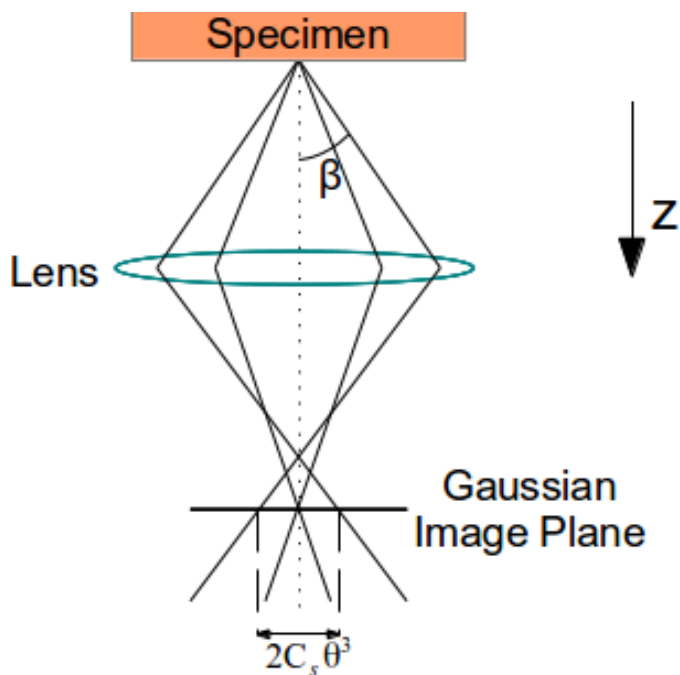


Figure 2.8: Effect of spherical aberration of a lens. At focal length the rays do not converge in a single point because of spherical aberration. z is the direction of the electron beam.

Instead of a crossover point there is a disc formed by the rays. The point where the diameter is smaller is called Gaussian plane and the diameter is

$$d_{sph} = 2C_s \beta^3 \quad (2.10)$$

where C_s is the spherical aberration coefficient and its value is about 1-3 mm in most lenses [69]. For small angles, below 10 mrad, the effect of the aberration can be minimised, but at wide angles the resolution decreases by orders of magnitude: at 200kV, with a 10 mrad semiangle, Abbe limit estimates a probe of approximately 0.13 nm, but spherical aberration with a 1 mm C_s increases the diameter to roughly 2 nm: any improvement from higher voltage would then be neglected. Scherzer proved that aberrations are unavoidable in round magnetic lenses, even though it can be reduced by defocus [79]: In a latter paper [80] he worked on the best condition of resolution, based on aberration and focus distance, defining the Scherzer focus. He also modelled the behaviour of the lenses as power series expansion of wave aberration function χ [79], which represents the phase difference between a perfect wavefront and the actual one, originated by the lens. The problem is that there is a number of relevant aberration and, in theory, an infinite amount of them. This is because aberration can be described by a Taylor expansion of the wave aberration function χ . Its expression as a Taylor expansion is [79]:

$$\begin{aligned}\chi(\theta, \varphi) &= K + \theta[C_{01a} \cos(\varphi) + C_{01b} \sin(\varphi)] + \frac{\theta^2}{2}[C_{10} + C_{12a} \cos(2\varphi) + C_{12b} \sin(2\varphi)] + \dots = \\ &= K + \sum_N \frac{\theta^{N+1}}{N+1} [C_{NSa} \cos(S\varphi) + C_{NSb} \sin(S\varphi)]\end{aligned}\tag{2.11}$$

where θ is the angle with respect to optical axis and φ is the azimuthal one, relative to a plane perpendicular to the column. K and C are numerical coefficients to fit various lenses. This introduces the various kinds of aberration, each described by a C coefficient. Aberration can be divided into two groups: rotationally symmetric (independent from φ) and φ -related astigmatisms. The first ones includes C_{10} , related to defocus contrast, C_{30} , which is the spherical aberration coefficient C_s , C_{50} etc. The second ones introduce 2-fold astigmatism and similar 3-fold, 4-fold, 6-fold ones etc. The φ -related effects are particularly noticeable in multipole lenses (see fig. 2.9), where the focal length depends on the azimuthal angle φ so, for example, electron trajectories on perpendicular planes would be focused differently. If the φ -related astigmatisms are corrected, the widening of the beam can be related to remaining aberration coefficients [78]:

$$d_s^2 = A_n^2 C_{n,0}^2 \alpha^{2n}\tag{2.12}$$

where A_n is a numerical constant that gives the diameter of the disc of least confusion, which is the plane where the minimum beam size is detected (usually different from the Gaussian plane).

Aberration correction requires a new lens design, because aberrations are intrinsic in round lenses [79]. They cannot be corrected as no divergent lenses are possible with

such design. Scherzer then proposed three alternative designs [80], in order to solve the problem

- 1) Field along the optical axis
- 2) Time varying field
- 3) Break of rotational symmetry

The first two solutions proved impractical, so the third one was developed and it led to multipole lenses [81, 82] (see fig.2.9): a complex series of these new lenses and additional coils can act as divergent lenses, helping to reduce the aberrations.

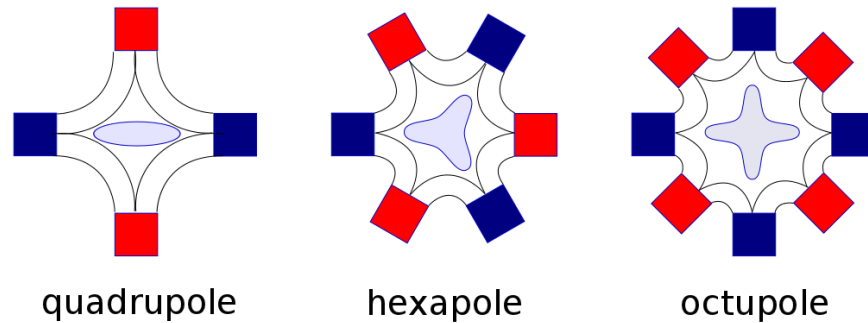


Figure 2.9: Schematics of simplest multipole lenses. Poles are shown in red and blue, to distinguish polarity, the black lines represent the magnetic field and the central shape is the form of the beam in the lens field. Original electron beam section is circular.

This design does not have a cylindrical symmetry but is based on a variable number of poles. Main difference from rotational symmetric lens is that field lines are perpendicular to the optical axis and form a characteristic pattern[78] (see fig.2.9). Analytically, this can be described by magnetic scalar potential Φ , which satisfies Laplace's equation:

$$\Phi(r, \theta) = r^N [p_N \cos(N\theta) + q_N \sin(N\theta)] \quad (2.13)$$

where $2N$ is the number of poles in the lens ($N=2$ refers to a quadrupole lens, $N=3$ to a hexapole one, etc.), r and θ are polar coordinates. The magnetic field in the lens is equal to the gradient of Φ .

The purpose of a quadrupole lens on a beam is to form an elliptical beam on a plane perpendicular to the optical axis: the resulting beam is smaller in one direction

and wider in the perpendicular one. Similarly, hexapoles form a three-spiked shape (three-fold symmetry), while octupoles creates a cross outline (see fig.2.9). Generally speaking, the beam is elongated in N directions (positive spherical aberration) and shrunk in between those N spikes (negative spherical aberration). However, this beam deformation can be compensated by a second lens of the same kind, creating an inverse field further down in the microscope.

On the other hand, radial deformation are more interesting as we can now compensate third order aberrations (which vary as r^3 , such as C_s) thanks to similar behaviour of lenses as a function of r . Moreover, a long lens (with respect to optical axis) has even stronger dependence on r , because of a second order effect[78]: the deformation of the beam in the first part of the lens pulls the beam away from the optical axis, increasing the strength of the lens as the electrons move along. The result is that of a “long” octupole lens deflection is again a function of r^3 . The working principle of the aberration correction is however based on a combination of many lenses, both multipole and conventional, because many stages are necessary to compensate aberration in the x and y plane.

Using suitable combination of these multipole lenses, two main designs of aberration correctors for microscopes were created by the Nion [83] and CEOS [84] companies. CEOS design uses two hexapoles beside additional conventional lenses (see fig. 2.10). The second order effect of hexapoles was detailed by Hawkes [85] and it lead to suitable designs [86, 87] and application [88]. The poles polarity is opposite in the two hexapoles, so first order effect is the opposite in the two lenses and its influence is negligible, while the second order becomes relevant. It requires some alignment from conventional round lenses, called transfer lenses (TL1 and TL2) for optimal precision [78].

However in this thesis the aberration corrected data (see section 4) were acquired on a Nion microscope in STEM mode. Its design is based on four quadrupoles and three octupoles, originally proposed by Scherzer [89]. First, the electron beam crosses condenser lenses C1 and C2: the former produces a crossover of the electron gun emission, reducing its size; the latter lens selects the focus distance for the following stages. Then the corrector is composed of four quadrupoles (Q1-Q2-Q3-Q4) and three octupoles (O1-O2-O3) (see fig. 2.10): the quadrupoles mostly act as a conventional, radially symmetrical lens and control the rotation of the beam, for it to align with the octupoles. O1 and O3 compensate third order spherical aberrations respectively for x and y plane. This causes 4-fold aberration, which can be corrected by O2. Finally scan coils align the beam to the optical axis, so off-axis aberration can be neglected. The result is a negatively aberrated beam, which is pre-compensated for non-ideal objective lens (OL), producing an aberration corrected beam to probe the specimen [81].

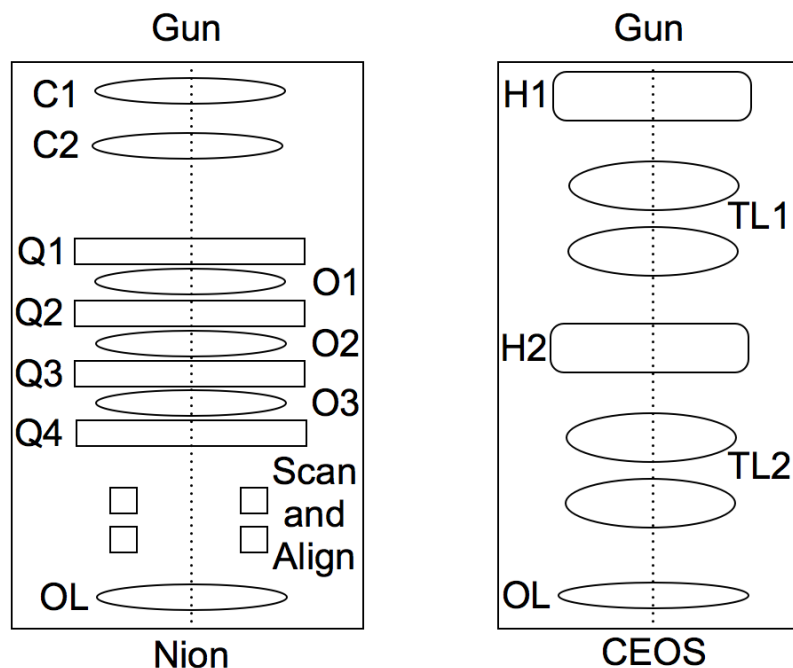


Figure 2.10: Nion and CEOS schematics of Aberration corrected systems for STEM microscopy. Q stands for quadrupole lens, O for octupole, OL for Objective Lens, H for hexapole, TL for transfer lens. Both systems have a second set of lenses (Q3-O3-Q4 and TL2) to compensate distortions from the first ones, while they also shape the beam.

These configurations correct aberrations up to 20-30 mrad, so a wider collection angle can be used. This has benefits on resolving potential of the microscope (as explained in section 2.3.2) and results in atomic resolution, sub-Å probes for STEM and C_s well below 1mm. For example, Abbe criterion predicts a probe size of 0.63 Å for 200kV STEM system with 20 mrad collection angle.

One convenient method for the diagnosis of aberrations in the STEM is the use of the Ronchigram method. This involves visualising the diffraction pattern of an amorphous sample (see fig.2.11). The basic assumption of this technique is that aberration corrected beam is supposed to be a plane wave, which corresponds to an emission of a distant source (far-field). The best setting to image an infinite distant object is focusing its emission in the focal point and acquire an image in that position, which corresponds to infinite magnification. The result is the visualisation of the phase of the beam: ideally, if all aberrations were cancelled, it would be entirely homogeneous, but in real cases only the central area is flat. For an uncorrected microscope, there will be a relatively small flat area with a radius probably less than 10 mrad and then a circular ring around this, as phase fluctuations with an angle start to appear. For an aberration corrected system as described above, the aberration-free area is much larger, in the order of 30 mrad. Outside this, the shape of the distorted area is no longer round, and will take on some of the symmetry of the correcting elements, for example a six pointed star in a hexapole corrected system and a square shape in a

quadrupole-octupole system.

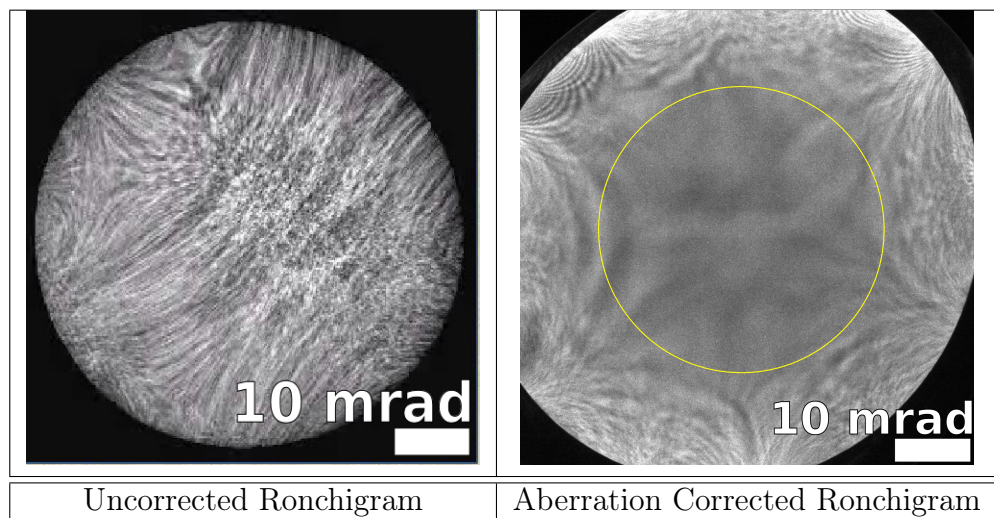


Figure 2.11: An example of two Ronchigrams with and without aberration correction. A central undistorted area, where aberrations are corrected, can be noticed in both images. Its size increases with aberration correction and results in better image quality. Outer zones, corresponding to higher angles, are clearly deformed because higher order aberrations come into play, as illumination angle increases. The yellow circle in the aberration corrected Ronchigram corresponds to 38.65 mrad. Courtesy of Dr. Sam McFadzean.

Aperture Apertures are used to limit the electrons moving towards the following stage of the microscope optics (see 2.12) by reducing the collection angle.

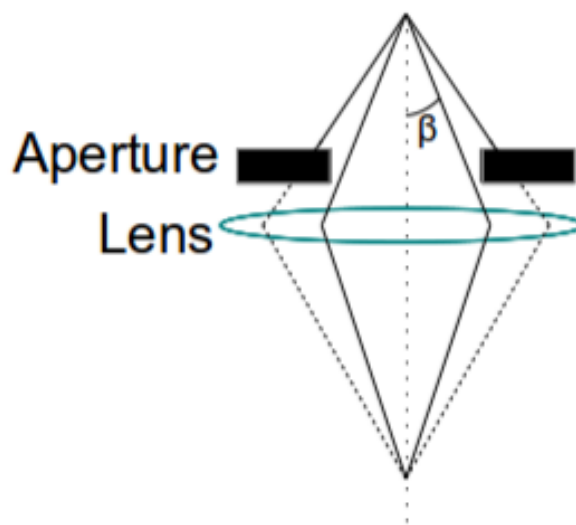


Figure 2.12: Schematic of an aperture. β is the collection angle. The electrons presenting a collection angle larger than β are blocked by the aperture: this is one of the mechanisms to control the electron beam and the relative angle. Apertures can also be used to reduce aberrations related to high angles, by limiting the collection angle β .

This is meant to cancel the contribution from the aberrated part of the Ronchigram, which always presents some aberration at larger angles (see fig. 2.11). The electron beam below the aperture is free of aberration.

The collection angle is then ultimately determined by the aperture, eventually defining the size of the probe and the resolution, as predicted by Abbe diffraction limit.

2.4 Electron Scattering and Studying Materials in TEM and STEM

Many techniques and configurations were developed to obtain the structural, chemical and magnetic characterisation of specimens. In order to understand all these methods, it is useful to look at the effects of an electron beam on a specimen: all interactions are due to Coulomb force, even though it results in many different effects (see fig.2.13) on both the outgoing electrons and the specimen itself.

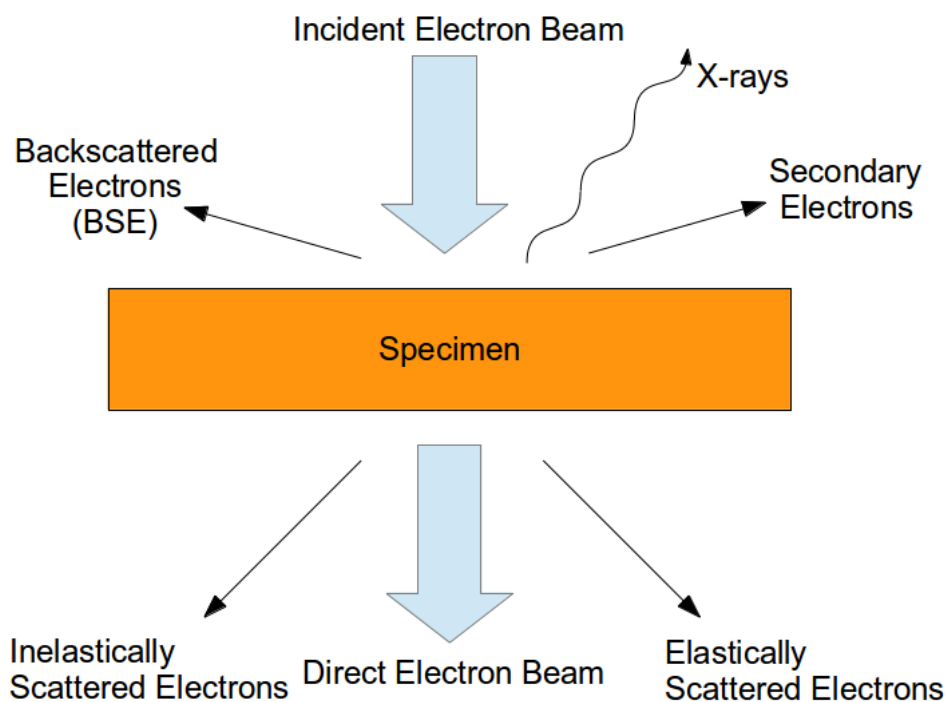


Figure 2.13: Some of the signals generated by interaction of an electron beam with a specimen in a TEM.

These signals can be related to many effects and properties of the specimen: here brief descriptions of the main techniques, especially those relevant for this work, are presented .

Signal	Technique	Provided Information
Elastically Scattered Electrons	BFTEM	Imaging, Morphology
Elastically Scattered Electrons	Diffraction Pattern	Crystallography
Elastically Scattered Electrons	HAADF	High Resolution Imaging, Stoichiometry
Inelastically Scattered Electrons	EELS	Stoichiometry, Chemical Bonding
X-Rays	EDX	Stoichiometry, Chemical Bonding

Table 2.3: List of some of the available signals in a TEM, relative techniques for analysis, and provided information.

The electrons coming out of the specimen can be influenced by different mechanisms, both wave and particle theories are necessary to explain all the results: for example, quantum physics is widely used in the EELS analysis, while diffraction patterns are explained by wave optics. A general (and rough) distinction is elastic and inelastic scattering, based on the energy of outgoing electrons: those with an energy close to the incident beam were elastically scattered; the electrons which lost 10-20 eV or more are considered to be inelastically scattered.

Elastic scattering is associated to interaction between the electron beam and nuclei in the specimen, so it can provide information about the atomic number and the disposition of the atoms: this mechanism is therefore relevant for stoichiometry and crystallography analyses. On the other hand, inelastic scattering is related to electrostatic interaction between the electron beam and the outer shells of the specimen, so it is possible to probe orbitals and chemical bonds: the resulting effect on electrons can be interpreted in terms of chemical information, such as stoichiometry.

2.4.1 Elastic Scattering and imaging

In electron microscopy, elastic scattering refers to the Coulombic interaction of incoming electrons with a specimen, with limited energy losses (mostly in the order of tens of meV). It is an interaction with the whole atom mediated by its electrostatic potential and transfer of momentum to the nucleus. It is different from interaction with weakly bound electrons, which is discussed in the following section (see 2.4.2.1).

It is necessary to consider electrons as waves in order to introduce the concept of phase coherence, which is fundamental to understand coherent scattering. The electron beam can be approximated as a plane wave with constant phase. Most of interactions

with the specimen are small enough to preserve the phase coherence. This happens because electrons have a low probability of passing close to nuclei, then strong interaction and energy exchange are unlikely. The final scattering angle is normally within few degrees and the wavelength is almost unaffected, so coherence is retained. However, few electrons happen to move close to nuclei, which cause huge deflection because of the big mass difference between the two. The wavelength is therefore changed substantially and coherence is lost. It is also possible to excite a phonon in the lattice.

In case of a crystalline specimen, the global behaviour of the lattice can be explained by the Huygens approach: the incoming electron beam is approximated as a plane wave and atoms act as centre of scattering. Spherical waves are formed there and their propagation causes interference phenomena because of different path length. At specific angle constructive interference causes these waves to be in phase (see fig. 2.14), as predicted by Bragg's law $n\lambda = d\sin\theta$.

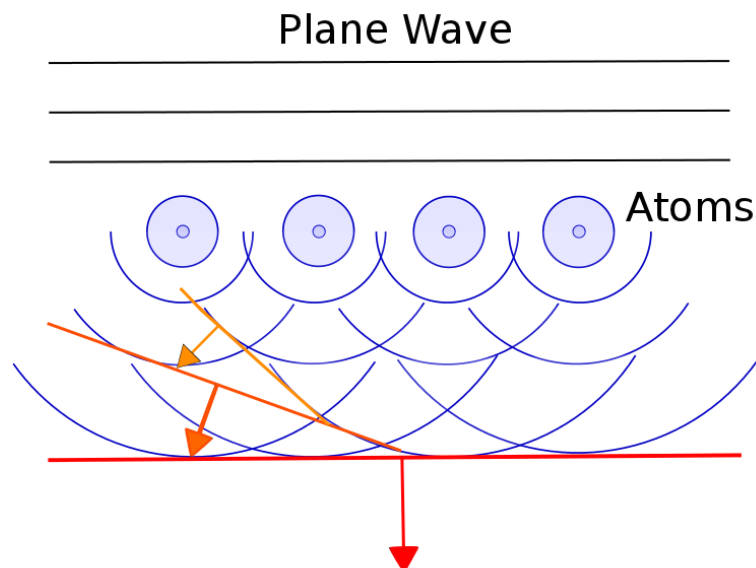


Figure 2.14: Huygens description of propagation of waves. The electron beam is approximated as a plane wave, while atoms act as centre of scattering and produce spherical waves (back propagation is not shown for simplicity). Wavefronts are represented in different colour according to direction and order of diffraction.

Waves cause constructive and destructive interferences creating a characteristic pattern of high intensity spots, which reflect the periodicity of the crystal or typical distances of atoms in the specimen, in case of material with only short-range order (amorphous or glassy materials). This coherent interference gives rise to electron diffraction patterns (DP), which are very useful in analysis of crystalline and amorphous materials. It is also critical to the imaging crystalline specimens, using either diffraction or phase contrast methods. See 2.4.1.1 for more details.

In order to move to a mathematical description of this process a plane wave Ψ was described as

$$\Psi = \Psi_0 e^{2\pi i k r} \quad (2.14)$$

where Ψ_0 is the amplitude, k is the wavevector and r the distance of propagation [69]. The scattering even produce a second wave Ψ_{sc} , which is spherical.

$$\Psi_{sc} = \Psi_0 f(\theta) \frac{e^{2\pi i k r}}{r} \quad (2.15)$$

the term $f(\theta)$ is called atomic-scattering amplitude and accounts for the reduction in amplitude of Ψ_{sc} when compared to Ψ_0 : it depends on θ , which is the semi-angle between the direction of the wave propagation and optical axis[69]. $f(\theta)$ was reported to be equal to

$$|f(\theta)|^2 = \frac{d\sigma(\theta)}{d\Omega} \quad (2.16)$$

Where σ is the cross section, a basic parameter to measure the probability of (any) scattering of an atom. Ω is the solid angle across which electrons are scattered [69].

A simple formula of σ in a specimen is

$$\sigma_{specimen} = \frac{N_0 \sigma_{atom} \rho}{A} \quad (2.17)$$

where N_0 is Avogadro's number, ρ is the density and A is the atomic weight [69].

However, it is more common to think of differential cross section, with respect to solid angle Ω : this happens because different signals can be detected according to the angles of collection and an integral can quantify the expected intensity.

$$\frac{d\sigma}{d\Omega} = \frac{4\gamma^2}{a_0^2} \left(\frac{Z}{q^2 + r_0^{-2}} \right)^2 \approx \frac{4\gamma^2 Z^2}{a_0^2 k_0^4} \frac{1}{(\theta^2 + \theta_0^2)^2} \quad (2.18)$$

where $a_0 = 4\pi\epsilon_0\hbar^2/m_0e^2$ is the first Bohr radius, equal to 0.0529 nm; Z is the atomic number; k_0 is the wavevector of the incident electron and $\hbar q$ is the momentum transfer to the specimen; $\gamma = (1 - v^2/c^2)^{-1/2}$ which is called relativistic factor; $\theta_0 = (k_0 r_0)^{-1}$; $r_0 = a_0 Z^{-1/3}$ [91, 92].

The differential cross section is essential for quantitative analysis and simulations, because it provides the probability of interaction of a given atom: this allows to calculate the electron signal relative to the presence of a given amount of elements. Alternatively, an electron flux in a certain range of scattering angles can be related to specific atoms.

2.4.1.1 Diffraction Contrast TEM Imaging

The differential cross section describes the scattering angles for electrons which interact with a single nuclei. In a crystalline specimen, this effect is repeated across the lattice and the global behaviour is similar to Huygens description in fig. 2.14 which obeys Bragg's law. This means that electrons are elastically scattered in regular distribution (called diffraction patterns) and their direction is described by Bragg's angles. As a consequence, a detector can record periodic peaks of intensity from crystalline materials, if the imaging system is in the diffraction mode (see fig. 2.6). The bright-field imaging condition can instead present the morphology of the specimen, which corresponds to the inverse Fourier transform of the diffraction pattern. A change of periodicity in the specimen, such as in case of a polycrystalline materials or dislocations, causes the diffraction patterns to be different in the various areas of the sample. The morphology then present a contrast, caused by the two different intensity distributions in the crystalline structures [69].

The process is however more complicated because of dynamical scattering, a form of multiple scattering where a diffracted beam undergoes a second scattering event causing it to return to its original orientation. This is a closely related to specimen thickness, as it implies a higher number of scattering sites. The final result is a complex relation between intensities of diffracted beams, so related contrast loses sharpness. Moreover, beam spreading has to taken into account: the convergence angle, which is either set by the objective aperture in BFTEM, which corresponds to the collection angle after the specimen. However, additional spreading is added by inelastic scattering, consisting of incoherent low energy excitations (like plasmons, see section 2.4.2.2 for details and 2.4.2.1 for general overview of inelastic scattering).

2.4.1.2 Mass-Thickness Contrast

Amorphous materials, on the other hand, present little diffraction contrast and dynamical scattering. The contrast is therefore interpreted in terms of specimen cross section, σ (see eq. 2.17), and average atomic number, as the differential cross section is a function of the atomic number Z (see eq. 2.18). This means that various elements scatter the electrons at different angles: more specifically, atoms with higher atomic number deflects more. A similar behaviour can be detected in case of different density or thickness of the specimen: so this effect is called mass-thickness contrast. It is explained as incoherent elastic scattering (from coherent beam illumination): the elec-

trons are scattered at higher angles by heavy atoms and thick zones of the specimen, so that they are stopped by the aperture or they miss the detector. The signal is mostly forward peaked and is concentrated within roughly 5° from the beam direction [69] so the corresponding detector is placed along the optical axis (see fig. 2.7). The related method is called bright field (BF).

2.4.1.3 HAADF STEM imaging

The STEM analyses in this work are based on the Annular Dark Field (ADF) detector [75] because of its high spatial resolution. It is shaped like a ring, collecting electrons in the range from tens to hundreds of mrad from the optical axis (see fig. 2.7). It relies on incoherent elastic scattering, because the detector cannot isolate coherent signals. This is due to two mechanisms: signals averaging and thermal diffuse scattering (TDS). The first is a consequence of the shape of the detector, which acquires electrons in a wide range of angles all around the optical axis, averaging the intensity. Most coherent signals, such as DP, are scattered by 10-20 mrad, so they do not normally fall in the angle range of ADF; when they do, their contribution is negligible if compared to incoherent signals [78]. Thermal diffuse scattering refers to atoms vibrations which reduces the intensity from coherent Bragg scattering, especially at high angles: it is an inherently inelastic and incoherent mechanism [93] and its integrated intensity in a HAADF detector is higher than that of coherent scattering. The literature is still uncertain as to which is the main cause of incoherent scattering [78].

The most important STEM detector is the High Angle ADF (HAADF) sensor (see fig. 2.7), which allows direct interpretation of atomic resolution imaging [94].

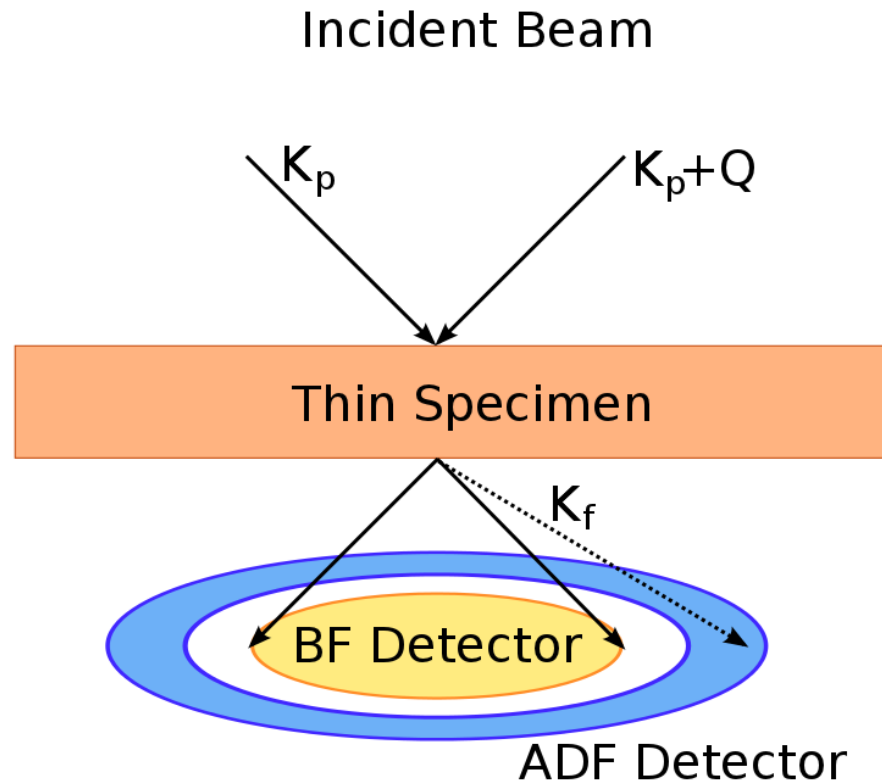


Figure 2.15: Schematics of Bright Field (BF) and Annular Dark Field (ADF) detector in STEM. K_p is the transverse wavevector of the illumination, K_f is the corresponding value for electrons scattered towards the detector and Q is the desired spatial frequency for the final image (see the description of eq. 2.21 for details). The range of values for these wavevectors is limited by apertures and convergence illumination. Angles are exaggerated.

The HAADF detector collects electrons which experienced incoherent elastic scattering, in the range between few tens to few hundreds mrad from the optical axis.

The description of elastic scattering in this angle distribution is based on differential cross section, which is proportional to Z^2 (see eq. 2.18). This simplifies the interpretation of atomic resolution images, as high atomic number elements correspond to higher intensity. However, the formula is based on Rutherford model, which is based on isolated atoms, while electron elastic interaction in crystals presents few differences because of Coulomb potential screening [78]. Moreover, the electron propagation tends to be directed along atom columns, because the associated periodic potential acts as a waveguide, so electrons interact strongly with localised states, mostly with 1s [95]. This behaviour is called channeling effects and it alters the intensity of HAADF signal too, which has a slightly lower dependence on Z in the experiments: it is proportional to Z^ζ where ζ is between 1.5 and 2, normally about 1.7 [78]. Nonetheless, the intensity can be related to Z , so the brightest atoms are considered the one with highest atomic

number, which helps comprehension of atomic resolution images: this effect is referred to as Z-contrast. However, In order to understand the contrast in HAADF, in both experiment and simulations, the channelling effect and the interaction with the specimen and its structure has to be considered. The electron channelling in the crystal can be modelled and included in the mathematical representation of wave propagation in HAADF imaging. This description also provide details about the HAADF detector and imaging process. First, the electron wave Ψ_f after interaction with the specimen is described: it represent the signal collected by the detector and it includes the factors which influenced it, such as the crystal lattice.

$$\Psi_f(K_f, R_p) = \sum_g \phi_g A(K_f - g) \exp[-i(K_f - g) \cdot R_p] \quad (2.19)$$

where ϕ_g comes from the transfer function of the specimen: in reciprocal space a crystalline sample would contribute with its Fourier transform (as a first approximation), which corresponds to a series of Bragg diffracted spots with amplitude ϕ_g . g is the reciprocal lattice vector corresponding to each spot. $A(K_f)$ is the aperture in reciprocal space, where K_f is the transverse wavevector of the electrons scattered towards the detector. R_p is the position of the electron probe on the specimen [78].

The relevance of ϕ_g reflects the role of crystal structure and channeling in HAADF image formation. This is also confirmed by Bloch wave simulations showing that intensity collected by ADF originates mostly from channelling effect [95].

The intensity from position R_p of the specimen, as detected by the ADF detector, is described by the probability density of the electron wave, convoluted by the object function $O(R_p)$.

$$I_{ADF}(R_p) = |\Psi_f(K_f, R_p)|^2 = |\psi_p(R_p)|^2 \otimes O(R_p) \quad (2.20)$$

where $\psi_p(R_p)$ is the probe wavefunction and $O(R_p)$ is the object function, which is the amount of scattering coming from an atom [78].

I_{ADF} can be rewritten in term of Q , which is the desired spatial frequency for the final image, to eventually isolate the contribution from the specimen, $O(R_p)$

$$I_{ADF}(Q) = \int D_{ADF}(K_f) \sum_g \phi_g \phi_{g-Q}^* A(K_f - g) A^*(K_f - g + Q) dK_f \quad (2.21)$$

where D_{ADF} is the detector function, which equals 1 for acquired values of K_f , 0 elsewhere [78].

This formula is based on the two beam model, where two electrons with wavevectors K_p and $K_p + Q$ respectively, are scattered by the specimen respectively by g and $g - Q$: if the resulting wavevector is the same, the two electrons can create interference and produce contrast. If this common wavevector is K_f , the two beams and the relative contrast are collected by the ADF detector [78].

Thermal diffuse scattering is neglected in this situation, as well as precise phase variations. The weak phase approximation, which assumes the electrons phase variations due to interaction with the specimen to be little, is assumed in previous equations.

2.4.2 Inelastic Scattering and Spectroscopy

When a highly energetic electron beam hits a specimen, many processes happen, as shown in fig. 2.13. Outcoming signals are due to scattered electrons or photons, but most of those signals have an energy that is considerably lower than that of the incoming beam. This is true for most of electrons which are scattered below the specimen, for secondary electrons, as well as most photons, either in form of X-rays or cathodoluminescence. The many mechanisms that account for these losses of energy are all considered to be inelastic scattering, but physical processes are considerably different. The details of these interactions are presented in the section 2.4.2.1 to introduce the physics behind EELS spectroscopy, which analyses the energy loss from inelastic scattering to characterise materials: this technique is described in sec. 2.4.2.2.

2.4.2.1 Theory of Inelastic Scattering

The most common effect is plasmon excitation: it is caused by an interaction between the beam and the weakly bound orbitals (also called “free electron gas”) which results in a collective motions of electrons and a perturbation (“ripple”) of the electrostatic field of the specimen (more details in 2.4.2.2). Plasmons can be described with good degree of approximation by Drude model, where collective motion of free particles, reacting to an electrostatic field, is damped.

$$m\ddot{x} + m\Gamma\dot{x} = -eE \quad (2.22)$$

m is the mass of free electron, x is the displacement, Γ a damping term and E is the oscillatory electrostatic field [70]. This process is stronger in metals, because of higher number of free electrons, but it can be detected in every material in principle. Plasmons’ cross section can be even higher than that of elastic scattering (for small scattering angle), making it the most probable inelastic scattering event: its value is in the range of $10^{-22}m^2$ at 200kV [69]. Their energy loss is proportional to plasmon frequency, which in turn may reflect a number of properties, such as high energy bands [96] (related to oscillating free electrons) size and shape of particles [97] or relative

composition of elements in alloys [98]. Typically the energy losses are between 15 and 25 eV and the scattering angle rarely exceeds 10mrad. These are consequences of the excitation conditions, characterised by large impact parameter, which represents the distance between the incoming and excited electrons. If those are relatively further away, collective response allow energy exchange but small momentum transfer, then little angle deviation [70]. A small impact parameter (i.e. close interaction) is a more improbable condition, which causes sufficient energy transfer to overcome the ionisation threshold and to move the excited electron to higher energy state [70]. The cross section for this process is in the range of $10^{-23}m^2$ at 200kV [69], roughly an order of magnitude less than plasmon's one. This is reasonable since a close interaction is less likely to happen than a distant one, because of size and density of electrons.

Excitation of electrons can start other energy loss processes, such as X-ray and secondary electrons emission. The process of X-rays starts after ionisation, in case the excited electron from the core K shells leaves the atoms. It then leaves a hole in its previous state, which is then occupied by another electron from higher energy states. This transition creates an X-ray, whose energy is equal to the difference between the two states. The value of cross section varies greatly as a function of atomic number and which energy states are involved. As a consequence, X-ray emission is more probable from high atomic number atoms. Moreover, the energy of the ray (in the order of keV) is characteristic to the material, so it allows identification of the emitting atom.

The energy spectrum of X-rays shows sharp intensity peaks, which corresponds to electron transitions, beside a wider background: this is called bremsstrahlung and means "braking radiation". It is caused by interaction with nuclei, instead of core electrons. The momentum transfer is considerable, given the mass difference between nuclei and electrons, and it leads to synchrotron radiation in form of X-ray emission. The energy range is wide so it overlaps both X-ray emission from electron transition and EELS spectroscopy signals (see sec. 2.4.2.2).

Another effect of the electron beam is the emission of secondary electrons (SE) from the specimen. These are from higher energy states, such as valence or conducting band, so a small energy transfer from the electron beam is enough to reach the vacuum level and to leave the specimen. As in case of plasmon, the energy transfer is limited and the SE energy is rarely above 50 eV. The cross section is complex, but it is considered to be below $10^{-25}m^2$ at 200kV [69]. They are emitted close to the surface of the specimen, because their low energy does not allow movement through the material for a long distance.

Auger electrons are considered secondary electrons as well, but they are emitted in a condition similar to characteristic X-rays. In fact, they require the ionisation of an electron from core state and subsequent transition from a higher energy shell to replace it. The Auger electrons absorb the energy released from this transition to reach the vacuum level, preventing X-ray emission. Auger electrons (just as SE) are normally emitted from surface of the specimen or nearby, because of their low energies: they

are normally between few hundreds and few thousands eV [69]. However, emission of these electrons is not efficient, as it requires multi-body interaction, namely the ionised electron, the transition and the Auger one.

In materials with a direct energy gap, such as proper dielectrics and semiconductors, ionisation of valence electrons can also create hole-electron pairs which can emit a photon. Its energy is equal to the energy gap and it can be detected to study the band structure: this process is called cathodoluminescence (CL).

Lattice vibrations (phonons) can be another source of inelastic scattering, which has various origins. An electron from the beam can interact with an atom transfer enough momentum to cause a vibration, Auger electrons and X-rays are sometimes converted to phonons as well. They have little energy (less than 0.1 eV [69]) but the momentum transfer causes a deflection of about 5-15 mrad in the electron from the beam [69]. Phonons ultimately increase the temperature of the specimen, particularly those with low thermal conductivity, such as polymers: heating up to hundreds K above the original temperature is possible with the proper electron gun, such as a thermoionic source [69].

Beam damage to the specimen is an issue and it can present itself in many forms, potentially altering the basic properties of the specimen. Beside heating, radiolysis can be a problem, particularly for polymers. High energy electron illumination can change the bonds and break the polymer chains, eventually leading to mass loss [69]. Alternatively, side group bonds can be broken, leaving radicals and promoting crosslinking [69].

The electron beam may also knock out atoms from the lattice and create vacancy or interstitial clusters, which can condense into dislocation loops. Electron microscopes have even been used to simulate damage from nuclear reactors. This happens when a considerable amount of energy is exchanged between the electron probe and the specimen: in the present work losses as big as thousands of eV are considered (e.g. EELS spectra in 2.4.2.2), whereas higher values have negligible intensities and are not normally detected by the instruments.

All these mechanisms obey energy and momentum conservation, thus the electron energy states and ultimately the band theory have to be considered in order to understand energy absorption of core electrons and changes of state: a quantitative description of energy and momentum differences is explained later on in this section, in 2.4.2.2, where orbitals calculations and states transitions are evaluated. However, it is easier to start from cross section, to define the probability of interaction: differential cross section in particular is an important parameter to determine intensities and settings, typically angles and energy range: a good starting point for a mathematical description is Bethe theory [99], where conservation of energy and momentum constraints possible transitions between states and, consequently, energy losses.

$$\frac{d\sigma_n}{d\Omega} = \left(\frac{m_0}{2\pi\hbar} \right)^2 \frac{k_1}{k_0} \left| \int V(r) \Psi_0 \Psi_n^* \exp(iq \cdot r) d\tau \right|^2 \quad (2.23)$$

$$V(r) = \frac{Ze^2}{4\pi\epsilon_0 r} - \frac{1}{4\pi\epsilon_0} \sum_{j=1}^Z \frac{e^2}{|r - r_j|} \quad (2.24)$$

k_0 is the wavevector of electron before interaction, k_1 is the one after it. Ψ_0 and Ψ_n are atomic wavefunction responsible for the energy loss, in the first Born approximation.

In order to include energy dependence, a double differential cross section is required. The previous formula of a differential cross section (see eq. 2.18) does not consider band theory, so a new estimate was introduced: a non-relativistic approximation gives

$$\frac{d^2\sigma}{d\Omega dE} \approx \frac{4\gamma^2 R}{Ek_0^2} \left(\frac{1}{\theta^2 + \theta_E^2} \right) \frac{df_n(q)}{dE} \quad (2.25)$$

where $f_n(q)$ is the generalised oscillator strength (GOS)[99]

$$f_n(q) = \frac{E_n |\varepsilon_n(q)|^2}{R (qa_0)^2} \quad (2.26)$$

where R is the Rydberg energy, E_n is the energy loss and $|\varepsilon_n(q)|^2$ is the inelastic form factor (also dynamical structure factor), composed by ε_n , the transition matrix element between two atomic states ψ_0 and ψ_n [70].

$$\varepsilon_n = \int \psi_n^* \sum_j \exp(iq \cdot r_j) \psi_0 d\tau = \left\langle \psi_n \left| \sum_j \exp(iq \cdot r_j) \right| \psi_0 \right\rangle \quad (2.27)$$

The final parameter for differential cross section is the characteristic angle θ_E , which arises from a Lorentzian distribution of intensity and is described by the following formula. θ_E is the half width at half maximum (HWHM), however there are typically long tails in this distribution[70].

$$\theta_E = \frac{E}{\gamma m_0 v^2} = \frac{E}{(E_0 + m_0 c^2)(v^2/c^2)} \quad (2.28)$$

The basic result of these formulas is a forward peaked signal at low energy loss, while a higher energy component is centred around a typical angle $\theta_r \approx \sqrt{E/E_0} \approx$

$\sqrt{2\theta_E}$, called the Bethe ridge, in the case of small angles and in a non-relativistic approximation [100]. The energy loss corresponding to ionisation thresholds can be calculated by consideration of transitions between atomic levels, but the interpretation and quantification of EELS spectra and HAADF data require an accurate description of atomic orbitals and potential. Hydrogenic model of atoms is a good starting point to describe core states, since an isolated atoms has orbitals which are similar to those found in bulk materials (such as a specimen). The probabilities of transitions between these states are reflected by the the differential cross section.

Core orbitals can be calculated from Schrödinger equation with a potential given by a parametrised effective charge $Z_s e$, localised in the nucleus, which accounts for screening from outer shells [101]: the detected ionisation energy E_k would then be

$$E_k = Z_s^2 R - E_S \quad (2.29)$$

where R is the Rydberg energy and E_S represents the reduction of inner-shell binding energy due to outer orbitals. Hence the net energy E_t , that is the sum of the kinetic and electrostatic components, can be written as

$$E_t = E - E_k = E - Z_s^2 R \quad (2.30)$$

where E is the energy loss measured in EELS spectra[101].

Therefore, the Schrödinger equation for the net energy is

$$(-\hbar^2/2m_0)\nabla^2\psi - (Z_s e^2/4\pi\epsilon_0 r)\psi = (E - Z_s^2 R)\psi \quad (2.31)$$

The Hartree-Slater central-field model [102] provides a simplified solution for this equation, based on a spherical field around the nuclei, so the orbitals could be calculated more easily.

$$\left[\frac{\hbar^2}{2m_0} \frac{d^2}{dr^2} - V(r) - \frac{l'(l'+1)\hbar^2}{2m_0 r^2} + E_t \right] \phi_n(r) = 0 \quad (2.32)$$

where E_t is the sum of kinetic and electrostatic energy, ϕ_n is a solution of radial Schrödinger equation and l' is the angular momentum quantum number. The electrostatic potential of the atom $V(r)$ is approximated [102] as

$$V(r) = -6 \left[\frac{3}{8\pi} \rho(r) \right]^{-1/3} \quad (2.33)$$

where $\rho(r)$ is the charge density in the atom. This is a correction which accounts for the distribution of charges, which is not considered in the assumption of a spherical field.

However, an additional correction to the electrostatic potential is required, since a core electron is promoted to a different state in the process and this corresponds to a lower charge in core shells: it is called core hole effect. If the core charge is set to $Z + 1$ there is an improvement in the accuracy of calculations, but multi-particle simulations are required to properly account for the results because the electronic orbitals adjust to the different charge and change their energies. One of the reasons is core excitons, which is a couple of hole and electron, bound by Coulomb interaction. Excitons create new energy levels and may cause shifts and sharpen peaks [103, 104], changing the shape on the spectrum.

Once orbital wavefunctions are well know, a transition matrix element can be considered. In case of a transition between two states ε_n can be approximated as

$$\varepsilon_n(q) = \int \psi_n^* \exp(iq \cdot r) \psi_0 d\tau \approx \int \psi_n^*(iq \cdot r) \psi_0 d\tau \quad (2.34)$$

thanks to the Taylor expansion of $\exp(iq \cdot r) \approx 1 + (iq \cdot r) + \dots$ and to the orthogonality of ψ_0 and ψ_n , which cancels the integral with the first term of the expansion (which is 1). The remaining term contains the odd function $q \cdot r$, which causes the result to be zero unless ψ_0 and ψ_n have a different symmetry: for example a transition between s-state (even symmetry) and a p-state (odd symmetry) is allowed. This is called the dipole selection rule [70].

In order to consider the probability of these electron transitions, Fermi golden rule [105] has to be considered

$$T_{i \rightarrow f} = \frac{2\pi}{\hbar} |\langle f | H' | i \rangle|^2 N_f(E) \quad (2.35)$$

where $T_{i \rightarrow f}$ is the probability of transition from state i to f per unity of time. H' is a first order perturbation of the Hamiltonian, calculated from Hartree-Slater central-field method and $N_f(E)$ is the density of final states. The differential cross section $d\sigma/dE$ is proportional to this transition probability and directly linked to the final density of state $N_f(E)$. This is especially important because it allows to investigate occupation of final states, which are outer shell at high energy, responsible for chemical bonds. When an element has many possibly oxidation states, the difference between those is due to the number of valence electrons shared with different atoms, which is exactly reflected by $N_f(E)$. EELS spectrum can then identify elements, by their characteristic ionisation threshold, and their oxidation state, so chemistry of the specimen can studied.

Based on these formulas, the ionisation thresholds in the spectrum (see fig.2.17) can be identified and explained, since core states are basically identical in single atoms (like in previous formulas) or in a complex specimen. Most common features correspond to K, L and M edges (see tab. 2.4), which are caused by different atomic shells and retain a characteristic shape, such as delayed maxima for M_{45} peaks [106].

Edge	Ionisation Orbital
K	1s
L_1	2s
$L_{2,3}$	2p
M_1	3s
$M_{2,3}$	3p
$M_{4,5}$	3d

Table 2.4: List of some of the detectable edges in EELS spectroscopy, beside the related ionisation orbital. Electron is promoted from that state to the first available empty one, which generally depends on the sample (e.g. the $M_{4,5}$ edge of *Ba* corresponds to a 3d→4f transition).

The shapes of ionisation thresholds depends on the involved element and specifically on the electronic band configuration. Most K shapes are sawtooth-like, which directly correspond to the activation of electron transition from 1s orbital. On the other hand, L_{23} features are more rounded and present a shifted peak for third row elements (from Na to Cl). This is caused by angular momentum factor $l'(l'+1)$ in the Schrödinger equation, called centrifugal potential. In the range of energies beyond the ionisation threshold, this decreases the overlap between the 2p orbital (initial state of L_{23} transitions) and the final states [70]. It results in a delayed maximum, at 10-20 eV above the fundamental transition energy. A different L_{23} edge shape is found for fourth period elements, like Ti, where the dipole selection strongly enhances the transition from 2p to 3d orbitals, causing sharp transitions with high intensities (so called “white lines”). In this case, it is easier to notice the difference between L_2 and L_3 , which is caused by spin-orbit coupling [70].

Similar behaviour is found in M_{45} edges: fifth period elements show a delayed maximum 50-100 eV above ionisation threshold, because of the centrifugal potential hinders with the 3d-4f electron transition. Sixth row elements between Cs and Yb, present white lines because f orbitals offer many empty final states for electron transitions [70], as an example of the role of the final density of state $N_f(E)$.

These edges provide more information than the ionisation threshold energy, the surrounding crystallographic and chemical conditions can be investigated by a wider analysis of the shapes. First, a variation of the ionisation energy can be attributed to chemical shift, which reflects the effect of bonded atoms on the core state. Even though the related wavefunction does not change significantly, its energy can increase

or decrease by up to 20 eV [70, 107, 108]. In metals, this is normally caused by bonding, since it affects valence electron orbitals and their screening of the electrostatic potential of the nucleus. In semiconductors and dielectrics, the energy gap influences the possible transitions, so changes of the gap cause different transitions and chemical shift. For example, this happens when moving from conductive graphite to insulating diamond, where the introduction of an energy band from diamond shift the ionisation threshold [70].

Moreover, the tails at higher energy show interesting features called Energy Loss Near-Edge Structure (ELNES): these oscillations are in a range of 50eV after the peaks and they display smaller intensity. These features are believed to be caused by neighbouring atoms, for example in terms of local joint density of states [109], molecular orbital theory [110] and crystal-field splitting [111, 112]. This last effect is a break of degeneracy of states due to the configuration of the surrounding atoms, which modifies the energy levels.

These formulae are essential for the quantitative analysis of EELS spectra, as the double differential cross section (see eq. 2.25) can be related to the integrated intensity of an EELS edge to the areal density of a material (see par. 2.4.2.2).

2.4.2.2 EELS

Electron Energy Loss Spectroscopy (EELS) is a technique which creates spectra of electrons leaving the electron dispersed by energy loss: this reveals a wealth of valuable information about the sample, since most atoms and even bondings have a characteristic energy loss pattern.

This technique requires an instrument and settings similar to that of TEM, so the two are frequently found together, even though they developed separately. However all EELS data in this work were acquired from a spectrometer attached to a dedicated STEM instrument. The ideal conditions for EELS are in fact similar to those of STEM imaging, since a tiny electron probe of know energy is moved across the specimen (see fig.2.4). On the other side, various scattered electrons are collected selectively, according to their angle of scattering and energy range (detection may be different from STEM). As for the STEM, a well controlled electron probe improves spatial resolution (since it interacts with a limited area of the specimen) and reduces the spread in the response. However, a good signal-to-noise ratio requires higher intensity then STEM, so a wider electron probe is employed. The C1 lens and the condenser aperture allow a bigger part of the electron flux to focus on the specimen (see fig.2.4): this setting retains some aberrations, but it is reasonable because direct imaging in not a priority.

The incident angle is then set at about 30 mrad while the collection one varies greatly according to the specimen and the objective of the investigation. However, it is generally in the order of 10-100 mrad. The incoming energy is that of the microscope, so often about 60-300 keV, and the range of collection includes losses of few thousands of eV at most.

EELS Spectrum It is helpful to divide the analysis of the EELS spectrum in two parts, low losses and core losses, because of different intensities and physical processes involved.

Low losses spectra are concentrated before 100 eV. The most intense feature is called Zero Loss Peak (ZLP) (see 2.16) which corresponds to weakly interacting electrons from the beam, passing through the specimen with little energy losses. Because inelastic scattering is relatively unlikely, this intensity is order of magnitude bigger than the other signals. Main low loss signals are related to plasmons.

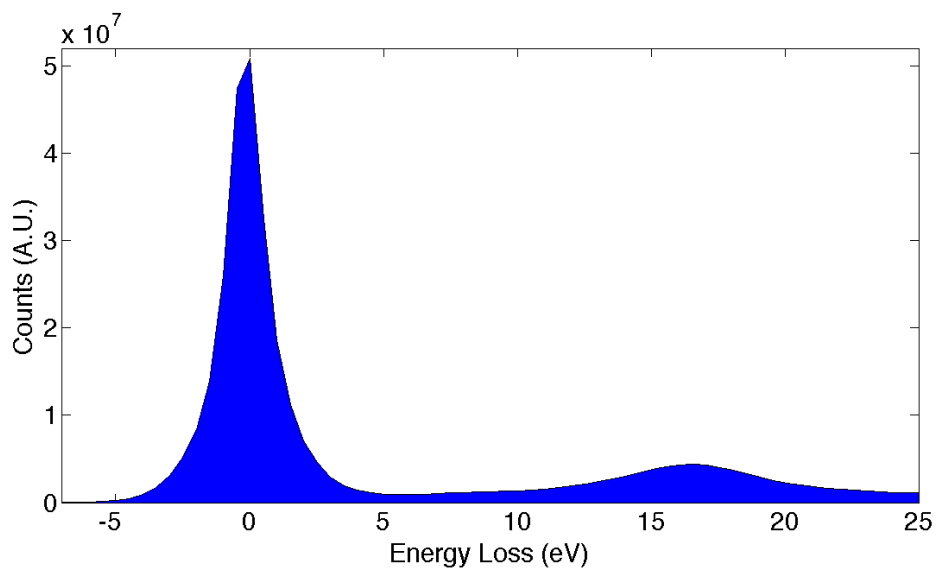


Figure 2.16: EELS spectrum at low energies of a Zirconium alloy specimen. The Zero Loss Peak (ZLP) is clearly seen on the left, at 0 eV, while the *Zr* plasmon peak is located at about 17 eV. Courtesy of Kirsty Annand.

Core losses can be present from 50 eV on (such as chromium and iron $M_{2,3}$ edge [70]), but they are more easily observed above one hundreds eV (e.g. at 470 eV in fig.2.17). They originate from interactions of the electron beam with atomic orbitals: more details are presented in sec. 2.4.2.1. Quantification is possible, once different cross sections of various elements are taken into account.

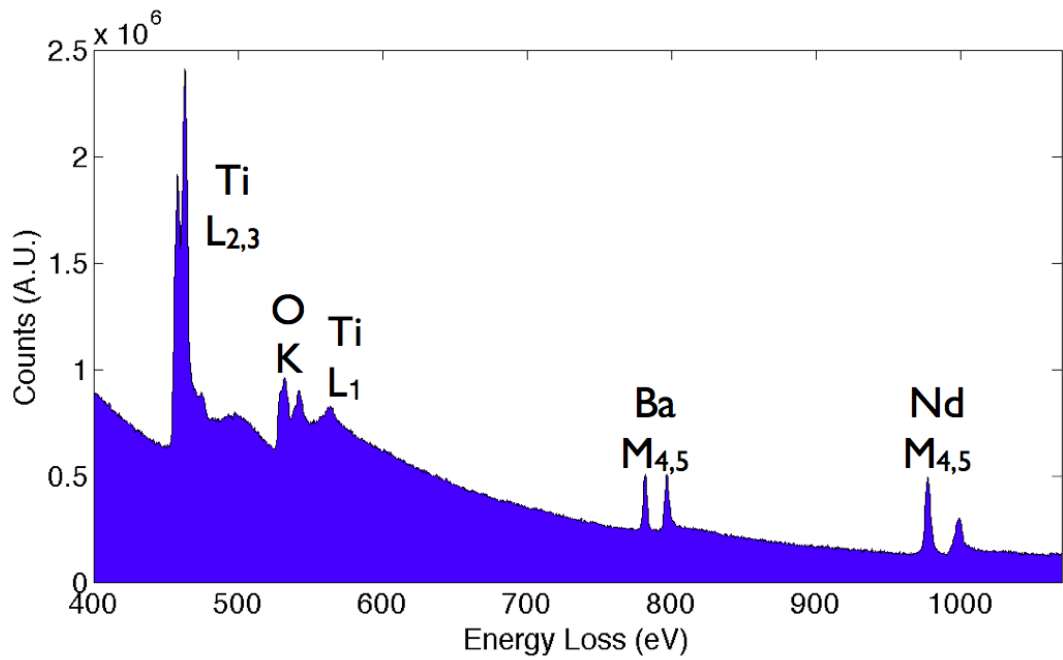


Figure 2.17: An example of EELS core loss spectrum of $Ba_{6-3x}Nd_{8+2x}Ti_{18}O_{54}$. Here, Ti , Ba , and Nd peaks are labelled with the related EELS edges, they correspond to those used later in this work. Additional features in the 500-600 eV region were not considered but are likely due to oxygen and further titanium contribution to the spectrum.

The background in the core loss energy range obeys a power law decay, at least in thin specimens

$$F(E) = AE^{-r} \quad (2.36)$$

where A and r are fitting parameters [70]. It is caused by various excitation mechanisms such as plasmons, tails of core-loss edges at lower energy and Bremsstrahlung [70]. It can be reliably fitted and removed, allowing to quantitatively analyse and compare the features in the spectrum. As mentioned before, the elements in the specimen can be identified by their specific energy loss peak, when associated to theoretical calculation of differential cross sections for most common shell ionisations [113, 114]. These features can provide information beyond the elemental identification, such as density of state or coordination number, so a description of related models is necessary.

Quantification The background in the spectrum can be reliably fitted and subtracted so analyses and quantification (both relative and absolute) are possible. Automatic routines are based on integration of entire sawtooth shape: this includes the spread of the signal to higher losses, due to ELNES and elastic scattering; on the other hand, the intensity peak alone can be influenced by near-edge structure [70].

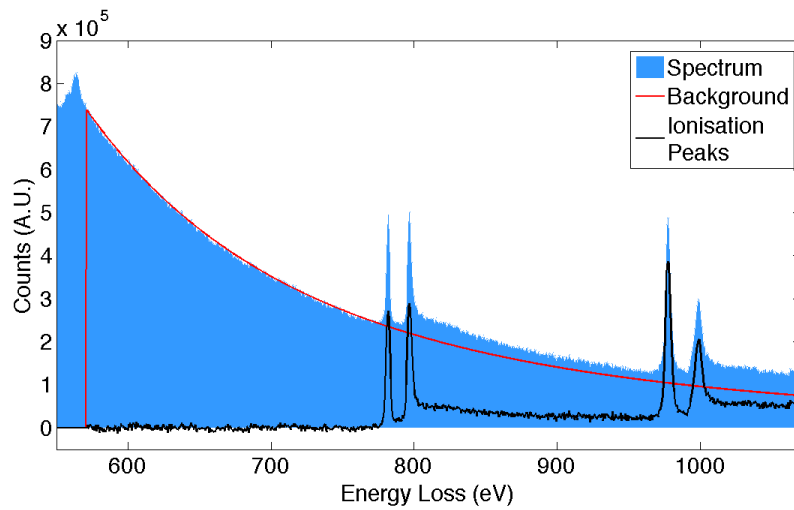


Figure 2.18: EELS spectrum with background (in red) and signal (in black). Ionisation thresholds can be clearly identified, after background subtraction.

The quantification algorithm aims to find the areal density N of a given atom, which is linked to the integrated density of the peak I_i by the following formula

$$I_i(\beta, \Delta) \approx NI(\beta, \Delta)\sigma_i(\beta, \Delta) \quad (2.37)$$

where I is the integrated energy loss spectrum, for a given angle range β and energy interval Δ [70]. I is usually approximated with the low loss region, which already accounts for roughly 99% of the intensity. σ_i is the calculated cross section for a given i shell and it requires careful estimation to grant reliable quantification. First, as a function of energy and angle, it is treated as differential cross section $d^2\sigma/d\Omega dE$. GOS formulation, based on hydrogenic model (described in 2.4.2.1) represents the simplest approximation, which neglects chemical environment or molecule orbitals influencing high energy states and responsible for ELNES features. However, integration over such fine structures may account for the cross section and still proves to be reliable within the hydrogenic model: it is estimated to be correct within 5%, when a range of energy of 20 eV or more is included in the integral [115]. The main shortcoming of this model is that it can only provide absolute cross section and not differential one, so it has to be calculated for every new setting and value of energy and collection angle. This is especially important as each specimen may require dedicated settings and a wide range of parameters could be used. This flexibility is required to handle different atomic numbers which modify the angle distribution of scattered electrons, which may overlap with different signals, such as elastically scattered diffraction patterns.

In order to satisfy this requirement Hartree-Slater method was introduced, because it allows to parametrise GOS, and then cross section, as functions of energy and wavenumber (which is linked to collection angle). This proves to be accurate as far as the assumption of ionisation transition to the continuum energy level E_t holds, while it is less precise in case of excitation to other atomic or molecular states.

An alternative solution is the use of well-known and standard material as a reference for specimen investigation, but it can be difficult to provide the necessary purity of composition down to the nanoscale.

The relative quantification is based on the following formula

$$\frac{N_a}{N_b} = \frac{I_{ia}(\beta, \Delta_a) \sigma_{jb}(\beta, \Delta_b)}{I_{jb}(\beta, \Delta_b) \sigma_{ia}(\beta, \Delta_a)} \quad (2.38)$$

where i and j are the two shell signals to be compared and Δ_a and Δ_b are two different energy windows [70].

Incident and collection angles α and β may be different between the investigations of the two materials, because of change of probe size (directly dependent on α) and improvement of signal intensity over the background (due to β). A small collection angle β (around 5-10 mrad) enhances the signal for low-energy edges, while wider angles increase intensities of high-energy features [70], even though such conditions may include diffraction signals [116].

In order to account for different angle settings, a correction factor was introduced for differential angular distribution of core-loss intensity. First, the intensity has to be calculated by integration over incident angle α [70]

$$\frac{dI_k}{d\Omega} \propto \int_{\theta_0=0}^{\alpha} \int_{\phi=0}^{2\pi} \frac{dI}{d\Omega} \frac{1}{\theta_k^2 + \theta_E^2} \theta_0 d\theta d\phi \quad (2.39)$$

where θ and ϕ are polar coordinates, θ_0 describes angle from optical axis which nominally ranges from zero to α . θ_k is the angle of inelastic scattering, given by $\theta_k^2 = \theta^2 + \theta_0^2 - 2\theta\theta_0 \cos \phi$ (see fig 4.19 eels). θ_E represents the Lorentzian function width, $\theta_E = E/(\gamma m_0 v)$, where $E \approx E_k + \Delta/2$. Previous formula can be calculated analytically [117].

The effect of collection angle β on core-loss intensity I_k , such as in case of an aperture, is expressed as [70]

$$I_k(\alpha, \beta, \theta_E) = \int_0^{\beta} \frac{dI_k}{d\Omega} 2\pi\theta d\theta \quad (2.40)$$

Thanks to previous equation we can define a F_1 factor of reduction of core loss intensity I_k , due to convergence angle of the beam.

$$F_1 = \frac{I_k(\alpha, \beta, \Delta)}{I_k(0, \beta, \Delta)} = \frac{2/\alpha^2}{\ln[1 + (\beta/\theta_E)^2]} \int_0^\beta \ln \left[\frac{\psi^2 + (\psi^4 + 4\theta^2\theta_E^2)^{1/2}}{2\theta_E^2} \right] \theta d\theta \quad (2.41)$$

Due to influence of θ_E , F_1 changes with every ionisation edge, which means for every measured material concentration.

An additional correction factor, F_2 , can be defined for absolute quantification as

$$I_k(\alpha, \beta, \Delta) \approx F_2 N \sigma_k(\beta, \Delta) I(\alpha, \beta, \Delta) \quad (2.42)$$

Value of F_2 changes according to incident and collection angles α and β : $F_2 \approx (\alpha/\beta)^2 F_1$ for $\alpha \geq \beta$; $F_2 \approx F_1$ for $\alpha \leq \beta$ [70].

Frequently the direct absolute quantification is difficult, because of inaccuracy of cross section calculation, so relative quantification is preferred. However, if a single element is somehow measured otherwise, relative quantification can then provide concentration of all others, by measuring ratio of intensities (see previous formula). Standard specimens can provide reference spectra and intensities. Crystallographic consideration can provide useful insights in the absolute quantities, allowing relative quantification to complete the picture by working out ratio between known and unknown element. A slightly different approach is used in this work: a crystallographic consideration [118] was used, which assumes a HAADF specimen to have the same number of atoms in neighbouring columns, due to limited variation of thickness and signal intensity on a nm scale (see fig. 2.19). However, other causes of intensity variations were reported: the channeling effect causes a modulation of the electron intensity, a phenomenon called Pendellösung effect [70]; a contribution of neighbouring sites to the EELS signal was also calculated as a consequence of thermal scattering [119].

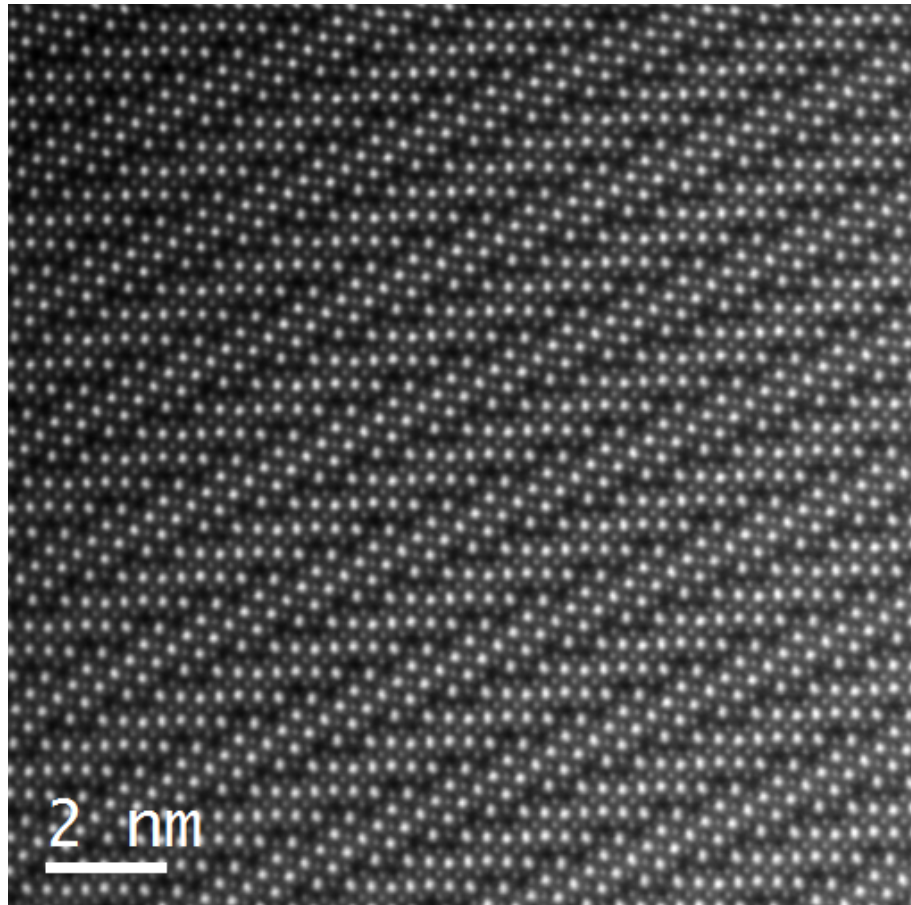


Figure 2.19: HAADF image of $Ba_{4.5}Nd_9Ti_{18}O_{54}$ along $[010]$ direction. Columns of atoms are parallel to b-axis and number of atoms in each of them is assumed to be similar, given that little thickness variation is noticeable. Ba and Nd sites are brighter and clearly visible, Ti can be noticed between the cations, even though it is more dim. Oxygen is not visible in this image.

If the number of atoms are assumed to be roughly equal, intensities can be normalised, based on the most reliable signal.

2.5 Conclusions

A general overview on electron microscopy, for what is relevant to this work, was provided in this chapter to introduce and explain relevant techniques and their results. Basic concepts of electron microscopy were introduced, together with related theory of electron scattering was presented. Relevant techniques were presented after their theoretical background was introduced, with a presentation of working principles, acquisition, results and interpretations and finally some important components.

Chapter 3

Data Analysis Methodology

3.1 Introduction

The work in this chapter is heavily based on interpretation of data, as much as acquisition of them, so that proper quantitative information could be extracted from the sample. This chapter is then meant to explain the rationale and procedures that guided the data processing and calculation of this current study. This is intended to help comprehension of our data as well as favouring reproduction of similar experiments.

A brief presentation of general statistical principles is provided in the next section, followed by a detailed description of data acquisition parameters and dedicated scripts for processing (section 3.3). Finally there is an introduction to Dr. Probe software [123] (developed by our collaborator Dr. Barthel) which we will later be used for simulation based on our conclusions, in order to both confirm and integrate our results (section 4.3).

3.2 Principle of Statistical Analysis

A large experimental dataset will inevitably contain a significant variance between measurements. There are a number of reasons for this, caused by different sources of noise. First, extrinsic sources can disturb the measures: for example stray electrons might be collected by detectors [70]. Moreover, electronic components may add noise as well, e.g. as a consequence of instability in power supply. Other contributions of digital detectors to the variance are limited sensitivity or dynamic range, low precision which causes quantisation noise: a limited number of values can be recorded by digital detectors, so measured quantities are rounded and therefore introduce an error. Physical processes contribute to noise as well, for example, shot noise. This is a statistical effect, which is caused by variations of the signal at each measure, due to the probability of emission (or detection) of a signal over time, e.g. the electrons in a beam have a chance of interactions with the specimen, described in terms of cross-sections (see sections 2.4.1 and 2.4.2.1). A limited number of readings might be biased because of the detection of improbable events, while an extended investigation is more likely to

present a reliable collection of data. This difference is caused by the shot noise, which should follow the Poisson distribution. Finally, variations of actual properties between measurements on neighbouring areas are possible, because of statistical distribution within the specimen itself (e.g. dopant levels on different atomic columns).

A proper error function can describe the distribution of results and provide an estimate of the original value before the noise contribution. By far, the most common description of errors, which are assumed to be random uncorrelated events, is the Gaussian function (also called normal distribution)

$$g(x) = \frac{1}{\sigma\sqrt{2\pi}} \exp\left[-\frac{1}{2}\left(\frac{x-\mu}{\sigma}\right)^2\right] \quad (3.1)$$

Here it is normalised so that its integral is equal to one [124]. σ is the variance and μ is the expected value: formulae to obtain these parameters are different for each probability distribution, in case of the Gaussian function

$$\mu = \frac{1}{n} \sum_{i=1}^n x_i \quad (3.2)$$

$$\sigma^2 = \frac{1}{n} \sum_{i=1}^n (x_i - \mu)^2 \quad (3.3)$$

where n is the number of observed events [124].

The main reason to focus on Gaussian function is the central limit theorem [125], which states that a collection of independent and identically distributed random variables converges to a Gaussian function as the number of data, n , tends to infinity. This justifies the use of normal distribution (and related formulae for expected value and variance) whenever a homogeneous distribution of error is assumed. In this work, the expected and relevant systematic errors, like drift distortion in HAADF images and thermal scattering in EELS data were corrected, as detailed in sections 3.3.1.1 and 3.3.1.3. The resulting sets of data were assumed to present only random and uncorrelated errors (an example is shown in fig. 3.4), so the Gaussian distribution was used to calculate statistical results.

3.3 Algorithms for the Quantifying Atomic Resolution Imaging and Spectroscopy

The following section describes the statistical treatment of the atomic resolution datasets used in chapter 4. In particular, we focus here on the algorithms used to evaluate

atomic scale structures and chemistry of the materials in chapter 4. A list of the related Matlab scripts used for this work can be found in the Appendix.

The crystalline structure and the chemistry of our samples was investigated by HAADF STEM and EELS to create a model of the unit cell and chemical composition of $Ba_{6-3x}Nd_{8+2x}Ti_{18}O_{54}$ to verify and possibly refine the previous Rietveld refinements [66] with an independent set of data.

Both HAADF and EELS analyses were performed at the SuperSTEM facility using an aberration-corrected Nion UltraSTEM (Nion Inc., Kirkland, WA) instrument equipped with a Gatan Enfina spectrometer (Gatan Inc., Pleasanton, CA). For both imaging and spectroscopy, a probe convergence angle (α) of 30 mrad was used. This is the largest aberration-corrected angle available for the SuperSTEM microscope: this setting can provide the smallest aberration-free electron probe for STEM, as stated by Abbe diffraction limit (see formula 2.8).

HAADF imaging was performed using an annular detector with an inner angle of 100 mrad and an effective outer angle of 185 mrad. Electron energy loss spectra were collected using an acceptance angle (β) into the spectrometer entrance aperture of 31 mrad. This angle was chosen again as the widest angle which does not present aberration: a wide angle would allow to collect a bigger part of the signal from the specimen, but aberrations from the microscope and the spectrometer come into play at higher angles.

3.3.1 Atomic Structure Refinement from HAADF Imaging

3.3.1.1 Atomic Column Position Refinement

The achievable resolution for HAADF data is better than 1 Å in modern aberration-corrected STEM instruments, such as the UltraSTEM used in this work, which allows the resolution of individual atomic columns along many projections of most materials. This led to early studies of grain boundaries with atomic resolution [126, 127]. If atomic columns are well resolved, then the positions of these columns can be measured with picometre precision using Gaussian peak fitting, since the profiles of the column images in HAADF are well approximated by a Gaussian. This solution proved to be suitable when considering the results (*a posteriori*), but the mathematical expression of intensity of atomic columns in HAADF data is unknown. On a stationary specimen, if the aberrations were corrected, the intensity function is likely to result from a convolution of three factors: the profile of the tip of the FEG gun (approximately a Gaussian function, 0.5-0.8 Å wide); the probe formation aperture (see paragraph 2.3.3) which causes the intensity to behave according to a Bessel function; the atomic potential, roughly 0.2-0.3 Å wide. The aperture is likely to provide the biggest contribution, with the others causing only a small broadening of the intensity profile. A Gaussian function is then a reasonable approximation of the main region of a Bessel pattern. Unfortunately, direct Bessel interpolation was not implemented in our software packages.

The Gaussian fit allows direct quantitative analysis and modelling of structure. This requires fitting of pixelated image, as those from STEM, in order to locate the centre of mass of single atomic columns [128] and then work on the statistics of those fits to create an average model and reduce the variance. This technique increases the precision in the localisation of atomic sites: it was first used to study the structural changes in crystallographic planes, due to the strain caused by epitaxial mismatch [129]. It is based on peak position measurements of atomic resolution images, which is then averaged over many unit cells, in order to obtain quantitative results at the picometre scale. 2D Gaussian fitting was then employed to improve quantitative description of crystallographic structures in TEM [130] and STEM [131].

In our work atom peak positions from the HAADF data (such as those shown in fig. 2.19) are located and refined by Gaussian peak fitting using either iMtools [132] or Image Analysis plug-in of Digital Micrograph¹ in order to provide coordinates of atoms columns. First, background subtraction is performed, either automatically (by iMtools) or by selecting the degree of a polynomial which will fit the background (in Image Analysis). Typically 1st or second degree is enough but a visual investigation is recommended. The following step is the definition of site radius (in pixel, since the algorithm ultimately works on images), which can be easily estimated by zooming in the image until single pixels are clearly visible, so the approximate number of pixels covered by an atoms column is obvious. The software packages can then interpolate two dimensional Gaussian functions (shaped either as an ellipse or a circle) to fit the atomic columns' intensity in the HAADF raw data. This results in a list of parameters related to the fitting process of each site:

- Coordinates of site (from 2D Gaussians fitting)
- Amplitude of Gaussian functions
- Variance/Width
- Orientation of the major axis (in the case of an elliptical fit)
- Lowest and highest values (fitting is relative to the radius of the site, so it may not correspond to lowest intensity pixels)

Although all atoms sites were mapped, only those in a limited area were actually used: this happened because the HAADF image shows differences which grow as the distance between the considered areas. This can be noticed in fig. 4.6, as our model of unit cell is compared to the original data and the replicated ideal cells tend to differ progressively from the HAADF data. Such behaviour is caused by the drift distortion in STEM, as the sample moves during the acquisition: distant areas show larger distortion because more time passes between their imaging, so the specimen can drift further away. As a

¹A recent alpha version kindly provided by our collaborator, Bernhard Schaffer of Gatan.

consequence, our acquisitions did not cover all the available data, in order to probe a relatively homogenous area and avoid introduction of errors from distortions.

A MATLAB script was used to detect almost automatically a number of unit cells. The algorithm was tested on the well-known perovskite structure of $BiFe_{0.5}Mn_{0.5}O_3$: the HAADF image in fig. 3.1 (courtesy of Dr. I. MacLaren) was analysed with the Image Analysis plug-in of Digital Micrograph. It provided a 2D Gaussian fit for Bi, Fe and Mn sites.

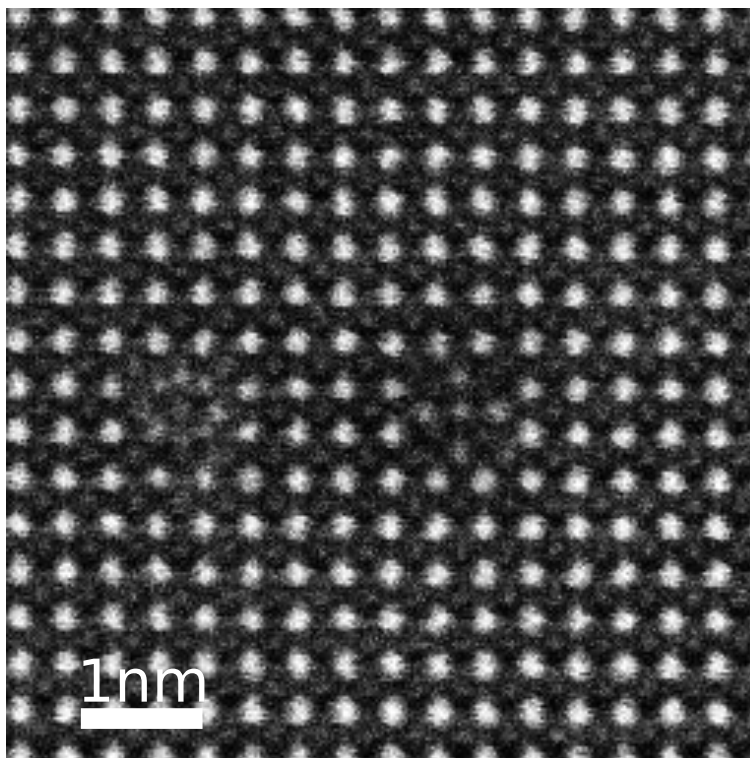


Figure 3.1: HAADF image of a $BiFe_{0.5}Mn_{0.5}O_3$ specimen. The perovskite structure is evident and the bright Bi atoms can be distinguished from the dimmer Fe and Mn ones. Oxygen is not visible. Two precipitates can be seen in the centre of the image. Courtesy of Dr. I. MacLaren.

The coordinates resulting from the fitting process are presented in fig. 3.2: the perovskite structure is conserved in most of the area, although some sites were badly fitted. It was also possible to select Bi or Fe sites, so the coordinates of the different atomic columns can be plotted. There are few errors in the attribution of sites to the right element, but this does not hamper the identification of the structure because only the coordinates are considered in the script. It is worth noting that the coordinates are expressed in pixels, as it is not possible to retain the scale from fig. 3.1.

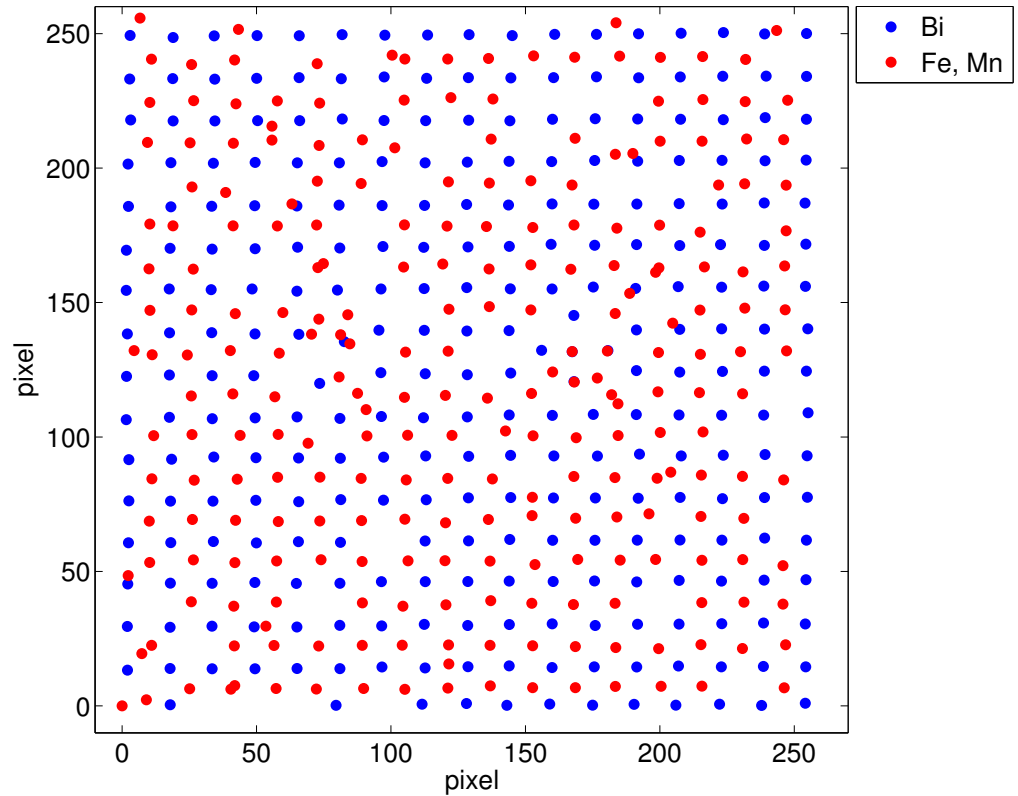


Figure 3.2: Coordinates from the fitting process on fig.3.1. Some sites were not fitted correctly, but the perovskite structure is conserved.

The unit cell of $BiFe_{0.5}Mn_{0.5}O_3$ is cubic so it appears as a square along the pseudocubic $\langle 100 \rangle$ directions [133]. It is possible to identify many unit cells of $BiFe_{0.5}Mn_{0.5}O_3$ in fig. 3.2, so one was selected as a “model“ for the identification of some others (namely 33 cell in total). The first cell (plotted with black dots in fig. 3.3) was chosen approximately in the central area, since it is deemed to be less affected by distortions: this allowed to provide the best possible model for the search of other unit cells. The coordinates of the five sites of the first cell were inserted in a script, which calculated the lattice constants in order to identify more cells. In fact, these characteristic distances describe the periodicity of features in the crystal and then the relative positions of the cells. However, a small margin of error is allowed, due to noise in the HAADF image affecting the fitting process. In case of uncertainty, the script asks the user to decide whether the identification of a given site is correct. This led

to identification of 33 cells, reported in fig. 3.3 as black squares: areas with obvious fitting errors or precipitates were not investigated.

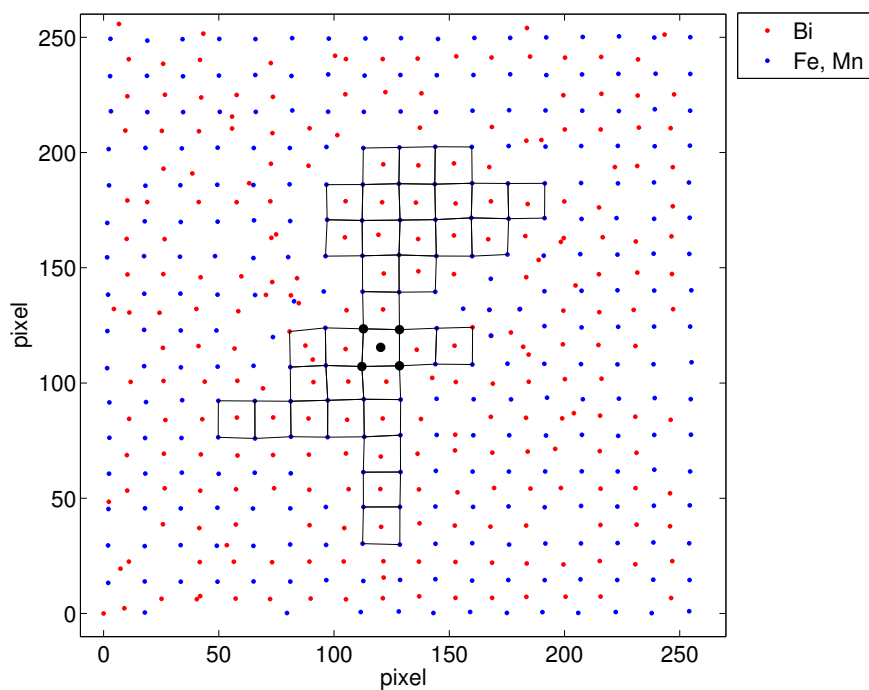


Figure 3.3: Unit cells' identification from coordinates of fig. 3.2. The wide black dots correspond to the sites of the first unit cell, which was defined by selecting individual coordinates. The other cells, which are marked by black squares, were identified by a semi-automated script.

The identified unit cells were overlapped to help the comparison between them: the central bismuth site was chosen to be unique and common for all of them, to provide a reference for the alignment. A representation of the difference between those cells can be seen in fig. 3.4, where the central bismuth site is overlapped. The picture seems to suggest that the coordinates present a random distributed error.

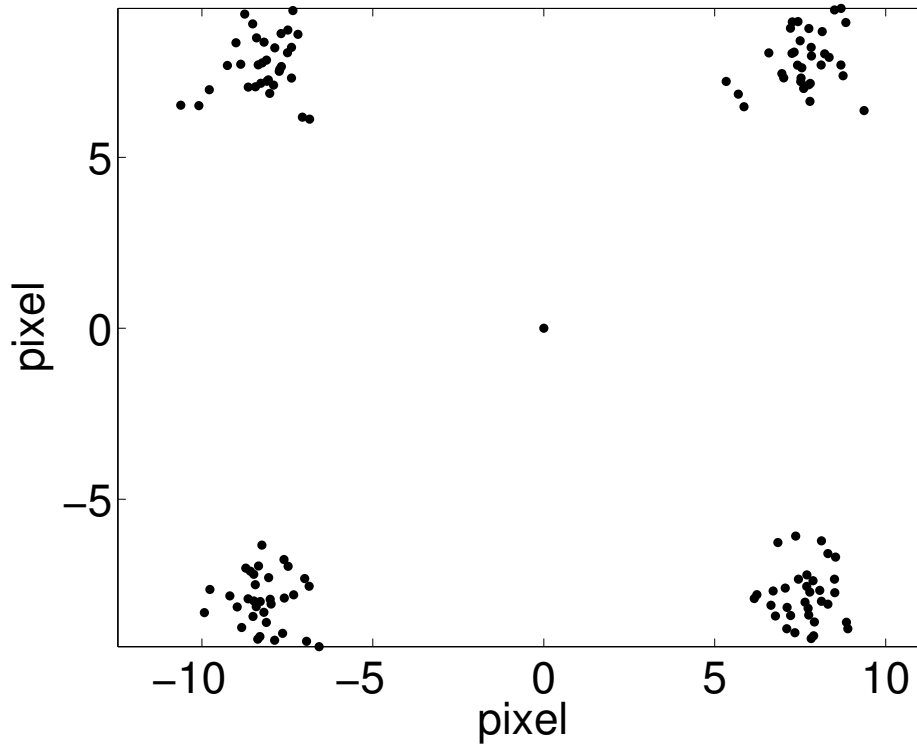


Figure 3.4: Overlap of unit cells from fig. 3.3, aligned accordingly to the central bismuth site. The distribution of coordinates can be seen in the corners.

In order to reach a model of the unit cell, two approaches are possible in this case: an average correction of all errors and distortions or specific adjustments for every cell. Both solutions were used: the results for the different stages of the algorithm are presented and the two final unit cell models are compared. The first stage was a rotation of the cells, which ensures that the bottom sites are aligned to a horizontal line. The rotation transformation is based on the following formula

$$\begin{pmatrix} x' \\ y' \end{pmatrix} = \begin{bmatrix} \cos\theta & -\sin\theta \\ \sin\theta & \cos\theta \end{bmatrix} \begin{pmatrix} x \\ y \end{pmatrix} \quad (3.4)$$

Where x and y are the original coordinates, while x' and y' are the rotated ones. ϑ is the anti-clockwise rotation angle. On the same set of data from fig. 3.4 two different rotations were applied: a common rotation (as seen in the left image of fig. 3.5), based

on average position, and a specific rotation to correct every single cell (result in the picture on the right in fig. 3.5). The difference between these two transformation (in fig. 3.5) looks negligible, probably because the required rotation was minimal (roughly in the range of 0.008-0.05 rad). This is a due to the original HAADF data being already close to alignment to a horizontal axis.

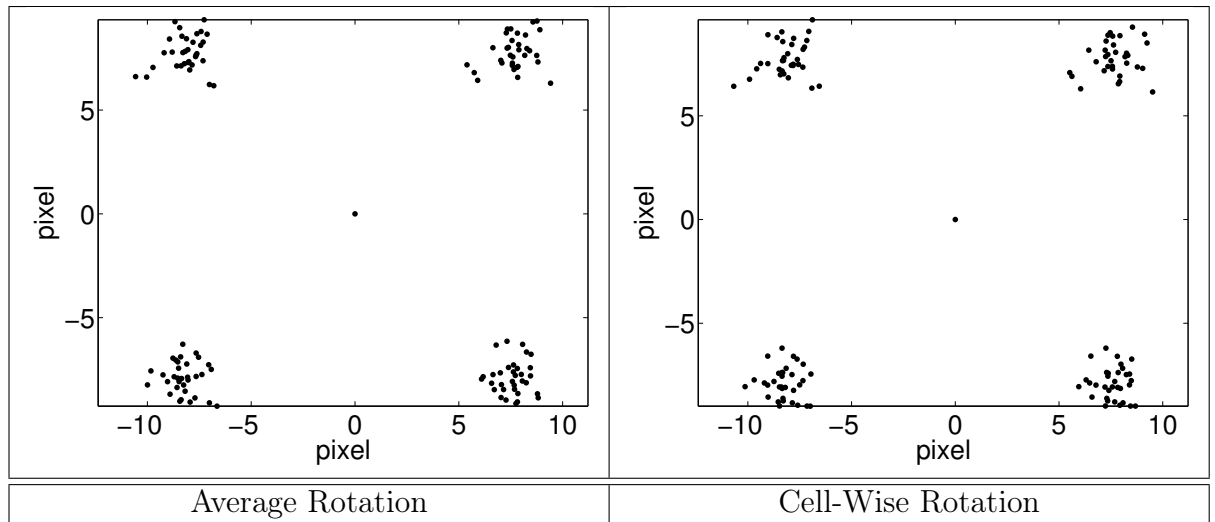


Figure 3.5: Slight rotations of data in fig. 3.4, in order to align the bottom sites to horizontal axis. In the left image, the same rotation was applied to all coordinates. The angle of the rotation was calculated accordingly to the average position of the sites. In the right picture, each cell was rotated by a different angle, according to the position of its bottom sites.

The second transformation required to match the standard unit cell is the shear, which aligns vertically the sites. It compensates the STEM drift distortion in the images, as the specimen moves during the measurement, causing an elongation in the detected structure. The shear transformation is based on the following formula

$$\begin{pmatrix} x' \\ y' \end{pmatrix} = \begin{bmatrix} 1 & \lambda \\ 0 & 1 \end{bmatrix} \begin{pmatrix} x \\ y \end{pmatrix} \quad (3.5)$$

Where x and y are the original coordinates, while x' and y' are the sheared ones. Value of λ is chosen to align left-hand sites vertically.

An average correction is shown in the left picture of fig. 3.6, starting from the data plotted in the left image of fig. 3.5; on the other hand, left-hand sites of each cell from the right picture of fig. 3.5 were aligned vertically. The results of this “cell-wise” shear correction are plotted in the right picture of fig. 3.6. While the left-hand sites are aligned as expected, little misalignment can still be noticed on the right-hand side. This happens because the shear was calculated to compensate the other sites and the distances between sites vary in each cell.

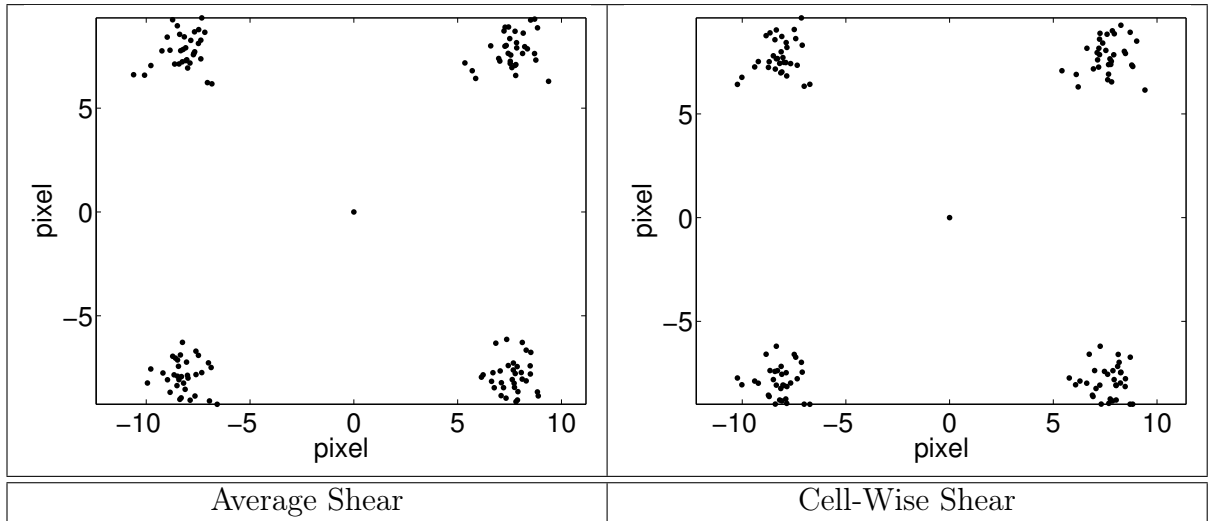


Figure 3.6: Shear correction on data from fig. 3.5. In the left image, the correction was based on the average position of the sites on the left-hand side, which were (on average) vertically aligned. In the right picture, the correction aligned vertically the positions of the sites on the left-hand side in each cell.

The structure of the cell is now approximately correct, but the coordinates of the central site and the corresponding standard deviation need to be estimated. The centre of mass approach is adopted here, where the central point is calculated as an average of all the other sites in the cell. This is inherently based on the single cells, so there is no “average approach” as opposed to “cell-wise” one. However, the same “centre of mass” method was applied to the different set of data presented in fig. 3.6, so the results change. The estimates for the central sites are shown respectively in fig. 3.7a (for the “average approach”) and 3.7b (from data originated by the “cell-wise” approach). This last one presents a much wider dispersion of the central site, possibly because the “cell-wise” transformation changed the cells singularly, increasing their relative differences, while the average approach maintained the dispersion constant, and this is reflected in the spread of the central coordinates.

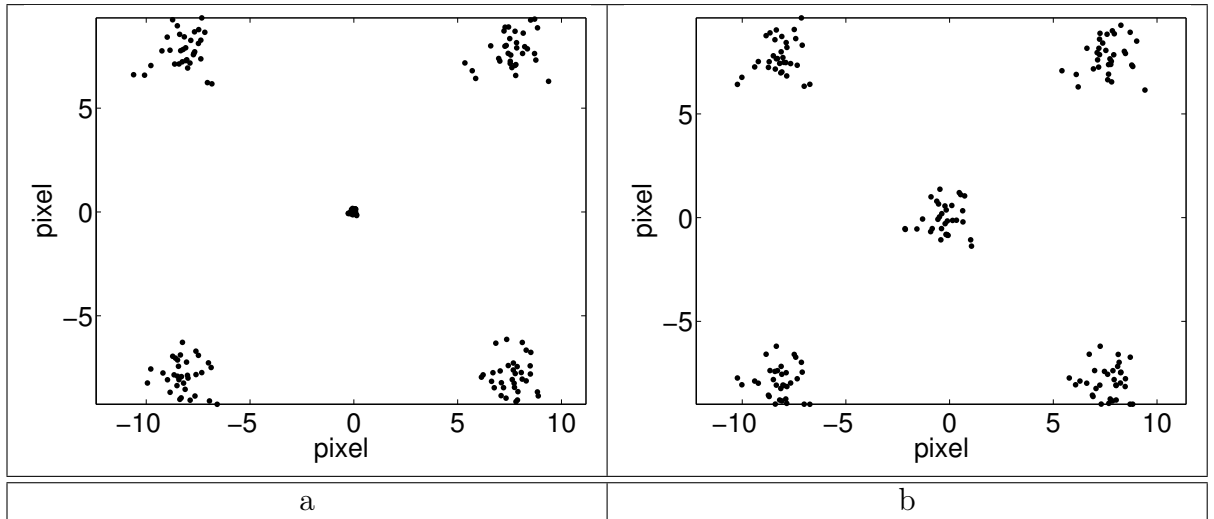


Figure 3.7: a) Centre of mass calculation of the central site, from the data shown in the left image of fig. 3.6, corresponding to the “Average approach”. b) Centre of mass calculation of the central site, from the data shown in the right picture in fig. 3.6, corresponding to the “Cell-Wise approach”.

The last transformation needed is the scaling, to express the distances in Å instead of pixels. Again, this was performed on an average and cell-wise manner (plots are not shown), so the size of the cells corresponds to the actual lattice constants of $BiFe_{0.5}Mn_{0.5}O_3$: 3.96535 by 3.91955 Å [133].

Finally all cluster of coordinates were averaged to calculate the final unit cell: this happened once again for both set of data. Standard deviations were calculated as well. The unit cell from the “average approach” and “cell-wise approach” are overlapped for comparison in fig. 3.8. This last plot shows a main difference in the central point, which exhibits a different position and standard deviation: it is likely a consequence of the two central point estimations. The values of standard deviation reflected the different dispersions of coordinates. The position of the central site varies as well, but not considerably. The other sites and standard deviations are all very close for both approaches. Interestingly, the standard deviations are similar to that of the central point from the “cell-wise approach”. This seems to be an advantage of this method, since it calculates a similar dispersion for all sites: this seems reasonable, given the same acquisition method was used for all. There are not direct data on the scattering of the central point: an estimation of the dispersion is required, resulting in some uncertainty.

The central point calculation is affected by the necessity of an estimation, in absence of direct data on its dispersion, so there is some uncertainty. The two approaches do not seem to alter greatly the final coordinates, but just the standard deviation.

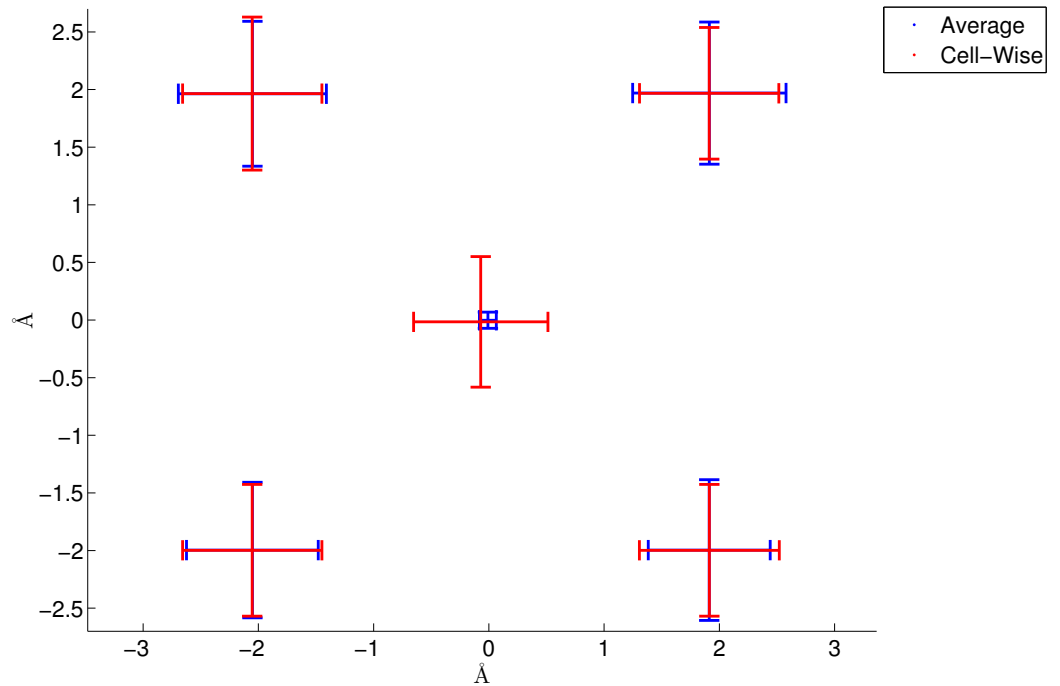


Figure 3.8: Comparison between the unit cells of each method. The main difference can be noticed in the central point. Error bars correspond to 3σ (standard deviation).

The effect of phonons in the data is not considered, but the results of this procedure on a $Ba_{6-3x}Nd_{8+2x}Ti_{18}O_{54}$ sample are later employed in a simulation of HAADF images, which includes a phonons' estimation (see section 3.4). The comparison with actual HAADF data shows an accurate match (see fig. 4.7).

3.3.1.2 Elliptical Fitting of non-round Columns

Some atomic sites, namely $Nd[2]$ and Ba ones (marked with black and red arrows respectively in fig. 3.9), consistently show some elongation at a given angle (see fig. 3.9). There seems to be a loose alignment between three sites ($Ba - Nd[2] - Ba$), as shown in fig. 3.9.

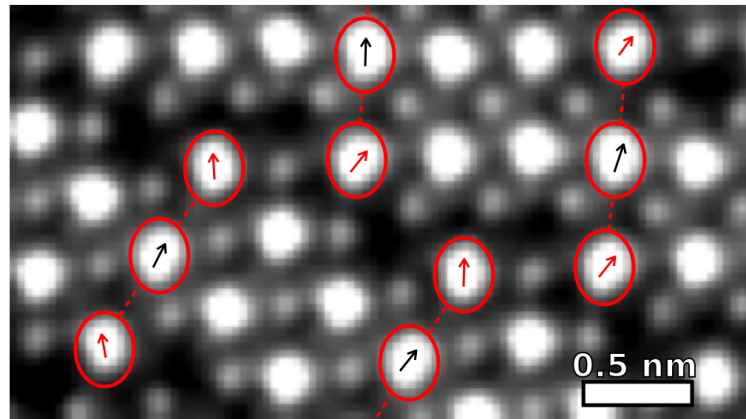


Figure 3.9: Zoom of HAADF acquisition of $Ba_{4.5}Nd_9Ti_{18}O_{54}$ along $[010]$ direction. $Nd[2]$ and Ba sites elongation are marked with black and red arrows respectively, presenting a rough alignment. The sites with similar orientation are linked with dashed red line.

This may be interpreted as a partial misalignment of atoms along a columns, so that its projection in HAADF STEM no longer looks circular (see fig. 3.10).

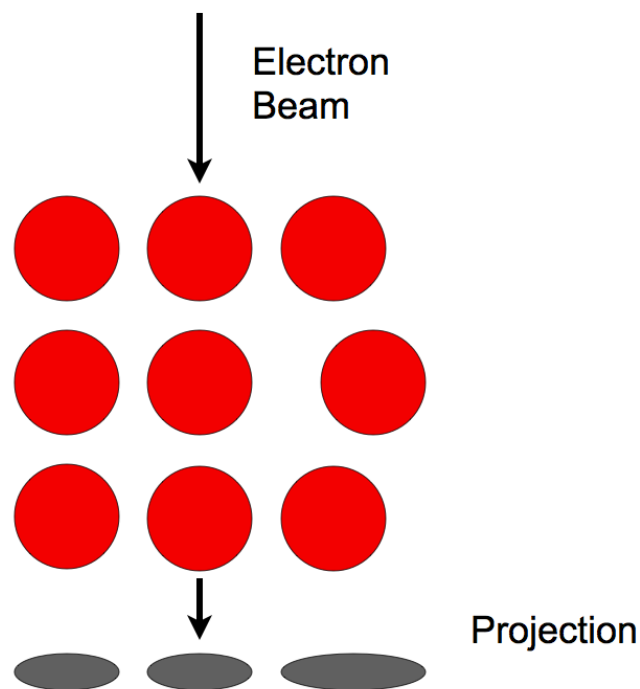


Figure 3.10: Schematics of an elongated atomic column site. The misalignment of an atom in the column result in the oblong projection, which is recorded by HAADF microscopy.

The measurement of these elongations can lead to a better description of the atomic positions in the column. Starting from previous Gaussian fitting results, the angles and width of sites can be listed. However, a new interpolation may be needed if the fitting was based only on the central part of each site, neglecting most of the elongation. A new fit with a wider radius proved sometimes beneficial in describing the extension of the atom columns and then their orientation.

The new fitting angles may need a correction, because of the ambiguity in the direction of the elongation. For example, two parallel ellipses may be fitted by angles pointing in the opposite direction, e.g. -90° and 90° . The average value would then be 0° , which is different from the original angles. This problem is resolved by setting a limited range of values, which is centred around the approximate average angle: a $0^\circ - 180^\circ$ range was used in this current study, where 0° corresponds to an angle pointing in the right direction. Any other angle was converted into the corresponding one within the range, for instance 270° would become 90° , which represents the same orientation. The average value is then bound to fall within the given range.

Since the original HAADF images undergo a rotation and shear transformation, some modifications are needed for these ellipse fits and their angles, similarly to the case of crystallographic structures above. Rotation and shear matrices were applied to the major axis of the elongated sites (resulting from the fitting), so that the angles and the extent of such columns were modified exactly as the unit cells. These modified values should then be compatible for the model of the unit cells.

Beside the distinction between $Nd[2]$ and Ba sites, a second difference was noticed: angles are approximately aligned along two directions, which seems to correspond to the “zig-zag” pattern of the global crystal structure (see fig. 2.19). Angles are then sorted according to both atomic sites and “zig-zag” orientation. Finally, average values are calculated for each subdivision. These orientations were then used to guide the creation of a refined unit cell, which accounts for these site elongations. This characteristic can be implemented in a unit cell by slight misalignment of atomic sites along their column, so that they do not overlap perfectly but form an elliptical shape. $Nd[2]$ and Ba atomic sites are then moved to match the elongation angle and extension, until the model overlaps the original HAADF image (see fig. 4.6). Once again, image rotation and shear are necessary for the two to match properly. The ultimate Rietveld refinements of the crystalline structures, based on all our results, are presented in the manuscript in preparation [134].

Finally, it is interesting to notice that the misalignments of atomic sites do not break the symmetry relations for $Pnma$ crystalline structures, as the deviations from the atomic column still obey those formulas.

3.3.1.3 Atomic Resolution Quantification of Column Cation Content

The process of EELS quantification is based on the theoretical framework discussed in paragraph 2.4.2.2. Here, we explain the actual procedure and the parameters used,

together with our internal standardisation approach used to produce chemically sensible results.

First, the elements of interest are selected, in our case *Ba*, *Nd* and *Ti* (when available). In particular the signals integrated above the $M_{4,5}$ edges for *Ba* and *Nd* (respectively at 781 and 796 eV for *Ba*, 978 and 1000 eV for *Nd*) and above L_{23} for *Ti* (edges at 456 and 461 eV, respectively) were used. All these edges have high intensity above the background with a pair of clear "white-lines" at the onset giving a good signal to noise ratio, as well as being well separated, allowing reliable background fitting.

The background is automatically extrapolated and subtracted from the spectrum. Then, the cross section σ_k is calculated with the Hartree-Slater model [135], based on GOS tables [114, 136], in the form of a double differential cross section $\frac{d^2\sigma_k}{d\Omega dE}$. This formulation can obtain the cross section of the experimental range of energy and angles by integrating the differential cross section. This process is performed in the standard quantification procedure on Gatan Digital Micrograph. It is then integrated over the relevant energy range for that given element and peak (see tab. 3.1) and the experimental range of angles: 30 mrad for convergence semi-angle and 31mrad for the collection. The collection angle is wider than the convergence one to detect all the undiffracted beam, which is then necessary to calculate the total integrated number of counts (I), used in the quantification formula later. The EELS intensity I_k is integrated over different ranges of energies for *Ba*, *Nd* and *Ti*: the parameters and the cross sections for each element are listed in tab. 3.1.

Element	Background Fitting Range (eV)	Edge	Integration Range (eV)	Cross Section (barns)
<i>Ba</i>	697.0 - 765.0	$M_{4,5}$	781.0 - 821.0	3654 ± 365
<i>Nd</i>	873.0 - 958.0	$M_{4,5}$	978.0 - 1018.0	1261 ± 126
<i>Ti</i>	407.0 - 447.0	L_{23}	456.0 - 481.0	3269 ± 327

Table 3.1: Parameters for elemental quantification from EELS spectra in Digital Micrograph. For all these elements, the angles were set to 30 mrad for convergence semi-angle and 31mrad for the collection. Beam energy was 100 keV. The power law formula was used for background fitting, cross sections were calculated using Hartree-Slater model by Digital Micrograph. Integration range was used for both cross section σ_k and element intensity integration I_k .

The areal density N (atoms/nm²) can then be calculated from following formula

$$I_k = NI\sigma_k \quad (3.6)$$

where I is the total integrated number of counts, while σ_k is the cross section, integrated over relevant angles and energies [135]. However, although I can be approximated by the zero loss peak, it is not always convenient to acquire it: an alternative is the relative quantification, which only requires the peaks of the related elements, in the core loss section of the spectrum. In fact, the relative composition may be calculated from following formula, without the need of the total intensity counts.

$$\frac{N_a}{N_b} = \frac{I_a \sigma_b}{I_b \sigma_a} \quad (3.7)$$

A more specific description is given in section 2.4.2.2 and [70]. An example of areal density mapping for different elements is fig. 3.11.

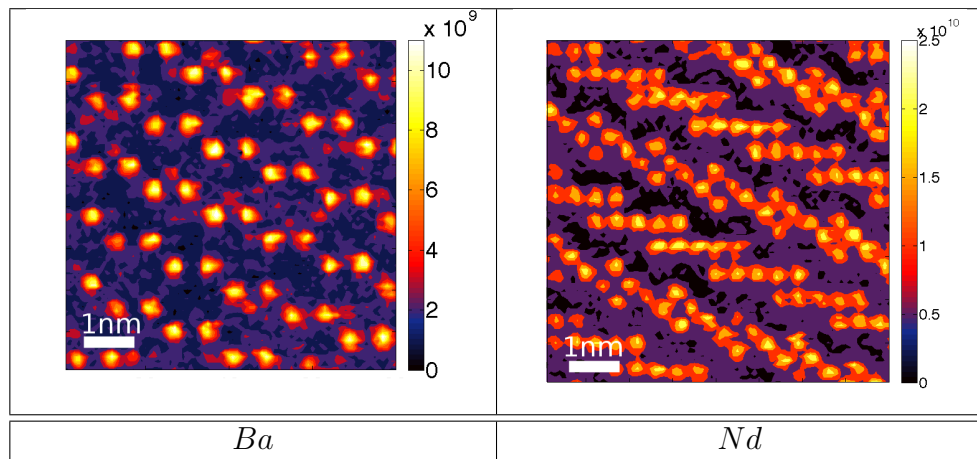


Figure 3.11: EELS-SI areal density image of Barium and Neodymium. The colour bar shows a considerable difference between the intensities of EELS signal of the two elements .

Our elemental maps show a huge difference in intensity throughout the specimen (see fig. 3.12) and between elements (see fig. 3.11).

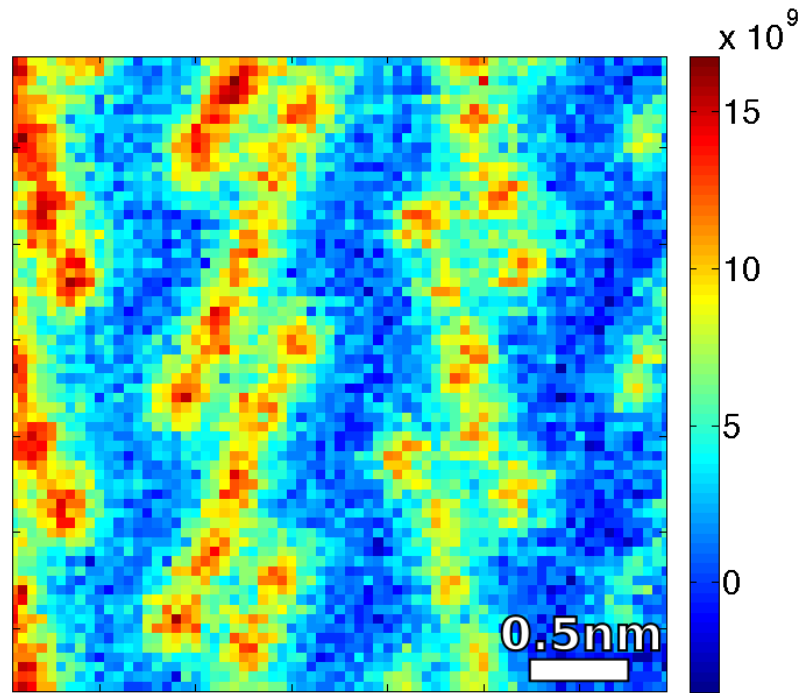


Figure 3.12: EELS-SI areal density image of Neodymium in a specimen with $x = 0.5$ composition. The colour bar shows the signal intensity. The influence of specimen thickness can be easily noticed, as intensity gradually decreases from left side of the image to right side of the image.

There are many factors which influence the intensity level, e.g. thickness variations. There is however a systematic difference in the peak intensity between different elements, which leads to doubt about the accuracy of the cross sections calculated by the Hartree-Slater model. In the case of *Nd* and *Ba* it involves the transition from 3d to 4f states and this latter orbital is quite hard to model [137, 138, 139]. A comparable calculation for *Ba*, its X-ray k factor, shows considerable differences in various models (see tab. 3.2), because they involve the description of high energy states, like d states. On the contrary, the k factor values for *Ti* tend to be quite similar, because they involve the easier and reliable model of simple orbitals like s and p . The k factor is relevant because it is proportional to ionisation cross section σ [69]:

$$k = \frac{(\sigma\omega a)_1 A_2}{(\sigma\omega a)_2 A_1} \quad (3.8)$$

where ω is the fluorescence yield, a is the relative transition probability (for example K or L edge, as detailed in tab. 3.2) and A is the atomic weight. The k factor represents a sensitivity factor, which converts X-ray intensity ratio to concentration one.

$$\frac{C_A}{C_B} = k \frac{I_A}{I_B} \quad (3.9)$$

k values based on reference samples have been reported in the literature [69], in particular those based on iron are labelled k_{AFe} : the values and amount of variation can be seen in tab. 3.2. The factor refers to Ba (L edge), which means that an electron is promoted from the L shell to the empty states beyond the Fermi level.

Moreover, a normal range of relative error for k factor is already considered to be 10-20%, mostly because of cross section estimation and detector parameter [69]. Neodymium cross section is believed to show similar problems, since it involves 4f destination states again, while Titanium shows less variance between the theoretical results.

Element	Theoretical Cross Section Method for k_{AFe} factor					
	Mott-Massey [143]	Green-Cosslett [144]	Powell [145]	Brown-Powell [146]	Schreiber-Wims [147]	Zaluzec [148]
Ba (L edge)	2.97	not available	2.52	2.25	2.49	2.83
Ti (K edge)	0.892	0.869	0.853	0.888	0.807	0.835

Table 3.2: List of theoretical X-ray k_{AFe} values for Ba (based L edge) and Ti (K edge), according to different theories [69].

In addition to the inaccurate cross section, there was another source of error, due to thermal electron scattering. The EELS results are likely to include an overrepresented contribution from Nd columns, because thermal scattering spreads the electrons of the STEM probe over neighbouring sites: many Nd columns are then able to channel the electrons, influencing the EELS elemental maps and eventually resulting in an exaggerated Neodymium content. A similar effect was reported in literature for strontium titanate [119]. In principle this could happen for every column in the specimen, but Nd sites are more numerous (see fig. 4.2).

Thus we believe the calculated areal densities were not accurate enough for our study and a normalisation of the data was necessary. This was performed using known facts about the crystal structure in a similar manner to Warusawithana [118]: since all the columns have the same number of atoms, the EELS quantification of the various element should be similar. On the contrary, our data show a constant difference in density between Ba and Nd , so a correction was applied to obtain the same relative density for both elements: namely, the Ba density was increased by 2.5216.

These results originate from the relative quantification of *Ba* and *Nd*, using *Ti* as a common reference: the intensity of titanium was averaged over the 4 or 5 sites surrounding *Ba* and *Nd*, before the calculation of intensities and the following correction. This technique accounts for variation of the local thickness of the specimen as well, because *Ti* signal acts as an internal reference: any change in the intensity due to the thickness is likely to be comparable for *Ba*, *Nd* and *Ti*, so the relative quantification remains mostly unaffected.

A second normalisation was carried on, based on the symmetry relations described in 3.3.1.1. The areal density of the sites with same symmetry were averaged, because they are equivalent from the crystallographic point of view. A global variance was then calculated for all of them.

3.4 Principle of STEM Image Simulation

Simulation of electron propagation in a bulk material can replicate the physical interactions happening in a electron microscope (for either TEM and STEM), in such a way that electrons' wavefunctions can be calculated during and after the scattering process from the specimen. Those wavefunctions can be converted into images, corresponding to those of a real microscope analysing the simulated structure. This is a considerable help in the interpretation of results, since data from electron microscopes may be hard to interpret and simulation can provide the representation of an expected structure, which can be compared to experimental data. Also, a number of parameters and conditions can be simulated, such as different thicknesses or illumination and acquisition condition for the microscope.

Typically the expected structure of the specimen is divided in parallel slices, perpendicular to the beam, each of which will interact with the beam: this is called the multislice method. Slices are normally composed of a single atomic plane, which will scatter the electron probe. First this interaction is calculated, considering the electrostatic potential of the atoms in the first slice, then the propagation of scattered electrons is simulated. At this point, the contributions to different signals (such as HAADF) are analysed and recorded. The electron beam is now formed by scattered electrons and the original probe, which will both propagate and interact with the following slice in the simulation. The additional contribution to relevant signals will be recorded and the previous steps will be repeated for all remaining slices. The sum of all contributions represents the response of the simulated structure to the investigation.

The mathematical formulation of such algorithm is the following

$$\Psi_{n+1}(k) = [\Psi_n(k) P_{n+1}(k)] \otimes Q_{n+1}(k) \quad (3.10)$$

where $\Psi_n(k)$ is the wavefunction of the electron wave in reciprocal space, in the

n slice. $P_n(k)$ represents the propagation of the wave in free space, convolution with $Q_n(k)$ accounts for the specimen interaction with the beam, also called phase grating [69]. This is calculated for all n slices which represent the simulated specimen, which typically results in beam spreading across the sample and increasing number of interactions (see fig. 3.13), even though channelling effect can reduce this effect.

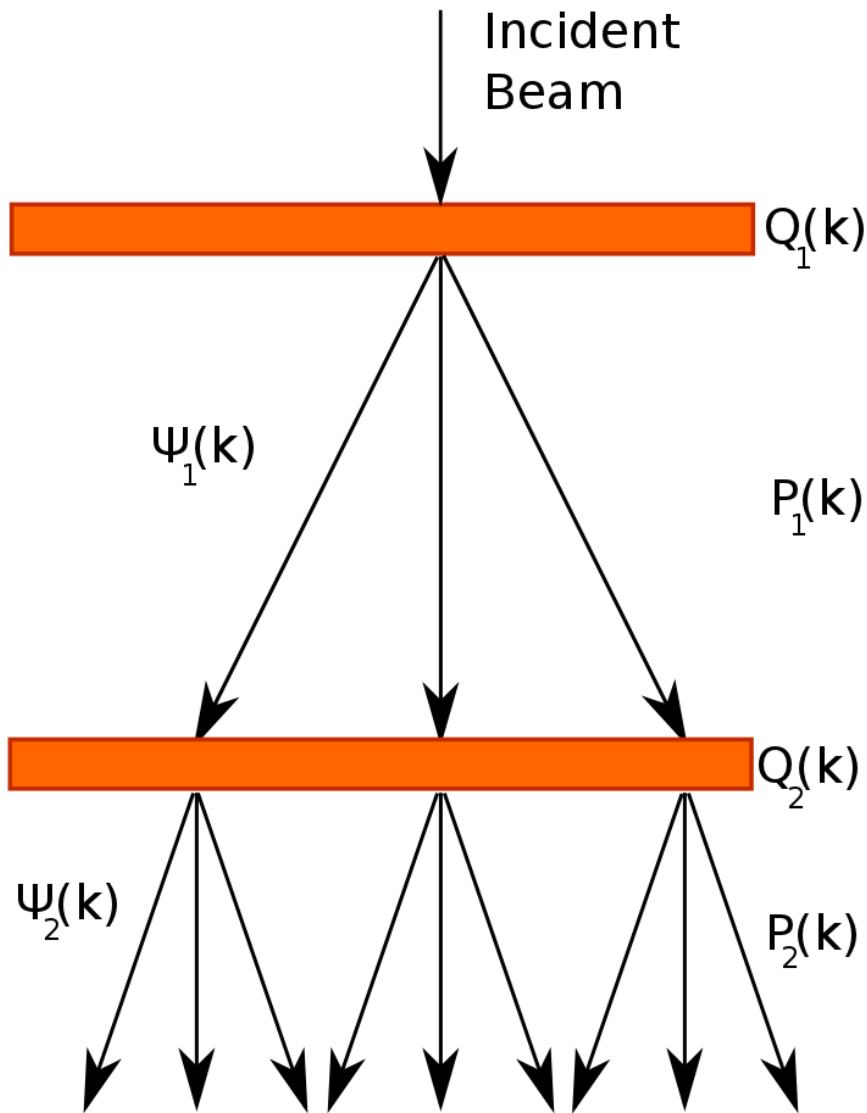


Figure 3.13: First stages of image simulations. Initial electron beam (top black arrow) interacts with first slice, modelled by convolution with $Q_1(k)$, and propagates as described by $P_1(k)$. This results in a new wavefunction $\Psi_1(k)$ which undergoes the same steps with $Q_2(k)$ and $P_2(k)$. The same procedure applies iteratively for all following slices.

A thicker slice, which includes more atom layers, would result in more wavefunctions to come into play. This happens because a bigger real space structure corresponds to

smaller k in reciprocal space, so a greater number of wavevectors and wavefunctions will fall within the aperture range.

Scattering excites different waves and the sum of all these contribution describes the electron propagation through the specimen. Finally, a convolution of such results with source profile is necessary to match the acquired data [140].

A corresponding formulation in real space is available, so knowledge of electron wave propagation P can be directly employed.

$$\Psi_{n+1}(r) = [\Psi_n(r) \otimes P_{n+1}(r)] Q_{n+1}(r) \quad (3.11)$$

The experimental results are affected by blurring because of phonon interaction with the electrons, so this effect needs to be implemented to obtain comparable simulated images. The origin of the blurring is the interaction of electrons with the atomic lattice: this can lead to absorption or creation of phonons. As mentioned in sec. 2.4.2.1, phonons have little energy (less than 0.1 eV) but considerable momentum, so they can scatter electrons by 5-15 mrad [69]. This causes blurring because the trajectories of electrons have deviated and they tend to spread across a wider area of the detectors.

This effect can be included in the simulation in two ways: by modification of the Debye-Waller factor (DWF) or, alternatively, using the frozen phonon approach. The DFW method consists in a convolution of the atomic potential with a Gaussian function, which approximates the thermal oscillations of the atoms and their potential. However, this solution does not describe incoherent scattering properly, which is the origin of HAADF image formation. On the other hand, the frozen phonon approach is well suited for HAADF simulations [123, 141]: it is based on the average of many similar lattices, all slightly displaced from each other. The approximation is justified by considering the velocities of electrons and atomic sites: the incoming electrons have near relativistic velocity, which is much higher than that of the lattice vibrations, so electrons effectively interacts with a series of static lattice configurations. This reflects the changes of atomic position due to the phonons, but it does not alter significantly the atomic potential, so inelastic scattering is well represented in HAADF simulations.

The crystallographic structure of the specimen can lead to the calculation of the most relevant phonons, so accurate displacements can be used in the simulation. About 80 frozen configurations are used to simulate HAADF images [142].

Chapter 4

Atomic Structure and Chemistry of



4.1 Introduction

The invention of microwave resonator [55] has introduced a device which can effectively handle telecommunication frequencies with extreme precision. It can act as filter, i.e. it isolates the specific frequency required by transmission and reception of signals, so it is an essential part of every telecommunication device. While filters of other kind existed before, the resonator can be scaled to portable size, such as a component of a mobile phone, and proved to be an essential factor in the miniaturisation of such applications (see paragraph 4.2.3). The size reduction is closely related to high permittivity of the material, but limited power loss at microwave frequencies is essential as well because it allows high selectivity: the ability to amplify a frequency with extreme precision, while filtering out all the other ones. These requirements are essential for the components and applications, but only few compounds, mostly ceramics, are suitable: these are called microwave dielectrics. Both permittivity and frequency selectivity are related to atomic structure and chemistry of these ceramics: the study of permittivity and polarisation is based on accurate comprehension of the crystalline structure of these materials; the power loss at microwave frequencies was related to various kind of crystalline ordering and chemical properties, such as impurities, so local composition of $Ba_{6-3x}Nd_{8+2x}Ti_{18}O_{54}$ was investigated as well.

In this chapter we first report a literature review (in the next section) with detailed description of the property of MW dielectrics, of course with special attention to barium neodymium titanate. First we present the physics related to this material (see paragraph 4.2.1) and a comparison with similar ceramics (see paragraph 4.2.2). As mentioned before, a paragraph is dedicated to applications (see 4.2.3), followed by the available information about $Ba_{6-3x}Nd_{8+2x}Ti_{18}O_{54}$ crystallography (see paragraph 4.2.4), which we are going to integrate with our results. We report here the analyses of both unit cell and composition, in order to provide a comprehensive model of the material while changing parameters such as composition and annealing temperature

(see section 4.3). Finally, our conclusions and possible follow-ups of this research are presented in section 4.4.

4.2 Literature Review

4.2.1 Physics of Microwave Dielectric

All relevant parameters of MW dielectrics (see par. 1.3.2) were related to crystalline structure and composition, so microscopy investigation has become a primary technique to investigate ceramics, providing structural and chemical data.

Freer and Azough [59] summarise the connections between different features of the material and the effect on suitable physical quantities. First, grains are considered, since higher density and substitution of cations can improve permittivity. Both can be altered by changing grain compositions with a mix of ceramic powders, in order to modify relevant properties. Empirical rules are available to predict permittivity and its temperature dependence in compounds: the Liechteneker rule describes how mixing changes permittivity

$$\log \varepsilon_f = (1 - x) \log \varepsilon_1 + x \log \varepsilon_2 \quad (4.1)$$

where x is the relative composition, ε_1 and ε_2 are the permittivity of the materials to be mixed, while ε_f is that of the final compound. An equivalent relation was found for the temperature dependence of permittivity

$$\tau_{\varepsilon f} = (1 - x) \tau_{\varepsilon 1} + x \tau_{\varepsilon 2} \quad (4.2)$$

An example of ceramic powders mixture is $AgNbO_3 - AgTaO_3$ (ATN): the two component exhibit strong and opposite temperature dependencies, but a suitable composition of powders balances them [179].

Grain boundaries are also relevant, as many impurities concentrate there. A common solution is to increase the purity of the material, but this is frequently expensive. An alternative is the introduction of additional species to trap undesired species in boundaries instead of grains, where they would lower Q : this was proved in case of $(Zr, Sn)TiO_4$ (ZTS), where NiO compensated Fe_2O_3 degradation of quality factor from diffusion of Fe^{3+} ions [180]. Microstructures and domains within grains play a role too, since higher Q is normally associated to bigger, uniform grains. Also, reduction of domains is strongly believed to improve frequency response [59].

Finally, lattice structure is important as well and, similarly to grains size case, the increase of domain size improves Q . This reflects better ordering in the crystal and can

be achieved by slower annealing and sintering [181, 182, 183], so nowadays processing grants that most grains are entirely composed of single domains [59]. The increase of cation-ordering in $Zr_{0.8}Sn_{0.2}TiO_4$ proved beneficial for Q too [184].

A closer look at perovskite ceramics emphasised the importance of BO_6 octahedral ordering in the ABO_3 perovskite. The tilting of such sub-units may be both in phase or antiphase [185] and it influences the value of τ_f [186]. It was described in terms of tolerance factor t

$$t = \frac{R_A + R_O}{\sqrt{2}(R_B + R_O)} \quad (4.3)$$

where R_A, R_B and R_O are the radii of A, B and O ions in perovskite structures. A low value of t denotes distortion in the structure related to octahedra, which will appear as a phase transition during cooling.

t controls the temperature at which the tilt begins, which in turn changes the resonating frequency as characterised by τ_f : the smallest value of τ_f was found for antiphase tilting, at $t \approx 0.97$ [187].

4.2.2 Advantages and Disadvantages of Possible Compounds

While temperature stability is paramount for every application, a distinction arises between mobile phone and network base station devices: the first requires high permittivity, to favour miniaturisation, while the second focuses on higher selectivity to avoid cross-talk between different frequencies (and networks)[58]. An empirical relation was found between the two quantities when looking at a series of MW ceramics: $\log_{10}(Q \times f_0) \propto 1/\varepsilon_r$ [188], which means that a given material can only have high values of either Q or ε_r (see tab.4.1 for examples). This effectively divides them into two classes, where one group is more suitable for mobile phone and portable devices while the other is better for base stations.

Material	ε_r	$Q \times f_0$	Structure
$BaMg_{1/3}Ta_{2/3}O_3$	24	250 000	Complex Perovskite
$BaZn_{1/3}Ta_{2/3}O_3$	29	150,000	Complex Perovskite
$Ba(Co,Zn)_{1/3}Nb_{2/3}O_3$	34	90,000	Complex Perovskite
$SrTiO_3 - LaAlO_3$	39	60,000	Simple Perovskite
$CaTiO_3 - NdAlO_3$	45	48,000	Simple Perovskite
$ZrTiO_4 - ZnNb_2O_6$	44	48,000	α - PbO_2
$Ba_4Nd_{9.333}Ti_{18}O_{54}$	80	10,000	Complex Perovskite / Tungsten Bronze

Table 4.1: List of some of the available MW ceramics, together with their value of $Q \times f_0$, permittivity and crystal structure [58].

4.2.2.1 Relevance of $Ba_{6-3x}Nd_{8+2x}Ti_{18}O_{54}$

The Barium Neodymium Titanate $Ba_{6-3x}Nd_{8+2x}Ti_{18}O_{54}$ presents one of the highest value of permittivity, which ranges between 80 and 110 depending on composition, near zero temperature dependence τ_f and reasonable $Q \times f_0$ of about 10,000 [58, 59, 61, 189, 190]. This set of properties makes it a candidate for resonators in miniaturised devices, such as mobile phones.

A complex tungsten bronze structure combining perovskite-like and non-perovskite structural units is behind these characteristic and it is then common in many MW dielectrics, because the cations have the possibility to adjust their position as a response to an external electric field, inside a relatively wide octahedra frame composed by titanium and oxygen. A rough idea of the flexibility of cations position can be provided by the perovskite structure in fig. 1.3, where cations and the octahedras are clearly visible. A similar arrangement is found in the perovskite-like structure of our samples, shown in fig. 2.19 and later in fig. 4.6: in these two pictures the bright cations can be distinguished from the dimmer *Ti* sites to show the distances and the relatively loose packing of the structure.

This flexibility allows to balance the polarisation, which influences permittivity, and the structure deformation from temperature. The relevance of polarisation, α , on permittivity, ϵ_r , is described by Classius-Mossotti (CM) equations

$$\frac{\epsilon_r - 1}{\epsilon_r + 2} = \frac{4\pi}{3} \sum_j N_j \alpha_j \quad (4.4)$$

where N_j is the concentration of a given element and j refers to the various atoms in the crystal.

Thermal energy, on the other hand, tends to soften the structure and crystal sites may shift slightly. A careful choice of composition can produce a material which balances the deformations induced by polarisation and temperature. A suitable structure may provide a permanent ferroelectric polarisation, in a practical range of temperature at least, while the polarisation still grants high values of permittivity. This optimisation is limited by phase transitions, which may introduce ferroelectric behaviour: that is characterised by spontaneous polarisation, which interferes with the desired properties.

4.2.3 Applications

The main applications of MW ceramics are resonators for base station, where they precisely select the working frequency. However, MW ceramics are widely used in a range of telecommunication components and devices, such as filters, wave guides and antennas, for which miniaturisation, temperature stability and high selectivity are important.

The wave guides for millimetre wavelengths also have a ceramic component because metals exhibit high conductive loss while dielectrics can confine electromagnetic field. Dielectric filters are used in radar and satellites too. Dielectric miniature antennas are another possible device [191].

MW ceramics can also be used for substrates of planar circuits called multilayer circuit modules (MCM)[192] for telephone applications [193, 194, 195].

4.2.4 Crystallography

Structures similar to $Ba_{6-3x}Nd_{8+2x}Ti_{18}O_{54}$ were investigated long ago in form of ternary system $BaO - Nd_2O_3 - TiO_2$ [196] as a variation of TiO_2 , which was the material of choice in early stages of research of MW ceramics. Then Kolar *et al.* [197, 198] discovered useful properties, in terms of permittivity, selectivity and temperature dependence, of similar compounds $BaNd_2Ti_5O_{14}$ and $BaNd_2Ti_3O_{10}$ (which correspond to similar mixtures of original components, respectively in 1:1:5 and 1:1:3 ratio). An intermediate composition $BaLnTi_4O_{12}$ was then discovered ($Ln = La$ or Gd), with 1:1:4 ratio, [199, 200] and chemically prepared [201, 202]. Its composition was quite debated [203, 204, 205] until a unifying interpretation included all variations in the general formula $Ba_{6-3x}Nd_{8+2x}Ti_{18}O_{54}$ [206]. The range of composition $0 < x < 0.7$ was verified, while another phase was found for $x > 0.8$ [207].

The crystal structure of $Ba_{6-3x}Nd_{8+2x}Ti_{18}O_{54}$ was first identified as orthorhombic in $Ba_{3.75}Pr_{9.5}Ti_{18}O_{54}$, which corresponds to $x = 0.75$ [208]. Space groups for $Ln = La$ or Gd (powder ratio 1:1:4) were reported as $Pna2_1$ and $Pnma$ respectively [209], corresponding to the different site symmetries reported in tab. 4.2.

Space Group	Site Symmetry Operations
Pnma	(1) x, z (2) $-x + 1/2, z + 1/2$ (3) $-x, -z$ (4) $x + 1/2, -z + 1/2$
Pna2 ₁	(1) x, z (2) $-x + 1/2, z + 1/2$ (3) $-x, z + 1/2$ (4) $x + 1/2, z$

Table 4.2: Site symmetry operations with respect to [010] direction, for Pnma and Pna2₁ space groups [210].

The unit cell of $Ba_{6-3x}Sm_{8+2x}Ti_{18}O_{54}$ ($x=0.27$) was investigated by Rawn *et al.* [211] using X-ray diffraction. They used a Pnma crystal structure for the refinement: the lattice constants were reported to be $a=22.289(1)$ Å, $b=7.642(1)$ Å and $c =12.133(1)$ Å. They suggested a structure with TiO_6 octahedra sharing vertices beside cations columns, which would be aligned along c-axis. The cations sites would be either entirely occupied by Ba , while others have mixed presence: 100% Sm [1] and 86.25% Sm [5], while another column is composed by both Ba and Sm , namely 59.25% Ba [3] and 40.75% Sm [2]). The proposed final composition is $Ba_{10.38}Sm_{17.08}Ti_{36}O_{108}$ with superstructure reflection along the b axis.

The range of composition $0 < x < 0.7$ were studied by Okudera *et al.*[212]. Their results correspond to a Pbam structure, where 5 independent columns (R sites) are in a rhomboid area, delimited by octahedra, while Ba atoms sit in pentagonal ones (P sites). These configuration is shown in fig. 4.1. Contrary to Rawn [211], the R_2 sites (labelled as $Nd[2]$ in fig.4.1) were reported to have only a minor Ba presence, with just a 13% component beside 82% of Nd atoms. Also the R_5 sites differ from Rawn, with 12% of Ba and 72% of Nd [212].

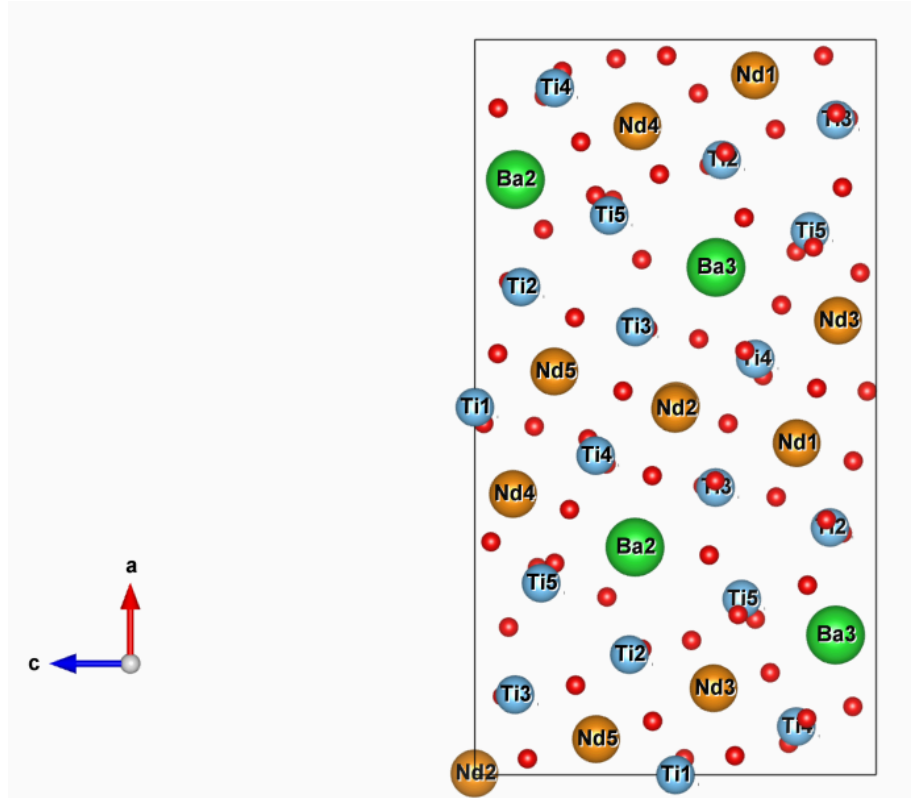


Figure 4.1: Reconstruction of $Ba_{4.5}Nd_9Ti_{18}O_{54}$ unit cell as seen from $[010]$ b-axis. Nd , Ba and Ti sites are labelled with corresponding numbers, while oxygen sites are shown as red spheres. Barium atoms are surrounded by five titanium atoms in a roughly pentagonal shape, while Neodymium by four.

Finally, Tang *et al.*[66] analysed $Ba_{4.5}Nd_9Ti_{18}O_{54}$ with X-ray powder diffraction and Rietveld refinement from 10 to 295K: they found an orthorhombic unit cell with $Pnma$ space group, with configuration equal to a tungsten bronze one and a superstructure which doubles b axis. The lattice constants are $a=22.3479(3)$ Å, $b=7.6955(1)$ Å and $c=12.2021(2)$ Å. The Ba pentagonal sites were again reported to be fully occupied, the occupancy of rhombic sites R_2 and R_5 is mostly due to Nd : it fills 79.3% of R_2 site, with a 12.5% of Ba , and 70.8% in R_5 , where Ba is limited to 12.3%. This mostly agrees with Okudera *et al.* [212], unlike the conclusions of Rawn *et al.* [211]. However, they all report some vacancies in R_2 and R_5 .

Regarding the temperature dependence, the unit cell did not change significantly from 10 to 295K [66], as expected from a material with low τ_f , since a structural change would likely modify dielectric response of the ceramic.

Based on previously mentioned findings, a tungsten bronze structure was used for refinements in this work. It is composed of TiO_6 octahedra with common vertices and columns of atoms along c-axis: two of these are independent sites, A1(1) and A1(2), are found between five titanium atoms; remaining five columns, A2(1)-A2(5), are perovskite sites. The latter are mostly occupied by Nd and will be referred to as $Nd[1-5]$, while the Ba is situated in “pentagonal” A1 sites, marked as $Ba[1]$ or $Ba[2]$ in fig. 4.1. However, a small varying concentration of Barium was found in the Nd sites too: precise measurements and compositions are reported in next section.

4.3 Structural and Chemical Model of Barium Neodymium Titanate

Samples of ceramic $Ba_{6-3x}Nd_{8+2x}Ti_{18}O_{54}$ were prepared by the team of Prof. Freer and Prof. Azough in the University of Manchester, using mixed oxide route. The process employed high purity (which means 99.5% or more) powders, namely $BaCO_3$ (Solvay, 99.5% purity), Nd_2O_3 (AMR Limited, 99.9%) and TiO_2 (Tioxide, 99.9%). The neodymium oxide was dried at 900 °C for 6 hours before the use. The powders were weighed and wet milled for 24 hours in a vibratory mill using zirconia balls and propan-2-ol. The mixture was then dried and calcined at 1150 °C for 4 hours. Wet milling was then applied a second time for 24 hours. Processed powders were then uniaxially compacted to form cylinder shapes of 20mm diameter by 15mm thickness at a pressure of 50MPa before sintering at 1350-1400 °C for 4 hours in air. The cooling rates were 180 °C/hr for all compositions, moreover $x = 0$ composition was also prepared at lower cooling rates of 6 °C/hr and 1 °C/hr.

Samples for TEM and STEM investigation were prepared by both ion beam thinning and crushing techniques, as both proved effective in the preparation of specimens. For ion beam-thinning, specimens were first ground on 1200 grade SiC to reduce the thickness of about 300 μm . They were ultrasonically cut into 3 mm diameter disks (Model KT150; Kerry Ultrasonic Ltd.) then dimpled (Model D500; VCR Group, San Francisco, CA) to reduce the thickness of the centre of the disk to 30 μm . Finally, the disks were ion beam thinned (using a Gatan Precision Ion Polishing System model 691; PIPSTM, Gatan Inc., Pleasanton, CA) operating at 4–6 kV. For the crushing method, the sintered disks were crushed to powder using an agate mortar and pestle. Grains of individual powders were dispersed in chloroform, dropped onto a copper grid with holy carbon film, and then dried. Structures were initially investigated at the University of Manchester using selected area electron diffraction (SAED) and high-resolution transmission electron microscopy (HRTEM) techniques using a FEI FEGTEM (Tecnai

G2, Eindhoven, NL for FEI Europe) operating at 300 kV. Subsequently, STEM microscopy and EELS spectroscopy were performed at the SuperSTEM facility using the aberration-corrected Nion UltraSTEM (Nion Inc., Kirkland, WA) instrument equipped with a Gatan Enfina spectrometer (Gatan Inc., Pleasanton, CA) and working at 100kV. For both imaging and spectroscopy, a probe convergence angle (α) of 30 mrad was used, generating an approximately 0.9Å wide electron probe. High angle annular dark field (HAADF) imaging was performed using an annular detector with an inner angle of 100 mrad and an effective outer angle of 185 mrad. Electron energy loss spectra were collected using an acceptance angle (β) into the spectrometer entrance aperture of 31 mrad. The specimen alignment was achieved by changing the inclination with the central disc of a convergent beam diffraction (CBED) pattern as a reference.

4.3.1 Atomic Structure Refinement from Atomic Resolution STEM images

4.3.1.1 Cations Sites

Statistical processing of HAADF atomic resolution images, taken along the [010] axis, allowed to detect atoms position and eventually pinpoint them with picometre precision, as in previous papers from our group [213, 214, 215]. Cations sites were fitted with 2D Gaussian functions by using iMtools software [132] first and the alpha version of “Image Analysis” DM plug-in (see par. 3.3.1.1) later, when elongation of sites was measured. This provided a series of coordinates for *Ba* and *Nd* sites, but a margin of roughly 1 nm from the edge was ignored. This is a prudential approach to avoid the data affected by scan distortion, which is more severe near the edges of the images. More details about the modelling procedure and the deformation of data can be found in par. 3.3.1.1. The unit cells modelled in this chapter were calculated using the “Average approach”, as it proved to be more simple and substantially equivalent to the “cell-wise approach”. It was applied to samples of various compositions and annealing ratio: there were four different composition, with $x = 0, 0.3, 0.4$ and 0.5 (based on the $Ba_{6-3x}Nd_{8+2x}Ti_{18}O_{54}$ formula), all annealed at 60 °C/hr; two different annealing ratio, 1 and 60 °C/hr, whose composition is $x = 0$.

A better statistical analysis can be achieved by considering symmetry relations between different sites in the unit cell (see sec. 4.3), since symmetry-related sites can not change position independently. The $Ba_{6-3x}Nd_{8+2x}Ti_{18}O_{54}$ structure exhibits *Pnma* symmetries [66] (see fig. 4.2), so the equivalent Wyckoff positions were averaged. The following symmetry relations [210] were used (x and z values correspond to a and c axis respectively):

$$(1)x, z \quad (2) -x + 1/2, z + 1/2 \quad (3) -x, -z \quad (4)x + 1/2, -z + 1/2 \quad (4.5)$$

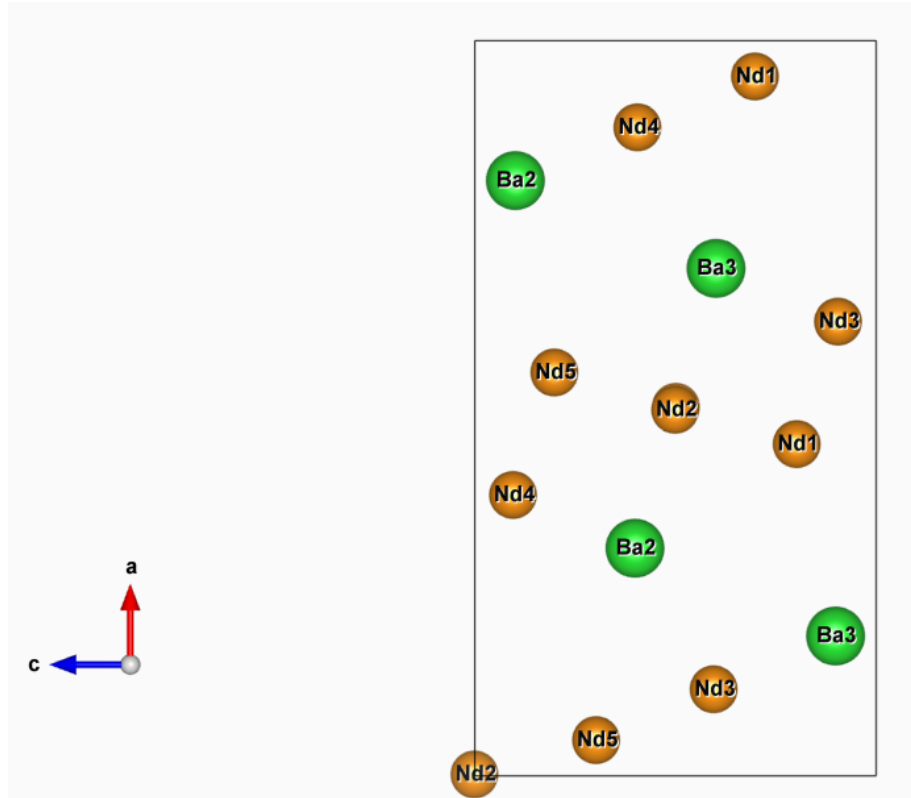


Figure 4.2: Reconstruction of $Ba_{4.5}Nd_9Ti_{18}O_{54}$ cations as seen from $[010]$ c-axis. Neodymium and Barium sites are labelled with corresponding numbers. Due to symmetry considerations, in paragraph 4.3.2 $Nd[5]$ and $Nd[4]$ sites are considered equivalent to $Nd[1]$ and $Nd[3]$ respectively.

This leads to two or four sites being linearly dependent, so they can be treated as a single site which replicates itself in 2-4 positions. As such, the set of data of different related sites can be transformed into a single one, based on symmetry operations, and averaged together. The resulting values will be then replicated, starting from the new average site. These are the final values, used for analyses and modelling, not to be confused with the first average coordinates, which were employed for the corrections.

Variations on the vertical and horizontal direction are calculated from the common set of coordinates of symmetric sites. Then, same variance is assigned to all the corresponding sites. These values derive from statistics of interpolated positions, which can increase the precision of STEM analysis [213, 214, 215], which is essentially limited by the pixel size (approximately 0.9\AA in these conditions). This procedure relies on the accuracy of initial STEM data, which show good alignment and low distortion in fig. 2.19 and 4.7, as the columns' projections appear roughly circular in the HAADF images. Considerable residual aberrations would result in irregular shapes instead, while a misalignment corresponds to a diffuse elongation of sites[78], which was not detected here. However, there is a limited amount of ellipsoidal shapes, but these are attributed to a particular feature of the crystallographic structure and are analysed in par. 4.3.1.2.

The resulting coordinates and variances for various specimens are listed below in tab. 4.3, 4.4, 4.5, 4.6 and 4.7. Variances are, as expected, smaller than the pixel size ($\sim 0.9\text{\AA}$), thank to the Gaussian interpolation procedure. All distances are relative to the centre of the cell.

Site	x [\AA]	y [\AA]	σ_x	σ_y
Nd[1]	-3.6374	1.0882	0.1888	0.2054
Nd[1]	-2.4014	-10.0226	0.1330	0.1459
Nd[2]	6.1655	11.1852	0.1643	0.2113
Nd[2]	0.0211	0.0042	0.0615	0.0974
Nd[2]	-6.0686	-11.1699	0.1591	0.2109
Nd[3]	-1.1316	8.5232	0.1001	0.1900
Nd[4]	-4.9181	-2.6680	0.1942	0.2031
Nd[4]	4.9633	2.7071	0.1461	0.2022
Nd[5]	1.2241	-8.5232	0.1442	0.2201
Nd[5]	2.5096	10.1240	0.1575	0.2177
Ba[2]	-1.1053	3.6425	0.1770	0.1736
Ba[2]	1.1996	4.2626	0.1359	0.1999
Ba[3]	4.9976	-6.8930	0.1320	0.0837
Ba[3]	-4.9519	6.8843	0.1875	0.1113

Table 4.3: Coordinates from statistical analysis of *Ba* and *Nd* cations for x=0 sample (annealing ratio 60 °C/hr).

Site	x [\AA]	y [\AA]	σ_x	σ_y
Nd[1]	-3.6873	1.0063	0.1751	0.2121
Nd[1]	-2.4252	-10.1675	0.2647	0.2713
Nd[2]	6.0773	11.1254	0.2446	0.4608
Nd[2]	-0.0065	0.0026	0.0418	0.0551
Nd[2]	-6.1223	-11.0742	0.2519	0.3158
Nd[3]	-1.2142	8.6070	0.1658	0.3834
Nd[4]	-5.0024	-2.4743	0.2256	0.2161
Nd[4]	5.0106	2.4208	0.2566	0.2876
Nd[5]	1.1435	-8.6064	0.2958	0.2338
Nd[5]	2.4101	10.2000	0.1940	0.4260
Ba[2]	-1.0620	3.6946	0.2289	0.2256
Ba[2]	1.1536	4.1798	0.1712	0.3026
Ba[3]	4.9018	-7.0579	0.3633	0.2592
Ba[3]	-5.0437	7.1344	0.2036	0.3741

Table 4.4: Coordinates from statistical analysis of *Ba* and *Nd* cations for x=0.3 sample (annealing ratio 60 °C/hr).

Site	x [Å]	y [Å]	σ_x	σ_y
Nd[1]	-3.7065	0.9360	0.1937	0.2014
Nd[1]	-2.5052	-10.1224	0.3014	0.2256
Nd[2]	6.0040	11.4163	0.4297	0.2572
Nd[2]	-0.0147	0.0135	0.0601	0.0393
Nd[2]	-6.1986	-11.2368	0.3252	0.2709
Nd[3]	-1.2279	8.5505	0.3997	0.1975
Nd[4]	-4.9318	-2.7793	0.2357	0.2422
Nd[4]	4.9068	2.7838	0.2475	0.2333
Nd[5]	1.0966	-8.4192	0.3093	0.2483
Nd[5]	2.3124	10.3021	0.4309	0.2073
Ba[2]	-0.9821	3.6535	0.1914	0.1985
Ba[2]	1.1023	4.3347	0.2871	0.1542
Ba[3]	4.9221	-6.7475	0.3096	0.2618
Ba[3]	-5.0304	6.8585	0.3692	0.2573

Table 4.5: Coordinates from statistical analysis of *Ba* and *Nd* cations for x=0.4 sample (annealing ratio 60 °C/hr).

Site	x [Å]	y [Å]	σ_x	σ_y
Nd[1]	-3.6565	1.0461	0.1617	0.1316
Nd[1]	-2.4906	-10.1032	0.1589	0.1734
Nd[2]	6.1455	11.1947	0.1825	0.1503
Nd[2]	0.0500	0.0479	0.1284	0.1150
Nd[2]	-6.0895	-11.1725	0.1416	0.1513
Nd[3]	-1.1198	8.4465	0.1659	0.1354
Nd[4]	-5.0130	-2.6719	0.1661	0.1500
Nd[4]	5.0217	2.6760	0.1395	0.0897
Nd[5]	1.0246	-8.5325	0.1204	0.1597
Nd[5]	2.5097	10.0951	0.0888	0.1639
Ba[2]	-1.0763	3.6014	0.1373	0.1113
Ba[2]	1.3115	4.2685	0.0997	0.1555
Ba[3]	4.8219	-6.9149	0.1454	0.1444
Ba[3]	-4.8804	6.9408	0.1464	0.1313

Table 4.6: Coordinates from statistical analysis of *Ba* and *Nd* cations for x=0.5 sample (annealing ratio 60 °C/hr).

Site	x [Å]	y [Å]	σ_x	σ_y
Nd[1]	-3.6374	1.0882	0.1888	0.2054
Nd[1]	-2.4014	-10.0226	0.1330	0.1459
Nd[2]	6.1655	11.1852	0.1643	0.2113
Nd[2]	0.0211	0.0042	0.0615	0.0974
Nd[2]	-6.0686	-11.1699	0.1591	0.2109
Nd[3]	-1.1316	8.5232	0.1001	0.1900
Nd[4]	-4.9181	-2.6680	0.1942	0.2031
Nd[4]	4.9633	2.7071	0.1461	0.2022
Nd[5]	1.2241	-8.5232	0.1442	0.2201
Nd[5]	2.5096	10.1240	0.1575	0.2177
Ba[2]	-1.1053	3.6425	0.1770	0.1736
Ba[2]	1.1996	4.2626	0.1359	0.1999
Ba[3]	4.9976	-6.8930	0.1320	0.0837
Ba[3]	-4.9519	6.8843	0.1875	0.1113

Table 4.7: Coordinates from statistical analysis of *Ba* and *Nd* cations for annealing ratio 1 °C/hr ($x=0$ composition).

The final unit cell was plotted for different compositions, which are summarised by the corresponding x value (from the $Ba_{6-3x}Nd_{8+2x}Ti_{18}O_{54}$ formula), see fig.4.3.

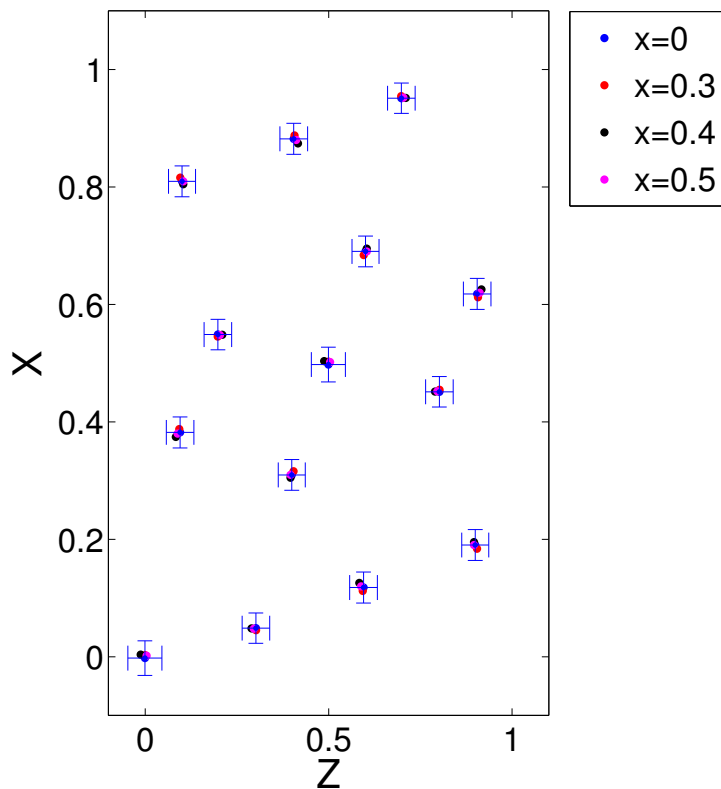


Figure 4.3: Plot of cations in the unit cell of $Ba_{6-3x}Nd_{8+2x}Ti_{18}O_{54}$ at various concentrations (represented by value x). Distances are represented as fractions of lattice constants, which is 22.3479 Å for X and 12.2021 Å for Z respectively. Error bars correspond to 3σ .

The resulting coordinates show almost no change as a consequence of different compositions. All variations are within the experimental error, so there is no noticeable effect of the composition changes on the unit cell, which appears to be stable in this range. This unit cell also agrees well with previous literature data [66] based on X-ray diffraction, so this structure is consistent when investigated by these two different techniques.

Unit cells associated to varying cooling rates after annealing are presented as well (see fig.4.4).

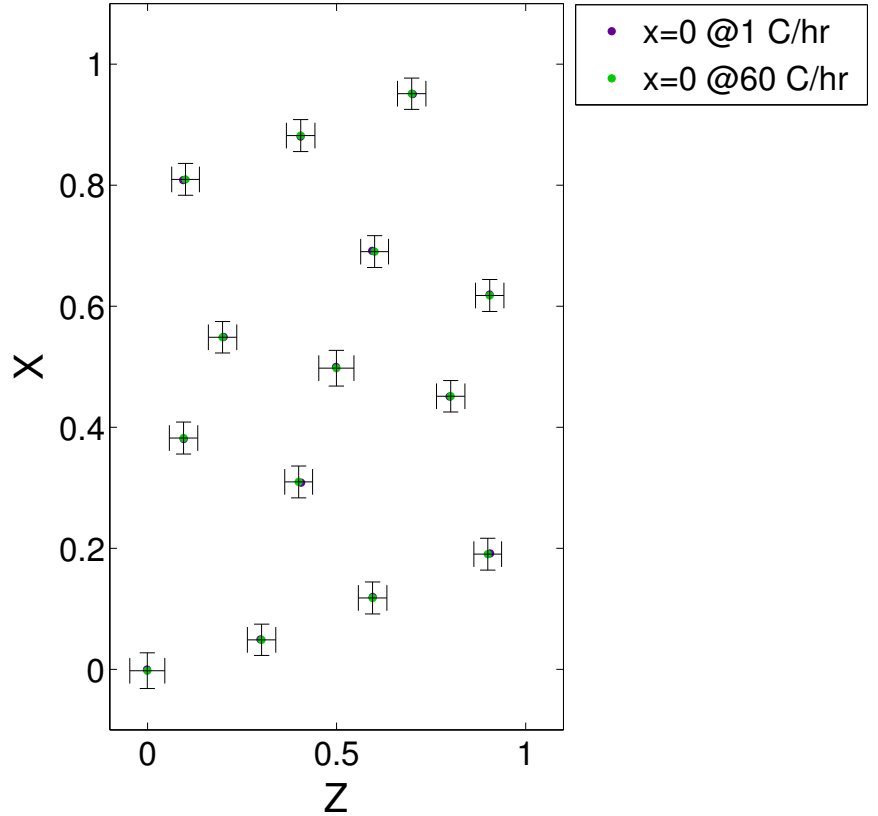


Figure 4.4: Plot of cations in the unit cell of $Ba_{6-3x}Nd_{8+2x}Ti_{18}O_{54}$ at various cooling rates. Distances are represented as fractions of lattice constants, which is 22.3479 Å for X and 12.2021 Å for Z respectively. Error bars correspond to 3σ .

The cooling rates do not affect the unit cell significantly, which was expected. However, there was a possibility of additional phase, as the slower cooling allows the material to reach an equilibrium configuration. Nonetheless the unit cell does not show any significant influence of the cooling rate and the existing changes are smaller than the experimental error. The crystal structure appears to be the same within this range of cooling rates and it remains similar to the one reported in literature [66].

These results are compared to the HAADF data in fig. 4.6, after some further analysis on the elongation of Ba and Nd [2] sites.

4.3.1.2 Elongated Sites

The unit cell of $Ba_{6-3x}Nd_{8+2x}Ti_{18}O_{54}$ was then further analysed to characterise the consistent elongation of Ba and Nd [2] sites (see fig. 3.9 and par. 3.3.1.2). The effect

was studied and the elongation was quantified in terms of angles (see fig. 4.5) and length, even though a significant variance is present.

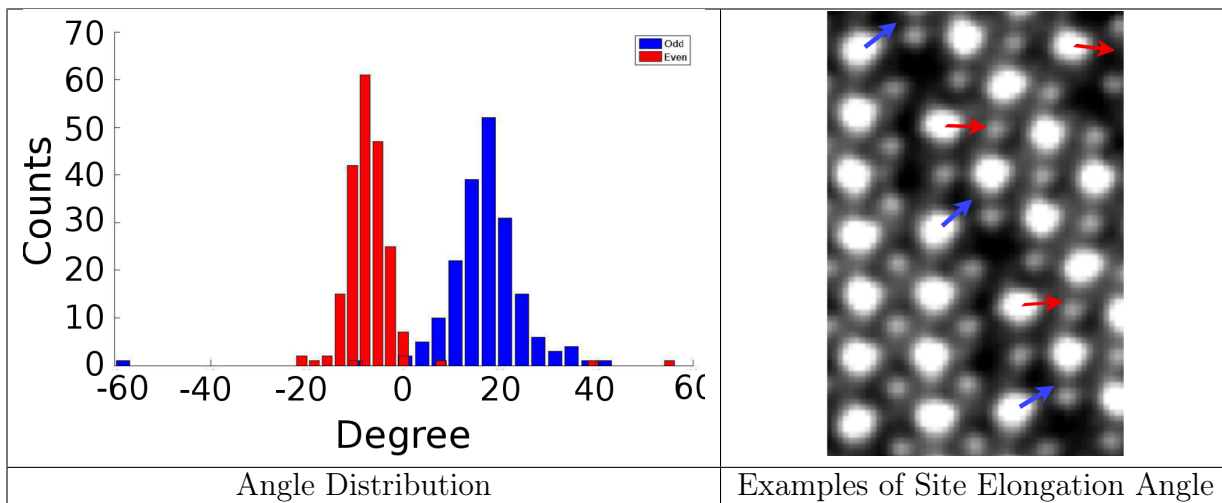


Figure 4.5: On the left, an example of distribution of tilt angles in Ba sites. Odd and even refer to different orientations of the tilt in the crystal structure, presented in the right image, which shows the angles of Ba sites. They are mostly oriented along two main directions, corresponding to blue and red arrows. $Nd[2]$ sites orientation are not considered in these figures, but they present a similar distinction (shown as black arrows in fig. 3.9).

This led to a qualitative estimation of both tilt angles and length of ellipses observed in HAADF data, which allowed to define a more detailed unit cell, based on a series of comparison and increasingly accurate refinements between the model and the real data. Thanks to a slight misalignment of atoms along $[010]$ direction, the elongation of the sites can be represented (see fig. 4.6 and corresponding table, tab. 4.8). The distortion of the HAADF data can also be noticed here, as the sites in the overlapped unit cells at the bottom and on the left seem more off-centre than those in the centre of the picture. These small differences across the HAADF image are caused by drift distortions, as the specimen moves during the acquisition and this effect can not be completely compensated. This effect is compensated in the model, because the acquired unit cells undergo a shear transformation which corrects the drift distortion.

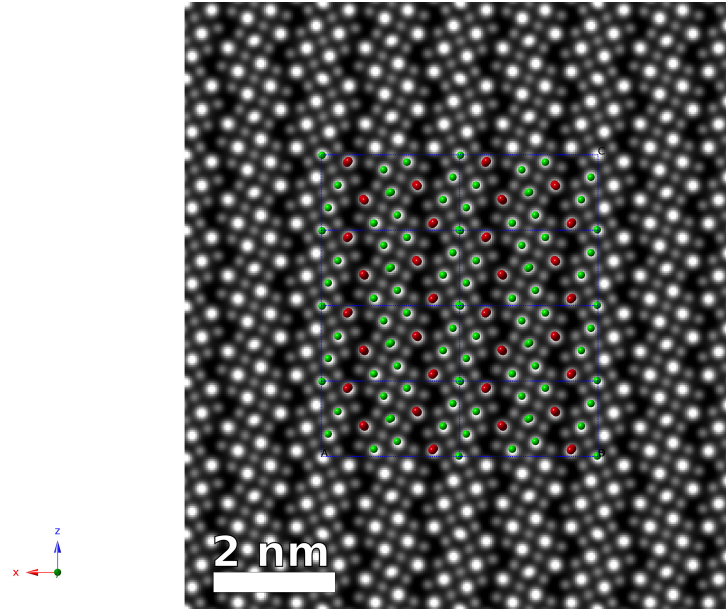


Figure 4.6: New unit cell model for $Ba_{6-3x}Nd_{8+2x}Ti_{18}O_{54}$ with tilt in Ba and $Nd[2]$ sites, overlapped over a HAADF image. Tilt is represented as misalignment of such atoms along the $[010]$ direction. A slight misalignment can be noticed in the bottom model cells because of drift distortions in the HAADF image.

Elongated Sites Model		
Site	x [Å]	y [Å]
Nd[1]	-3.6374	1.0882
Nd[1]	-2.4014	-10.0226
Nd[2]	6.1655	11.1852
Nd[2]	-0.0720	0.1207
Nd[2]	-6.1011	-11.1740
Nd[3]	-1.1316	8.5232
Nd[4]	-4.9181	-2.6680
Nd[4]	4.9633	2.7071
Nd[5]	1.2241	-8.5232
Nd[5]	2.5096	10.1240
Ba[2]	-1.2080	4.1455
Ba[2]	1.1996	4.2626
Ba[3]	5.5015	-6.7558
Ba[3]	-4.9519	6.8843

Tang's Model [66]		
Site	x [Å]	y [Å]
Nd[1]	-3.6240	1.1554
Nd[1]	-2.4770	-10.0186
Nd[2]	6.0766	11.0868
Nd[2]	-0.0244	0.0872
Nd[2]	-6.1255	-11.0868
Nd[3]	-1.1348	8.4453
Nd[4]	-4.9663	-2.7264
Nd[4]	4.9541	2.6840
Nd[5]	1.2446	-8.7457
Nd[5]	2.4282	10.1169
Ba[2]	-1.1592	4.2349
Ba[2]	1.0738	4.3847
Ba[3]	5.0273	-6.7893
Ba[3]	-4.9419	6.9390

Table 4.8: Coordinates from elongated sites model, for annealing ratio $1^\circ\text{C}/\text{hr}$ ($x = 0$ composition), and from Tang [66]. Differences in some coordinates of Ba and $Nd[2]$ sites are bigger because the Tang model did not include any elongation. However, there is a general similarity between the other coordinates. In addition, Tang's model corresponds to a different orientation of the cell, so the relative symmetry operations were applied to reach comparable coordinates. Standard deviation can not be estimated as precisely as in previous models, but comparison with Rietveld X-ray refinements and Dr. Probe simulations show good match (see fig. 4.7).

This model was used to simulate HAADF images based on our STEM settings, using the software package Dr. Probe [123] with the aid of Dr. Juri Barthel, at FZ-Jülich, Germany. Simulations were performed for different thicknesses using a wedge shaped specimen as a input, which presents increasing number of unit cells across the scanning area (see fig. 4.7). This produced a growing intensity through the image together with a perfectly defined local thickness, so it allowed us to recognise which part of the simulated specimen was most similar to our original image, determining the thickness of the actual specimen. For example, our HAADF images (such as fig. 2.19) seem to correspond approximately to a 8-9 nm thickness.

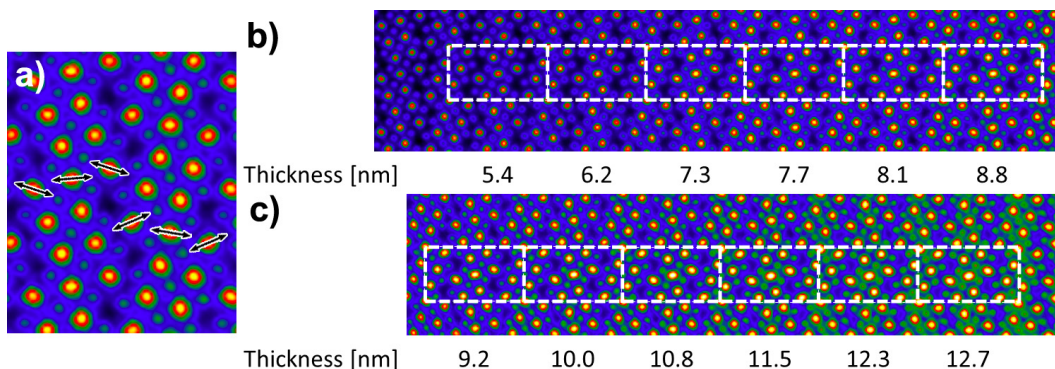


Figure 4.7: Comparison of HAADF data and simulations of our model of a unit cell. a) Real HAADF data with direction of elongation of Ba and Nd [2] sites. b) and c) HAADF data from a wedge specimen with increasing thickness: simulations of our model are overlapped in the white rectangles. This comparison can be used to estimate the thickness of the specimens.

The simulation accurately matches the real HAADF data from a wedge shaped specimen, validating the model and the accuracy of our semi-quantitative description of the elongated sites. The depiction of these features in the unit cell provides additional information on the atoms coordinates, which led to further Rietveld refinement of X-ray data. Two symmetry lowerings, consistent with deviations on the x-z plane and b direction, were identified and they can be attributed to displacement along [010] direction [134], like those we modelled.

4.3.1.3 Titanium Sites

Titanium sites were investigated to provide a more comprehensive model of the unit cell. Since the coordinates of the cations sites proved to be approximately constant in our samples, Ti coordinates were studied in just one specimen, which is believed to share the common crystal structure. The chosen sample was the one with $x = 0$ and 1°C/hr annealing ratio, because the quality of HAADF data and the number of displayed cells. The original HAADF data are shown in fig.2.19.

The data in fig. 2.19 were analysed with the Image Analysis plug-in of Digital Micrograph: in order to give an idea of the quality of the results, the coordinates resulting from the fitting process are presented in fig. 4.8. The fitting image shows the structure is conserved in most of the area, although some sites were badly fitted.

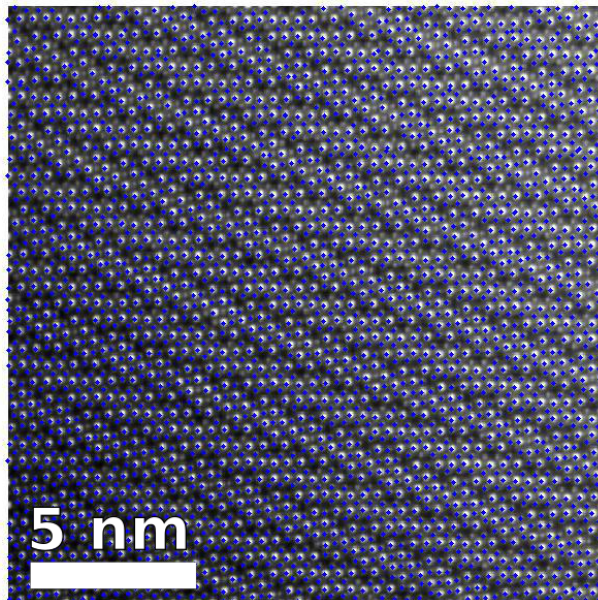


Figure 4.8: Fitting results on fig. 2.19. Some sites were not fitted correctly, but the Pnma structure is conserved.

The only difference from the $BiFe_{0.5}Mn_{0.5}O_3$ test case (shown in sec. 3.3.1.1) is that the perimeter of the cell was selected for automatic identification (for example, the red dots in fig. 4.9), instead of the whole cell. This choice reduced ambiguities in the identification of coordinates. In a latter stage, all atoms within the cell were added. This first perimeter (plotted with red dots in fig. 4.9) was chosen in an area where the fit was more accurate, since the rest of the figure 4.9 shows some “holes”, corresponding to sites which were not fitted. The central part is deemed to have the least distortion, but it is also lacking more sites: this suggested to work on another area with better data. This process led to identification of 13 cells, reported in fig. 4.9 as black squares. It proved difficult to identify more cells because of some missing points. The coordinates of the fitting process present a vertical mirroring, so fig. 4.8 and fig. 4.9 look inverted.

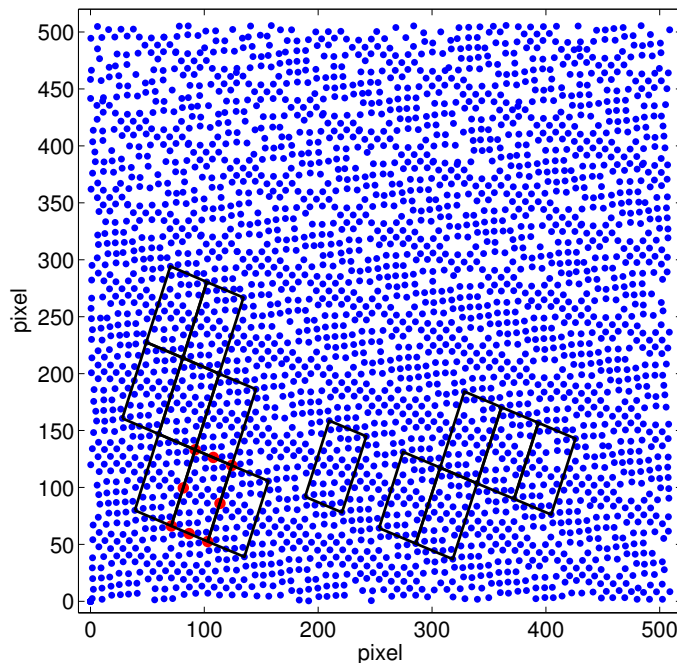


Figure 4.9: Perimeters identification from coordinates of fig. 4.8. The wide red dots correspond to the perimeter of the first unit cell, which was defined by selecting individual coordinates. The other perimeters, which are marked by black squares, were identified by a semi-automated script. It is worth noting the fitting process vertically mirrors the image, so the coordinates are inverted when compared to fig. 2.19 and 4.8.

Once the perimeters were identified, all sites within were acquired and added to the relevant cell. Few cells are missing a site, so the calculations of mean and standard deviation were based only on available data from other cells.

The following steps of the unit cell identification are exactly as those presented in sec. 3.3. The required rotation was about 0.4 rad, while the shear was roughly 10% for all data. Both “average” and “cell-wise” approaches provided similar results again, as shown in fig. 4.10.

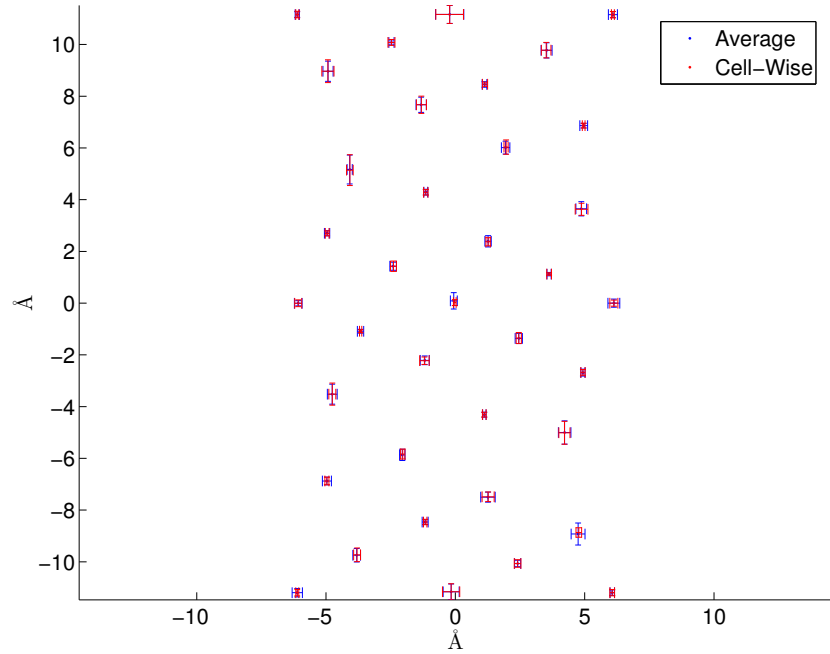


Figure 4.10: Comparison between the unit cells from the “Average” and “Cell-Wise” approaches, based on cells identified in fig. 4.9.

The Ti sites present the same symmetry of the cations, which is detailed in the formula 4.5. Similarly to what happened to the cations sites, the symmetric coordinates were grouped together to provide a better statistical analysis. The results are listed in tab. 4.9 and are close to those reported in literature [66].

Ti Site	x [Å]	y [Å]	σ_x	σ_y
Ti[1]	-0.0078	-6.0875	0.0806	0.1776
Ti[2]	-3.5822	-4.8065	0.1233	0.0838
Ti[3]	-2.2631	-1.2458	0.1281	0.0979
Ti[4]	-1.4044	2.4349	0.0794	0.1147
Ti[5]	-5.1593	4.1294	0.1690	0.0858

Table 4.9: Coordinates from statistical analysis of Ti sites for x=0 sample (1°C/hr annealing ratio).

4.3.2 Atomic-Scale Chemical Ordering

4.3.2.1 Grains Chemical Ordering

A chemical model of Barium Neodymium Titanate $Ba_{6-3x}Nd_{8+2x}Ti_{18}O_{54}$ was created, starting from the EELS-SI data provided by our collaborators at SuperSTEM facility. The elemental maps were normalised as described in chapter 3.3 and the resulting areal densities are shown in fig. 4.11.

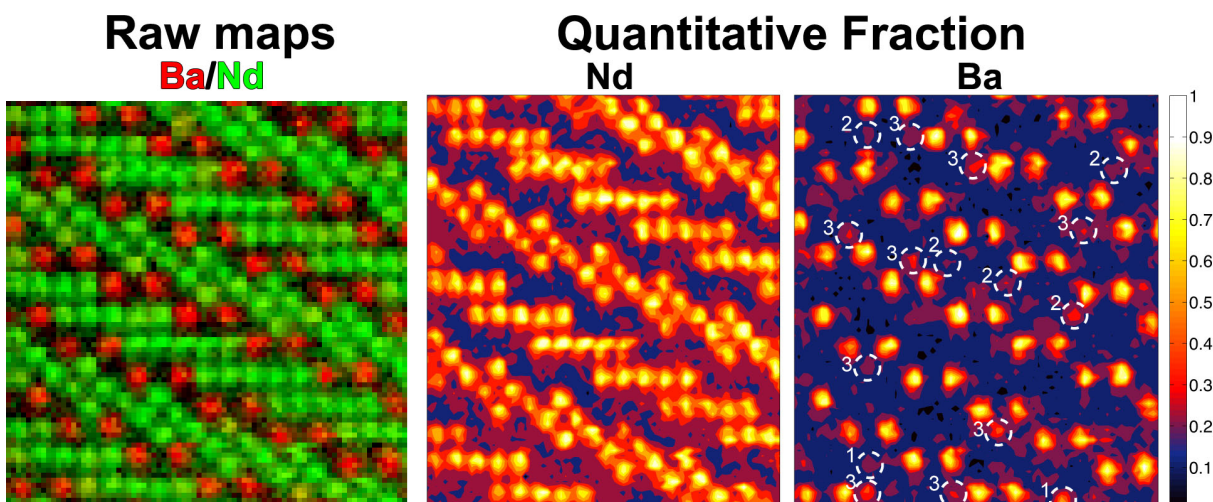


Figure 4.11: Comparison between areal densities of Ba and Nd . Raw map on the left shows few yellow sites, where both cations are present. Ba areal density is more clear and shows its presence in Nd sites, which are labelled with dashed white circles and the corresponding number of Neodymium site (mostly $Nd[2]$ and $Nd[3]$).

It is evident that the Ba signal is not limited to the expected $Ba[1]$ and $Ba[2]$ sites, but is also detected in many Nd sites (mainly $Nd[2]$ and $Nd[3]$). This feature led to a calculation of the global amount of the two cations in the material, based on our new values of elemental densities. Once substitution of Ba in Nd sites was considered (see following paragraphs for details), the new concentrations of Ba and Nd were close to those reported in literature [206] for both different compositions (see fig. 4.12) and cooling ratios (see fig. 4.13). These findings supported the correctness of our procedures and conclusion.

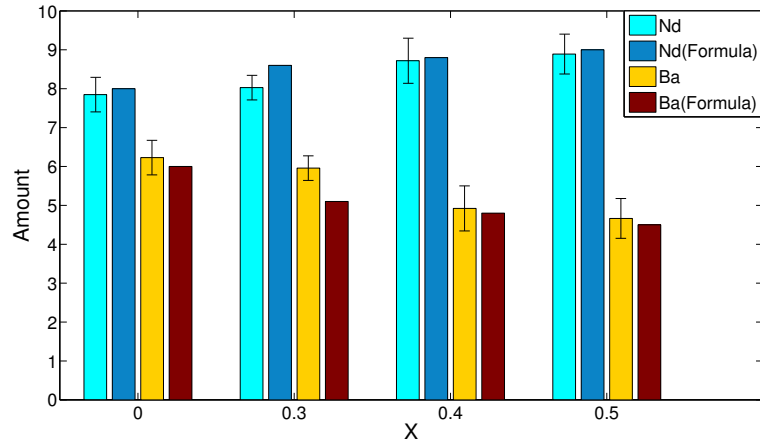


Figure 4.12: Comparison between amount of Ba and Nd in our findings and the formula from the literature [206], $Ba_{6-3x}Nd_{8+2x}Ti_{18}O_{54}$, for different x values. All samples in this plot present a cooling ratio of $60\text{ }^\circ\text{C/hr}$. Error bars correspond to 1σ .

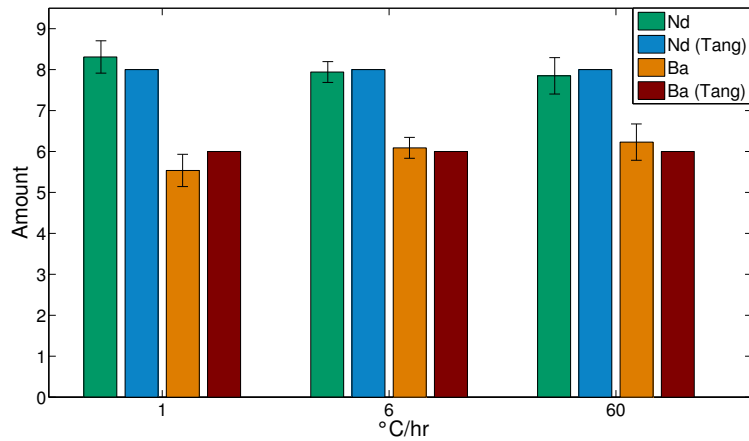


Figure 4.13: Comparison between amount of Ba and Nd in our findings and the formula from the literature [206], $Ba_6Nd_8Ti_{18}O_{54}$, for different cooling ratios. All samples correspond to $x = 0$ composition, so the corresponding formula is the same for all three specimens. Error bars correspond to 1σ .

The normalised data from EELS-SI were used to map concentration of cations in each columns, using a ratio of intensities of Ba and Nd as measured over the corresponding sites. Ba columns do not show measurable presence of Nd , while Neodymium sites proved to have a noticeable amount of Ba , which depends on stoichiometry and preparation. In fact, a systematic investigation revealed a clear trend of Ba fraction in the different Nd sites when changing composition (see fig. 4.14) or cooling ratio (see fig. 4.16).

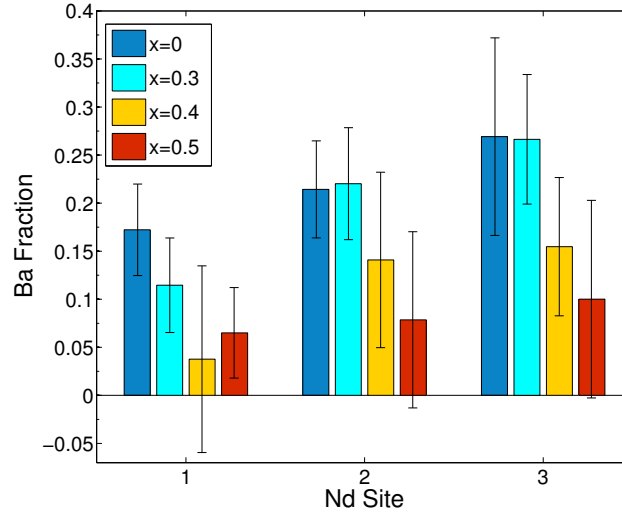


Figure 4.14: Comparison between amount of Ba in Nd sites for the various compositions (x value comes from $Ba_{6-3x}Nd_{8+2x}Ti_{18}O_{54}$). A clear trend can be seen for both x values and Nd sites. Error bars correspond to 1σ .

It is intuitive that Ba increases as its concentration in the material grows, while the differences between the Nd sites seems to correspond to the distances between such sites and the closest Ba column (see fig. 4.15): Nd [3] can be considered first neighbour of Barium sites (see fig. 4.15), so it is not surprising to detect the highest fraction of Ba in those sites. Nd [2] and Nd [1] are increasingly further apart from Ba columns, so its fraction decreases in Nd [2] sites to reach the lowest value in Nd [1] columns. All these sites are not significantly separated along z-axis (which corresponds to the [010] direction), so the distances shown in fig. 4.15 show roughly the correct proximity. Nd [5] and Nd [4] sites are considered equivalent to Nd [1] and Nd [3] respectively, because of symmetry reasons. The elongation of Nd [2] and Ba sites is not likely to be related to this result, as the Nd [3] column, which is even closer to the Ba sites and show a higher fraction of barium, does not present any elongation.

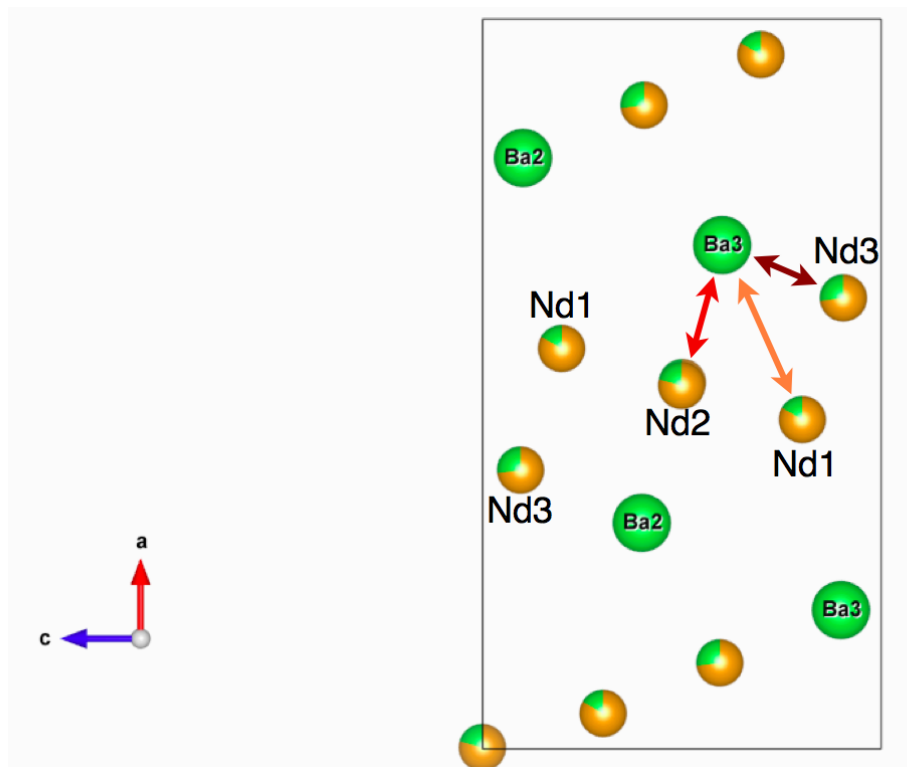


Figure 4.15: Schematic of $Ba_{4.5}Nd_9Ti_{18}O_{54}$ cations' elemental occupation, from [010] *c*-axis. *Ba* sites (shown as green spheres) are entirely composed of Barium atoms, while *Nd* ones (the orange spheres) present some *Ba* content: a corresponding fraction of the sphere is then coloured in green. The distances between *Nd* and *Ba* sites are indicated by arrows: a bigger distance corresponds to a lower *Ba* content. Due to symmetry considerations, *Nd* [5] and *Nd* [4] sites are considered equivalent to *Nd* [1] and *Nd* [3] respectively.

Additionally, the relative distances of *Nd* and *Ba* sites are approximately maintained for the different unit cells, both in case of varying composition and cooling rates, as shown in fig. 4.3 and 4.4. The 3σ error bars are presented in those images: it is possible for few *Nd* [2] atoms to be closer to *Ba* location than *Nd* [3] ones, but the probability is likely to be low for a Gaussian distribution (which is assumed in this case): a deviation of 3σ or more is found in only 0.3% of occurrences.

On the other hand, the cooling rate plot of fig.4.16 suggests that a slower temperature reduction allows cations to concentrate in their own sites, while faster cooling leaves a higher amount of *Ba* in all *Nd* sites (see fig. 4.16). This results in an increase of *Ba* concentration for faster cooling ratio, as shown in fig. 4.13 too. The distance of *Nd* sites from the *Ba* ones seems to play a role again, as the *Ba* fraction grows with the proximity between *Ba* and *Nd* sites.

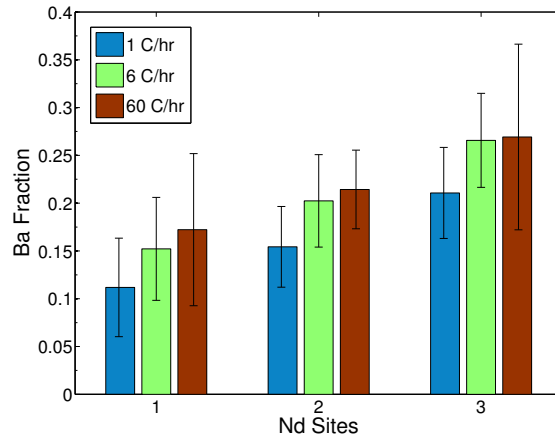


Figure 4.16: Comparison between amount of Ba in Nd sites for various cooling rates. A trend can be seen for both anneal and Nd sites. Error bars correspond to 1σ .

Site	$x=0$ 60°C/hr	$x=0.3$ 60°C/hr	$x=0.4$ 60°C/hr	$x=0.5$ 60°C/hr	$x=0$ 6°C/hr	$x=0$ 1°C/hr
Nd[1]: Nd	0.83(8)	0.89(5)	0.96(10)	0.935(47)	0.85(5)	0.89(5)
Nd[1]: Ba	0.17(8)	0.11(5)	0.04(10)	0.065(47)	0.15(5)	0.11(5)
Nd[2]: Nd	0.79(4)	0.78(6)	0.86(9)	0.921(92)	0.80(5)	0.85(4)
Nd[2]: Ba	0.21(4)	0.22(6)	0.14(9)	0.079(92)	0.20(5)	0.15(4)
Nd[3]: Nd	0.73(10)	0.73(7)	0.85(7)	0.900(100)	0.73(5)	0.79(5)
Nd[3]: Ba	0.27(10)	0.27(7)	0.15(7)	0.100(100)	0.27(5)	0.21(5)
Nd[4]: Nd	0.73(10)	0.73(7)	0.85(7)	0.900(100)	0.73(5)	0.79(5)
Nd[4]: Ba	0.27(10)	0.27(7)	0.15(7)	0.100(100)	0.27(5)	0.21(5)
Nd[5]: Nd	0.83(8)	0.89(5)	0.96(10)	0.935(47)	0.85(5)	0.89(5)
Nd[5]: Ba	0.17(8)	0.11(5)	0.04(10)	0.065(47)	0.15(5)	0.11(5)

Table 4.10: Ba fraction in Nd sites. These values are plotted in fig. 4.14 and 4.16.

Our conclusions of full occupancy in $Nd[2]$ and $Nd[5]$ sites disagree with previous literature [66, 211, 212], for example Tang *et al.* [66] reported $Nd[2]$ sites with a 91% occupation and $Nd[5]$ ones with a 82%. Moreover, Tang did not report any Ba in $Nd[3]$ sites, while we detected the highest Ba substitution ratio in those sites. Another difference was found in $Nd[2]$ sites, where our data show a Barium ratio of about 15-20% in most specimens, while Tang and Okudera [66, 212] report about a 37% Ba ratio in those columns. These details were obtained using atomic resolution spectroscopy, which provided a more complex description than X-ray diffraction studies in literature.

These results are too detailed to be entirely confirmed by Rietveld refinement of X-ray diffraction, as it can not be restricted to a limited number of sites as HAADF. However, the fits of the Rietveld refinements were constrained according to our data to improve the refinements. The related results will be submitted for publication shortly [134].

4.3.2.2 Phase Boundary Chemical Ordering

The composition of phase boundaries in $Ba_{6-3x}Nd_{8+2x}Ti_{18}O_{54}$ was investigated too because of its relevance in the dielectric properties of the material [180]. This analysis was based mostly on EELS data taken in two boundary regions of a sample with $x = 0$ and 1 °C/hr cooling rate. These areas were investigated also by HAADF, which provides a higher spatial resolution than EELS-SI and helps to understand the orientation of the two grains at the boundary, as in fig. 4.17a and b.

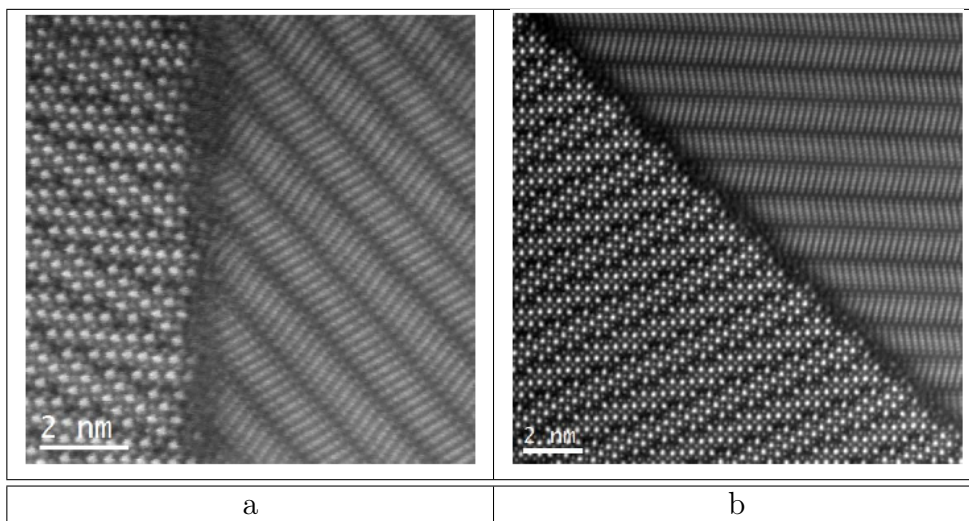


Figure 4.17: HAADF data from two phase boundaries analysed in this section. These images come from a $Ba_{6-3x}Nd_{8+2x}Ti_{18}O_{54}$ sample with $x = 0$ composition, annealed at 1 °C/hr.

The grain boundaries of $Ba_{6-3x}Nd_{8+2x}Ti_{18}O_{54}$ could differ from the grain in the structure and stoichiometry, as it was already reported in ceramic materials like ZnO [216, 217]. If this constitutes a second phase, it may influence the properties of the material. The presence of impurities in the boundaries can result in a similar effect too [180]. It is therefore important to study the stoichiometry of such regions: EELS spectroscopy provided compositional data from these regions, which can lead to identification of the stoichiometry in the boundary. EELS data can also be studied and presented in the form of spectra or elemental maps. This allows two different analyses: the spectrum of the boundary can be studied to relate it to corresponding spectra of known materials, while elemental maps can show the amount of a given element in the boundary, leading to quantitative analysis of species. The results of these two studies are now presented and compared.

EELS Spectrum Analysis The EELS spectra of both our acquisitions show some differences in the boundary, after the normalisation with the grains' spectra in the slope region between 600-700 eV, as seen in fig. 4.18.

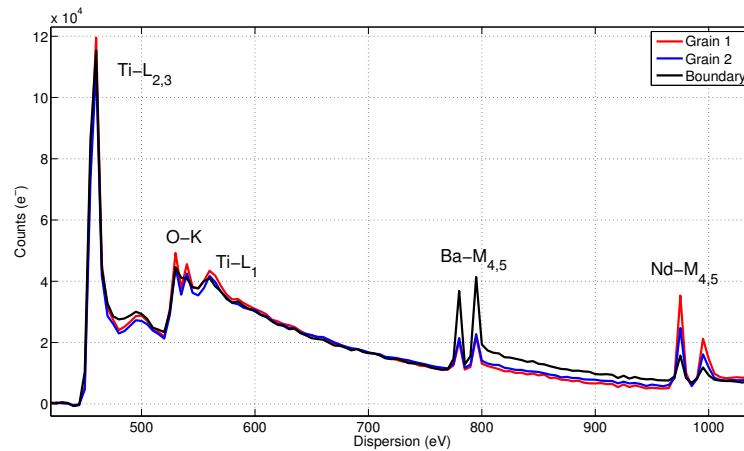


Figure 4.18: EELS spectra from phase boundary and nearby grains.

There is an increase in the Ba signal and a decrease in the Nd one, while the titanium stays constant. The information about Ba, Nd, Ti and O is shown in fig. 4.20, as EELS-SI mapping, which proves that Neodymium is depleted in the boundary, while Barium, Titanium and Oxygen are present. It is then interesting to notice a difference in the Oxygen k-edge at 530-550 eV, which differs from the grains' spectra: a lower second peak of the oxygen edge was reported in literature as a sign of oxygen vacancies in $BaTiO_3$ [218].

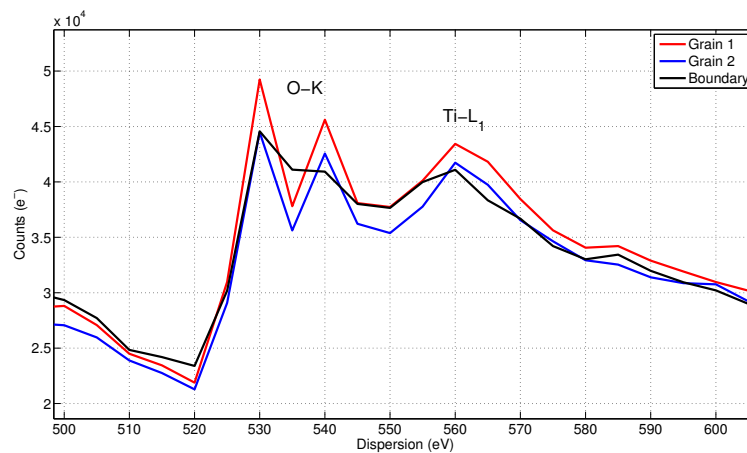


Figure 4.19: Oxygen k-edge spectra from phase boundary and nearby grains.

Unfortunately it was difficult to extract additional information from the Energy Loss Near-Edge-Structure (ELNES) because of the poor energy resolution (5 eV per channel) and the presence of the titanium peaks ($Ti - L_{2,3}$ and L_1) nearby.

Elemental Maps Analysis Elemental maps of Ba, Nd, Ti and O are shown in fig. 4.20. They underwent a PCA reconstruction to reduce the noise component and the first 9 components were accepted for the first sample (fig. 4.17a) while 7 were enough for the second (in fig. 4.17b). The percentages of the Ba and Ti were calculated over areas on the boundary and beside it for comparison. The Nd was not considered as it is mostly absent in the boundary, while the oxygen elemental mapping tends to show poor spatial resolution, so it can not be reliably analysed in the boundary zone. The ratio of Ba and Ti in the boundary was found to be similar to some barium titanium oxides.

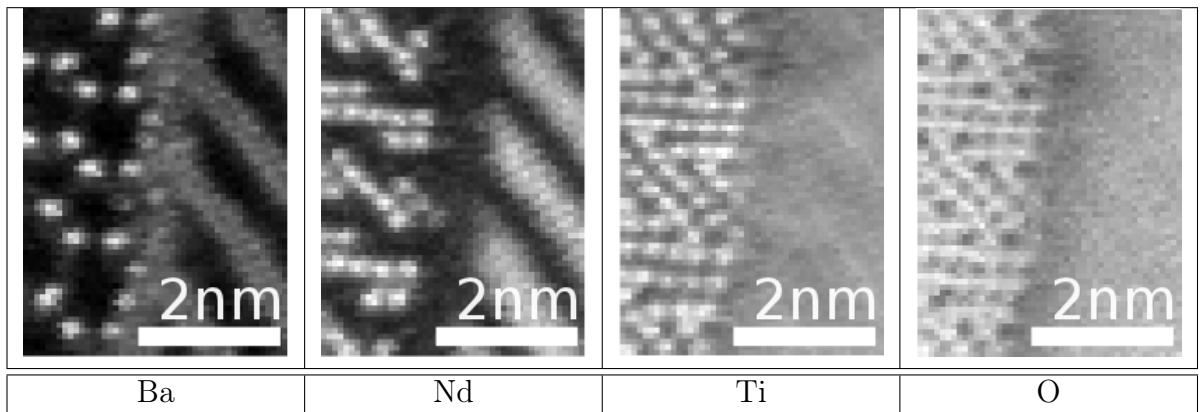


Figure 4.20: Elemental maps of Ba, Nd, Ti and O of phase boundaries in $Ba_{6-3x}Nd_{8+2x}Ti_{18}O_{54}$ sample ($x=0$, 1 °C/hr). The investigated area correspond to a part of the grain boundary shown in fig. 4.17a.

The expected ratio of Barium to Titanium in the grain is 33% (on average), as the formula predicts 6 atoms of Ba and 18 of Ti for our samples for the $x = 0$ composition. This value was approximately confirmed by the first specimen from fig. 4.17, where the grain areas were investigated and the measured values were roughly 37%. However, the second sample presents a value of about 16%, as the Ba content was lower than predicted. On the other hand, the boundaries in both samples show different values, with 44% and 14% respectively. These ratios can be normalised with respect to 33% (starting from detected values of 37% and 16%), which result in 39% and 22%. These data are reported in the following table 4.11, together with possible barium titanate compounds which present similar ratio.

Sample	A	B
Grain's Ratio	16%	33%
Boundary's Ratio	14%	44%
Possible Formula (Relative Ratio)	Matching ratio not found	$BaTi_2O_5$ (50%)
Normalised Boundary's Ratio	22%	39%
Possible Formula (Relative Ratio)	$BaTi_5O_{11}$ (20%) - $Ba_2Ti_9O_{20}$ (22%)	$Ba_6Ti_{17}O_{40}$ (35%)

Table 4.11: Ratios of Ba to Ti in the grains and boundary of the two samples. Possible formulas are suggested.

The two analyses suggest presence of some barium titanates compound at the phase boundary, but it is not clear which formula suits best our data. The consideration of O k-edge in the EELS spectrum points at oxygen vacancies, while relative percentages of Barium and Titanium seem to vary considerably between the two samples. The possibility of excessive noise in the data has to be considered, however crystallographic conditions may play a role too: the two samples in fig. 4.17a and b show a different angle between the structures of the grains beside the boundary. This could lead to diverse arrangement and chemistry in the two sections, even though the composition is the same. Another possibility is that the boundary does not allow formation of an extended barium titanate structure, given the limited extension of the boundary: our measure would then probe the intermediate structure between the grains and the boundaries, together with the expected barium titanate itself. This would alter the relative amount of elements. This is somehow supported by the Ba and Ti map in fig. 4.20, where some Ba and Ti sites can be noticed in the boundary, with a lower intensity. This could reflect a gradual change in the crystallographic structure.

4.4 Conclusions and Suggested Future Work

The unit cell of $Ba_{6-3x}Nd_{8+2x}Ti_{18}O_{54}$ was investigated for different concentrations and annealing ratios, assessing the stability of crystal structure. The unexpected elongation of the Ba and $Nd[2]$ cations sites was interpreted as a misalignment along the atom column, then it was modelled and showed close resemblance to real HAADF data. The composition was probed as well, detecting clear patterns of Ba distribution with preferential substitution onto $Nd[3]$ sites, less onto $Nd[2]$ sites and very little onto $Nd[1]$ sites. This is in marked contrast to the substitution patterns assumed in

previous Rietveld refinements of XRD data [66, 211, 212]. It is therefore shown that use of electron microscopy to constrain the elemental partitioning to different sites in a Rietveld refinement is important in such complex oxides as studied in this work.

Structural and chemical characterisation can justify changes in relevant parameters of MW dielectrics and, even though literature on the general topic exists, an investigation on permittivity, selectivity and thermal stability for $Ba_{6-3x}Nd_{8+2x}Ti_{18}O_{54}$ would be interesting to correlate such values with our findings. For example, although unit cell does not change with different annealing, more substitutional Ba is found in Nd sites, so some effect on polarisation and permittivity may be expected.

It would be interesting to assess whether substitutional Ba atoms have a pattern or obey some periodicity, possibly related to the arrangement of the superstructures, which have already been detected along the c axis of $Ba_{6-3x}Nd_{8+2x}Ti_{18}O_{54}$ [208]. Investigation of the specimens in different crystallographic orientation would allow a complete 3D investigation of unit cell and substitutional Ba atoms.

Chapter 5

Morphology Study of Organic-Inorganic Compounds

5.1 Introduction

In this chapter morphology and phase separation of organic blends will be investigated, with special attention on the influence of quantum dots (QDs). This is especially important since they are considered a possible alternative, both cheap and easily manufactured, to semiconductor electronics, optoelectronics [149, 150, 151, 152], photovoltaics [153, 154, 155, 156] and biosensing devices [157]. However, production of such systems will require careful knowledge and modelling of blends, as parameters can change greatly final results, particularly when mixing additional components like QDs.

In this chapter we introduce the topic of organic blends for semiconductor electronics, focusing especially on morphology. A literature review is presented in the next section, dealing first with applications and relevant technological achievements (see section 5.2.1), then we move to the blend preparation conditions (see section 5.2.2), including the effect of nanoparticles.

Finally we move on the experimental part, starting with the details of various specimens (see section 5.3). The analyses, results and interpretation are then presented in section 5.4 and finally conclusions are reported at the end (see section 5.5).

BF-TEM analyses of different organic blends have been carried on to characterise layers of F8BT:TFB, because of its technological importance. Important details about morphology, interfaces and interaction of the components in the blend were described and interpreted in terms of interaction between organic and inorganic materials in the blend, with a focus on practical applications. STEM analysis was also performed on QDs samples to further characterise the behaviour of the nanoparticles in the sample.

The study was performed on different compositions, both with and without QDs. Results were compared with parallel surface AFM analyses, carried on by our collaborator, Dr. Michail Kalloudis, from University of Edinburgh, working within the group of Dr. Vasileios Koutsos and Dr. Paul Clegg. Dr. Kalloudis also prepared the samples used in this chapter.

5.2 Literature Review

5.2.1 Reasons of Interest and Applications

The huge technological importance of semiconductor materials, together with the complex requirements of processing the inorganic semiconductors, led to consideration of cheaper alternatives, like organic ones. These allow much easier processing, both in terms of required time, temperature and facilities. Also, they provide a greater flexibility thanks to chemistry of composite materials, which allows combination of properties from different substances. For example conjugated polymers (which are conductive thanks to delocalised electrons along π -conjugated polymer chains) have been mixed with inorganic nanoparticles (such as quantum dots) in thin films to fabricate light emitting diode (LED) [149, 150, 151, 152], photovoltaic cell (PC) [153, 154, 155, 156] and biosensor materials [157]. However, organic semiconductors show a reduced durability when compared to inorganic alternatives, as well as lower conductivity. These properties initially restricted their use to disposable electronics, which do not require long-lasting materials, but now organic semiconductors are employed in a wider range of products, such as LED and PC, which are meant to operate for years. The conductivity is still an issue, so any application involving considerable current, such as power electronics, is not suitable for organic semiconductors.

Most common conjugated polymers are polyfluorenes, thanks to their easy processing and good optoelectronic performances, especially when compared with other π -conjugated polymers such as the polyphenylenes (PPPs and PPVs), polythiophenes (PTs), polypyrroles (PPYs) and polyanalines (PANIs) [1]. Moreover they provide good stability when mixed with inorganic nanoparticles such as quantum dots [158]. In particular, the two polyfluorenes used in this work, F8BT, poly(9,9-dioctylfluorene-co-benzothiadiazole) and TFB, poly[9,9-dioctylfluorene-co-N-(4-butylphenyl)-diphenylamine], already proved to be effective in heterostructures for LEDs [159, 160, 161] and PCs [162]. However, the mobility of F8BT is approximately an order of magnitude lower than that of TFB [163], a common distinction between hole and electron-transporting organic materials. This difference in conductivities results in negative effect on device performance [159]. Inorganic nanoparticles however can provide a better optoelectronic efficiency and help reduce the problem [1, 149]. Unfortunately, the reliable and reproducible production of suitable mixture and thin film is still an open problem. The interfaces between the materials are crucial [1, 164] and require investigation in the nm scale, before and after the introduction of nanoparticles.

5.2.2 Physics of Conductive Organic Materials and QDs Thin Films

A blend of two semiconductor organic materials can behave as a p-n type interface of inorganic semiconductors, for example in common devices such as LEDs [7]. A suit-

able solution and spin coating are enough to create such interface, so this represents a cheaper and faster processing and production method than inorganic materials. This also provides a good degree of flexibility when compared to inorganic processing, which involves complex substrate preparation and doping processes. This difference in complexity is partly due to precise patterning in inorganic semiconductors, while organic blends are based on self-assembly, as the phases' formation and then the interfaces are governed by thermodynamic and chemical processes (e.g. nucleation and glass transition). So, the morphology and phase separation of such blends can not be directly controlled, but composition, choice of solvent and deposition parameters can influence the result, altering the interfaces and ultimately the performances of related devices [8, 159, 160]. This was interpreted in terms of excitons behaviour, energy band and photoluminescence process, which are influenced by interfaces [159].

The F8BT:TFB blend was one of the main studied blends because of its promising application in optoelectronics, such as LEDs with high brightness and efficiency [8, 165, 166] and good durability of performances [167, 168]. The behaviour of phases in F8BT:TFB thin films was studied [160] using *p*-xylene as a solvent, as it is able to promote phase formation in this blend because of difference in solubility of F8BT and TFB. The correlation of morphology with average molecular weight (M_n) was reported, as a $M_n < 10\text{ kg/mol}$ (for at least one of the components) result in limited lateral phase separation [161]. To the best of my knowledge, there are not reports of investigation for blends entirely composed of low molecular weight polymers, which arises for the main focus of this chapter. This is believed to be beneficial for high operating voltages and hole mobility in TFB [161].

A model for phase separation of F8BT:TFB in *p*-xylene was also proposed [160], which explains the formation of the two phases as a consequence of solubility. The two components segregate either by spinodal decomposition (local density fluctuations which start aggregation), in case of 1:1 ratio, or by nucleation, in case of 1:3 composition. The phases are not expected to be completely pure, according to this model: the 1:1 ratio blend results in a F8BT-rich phases, forming islands of 2-5 μm size; the 1:3 ratio sample presents phases composed mostly of TFB, with an extension of 0.5-1.0 μm , within a matrix of F8BT.

Characteristics of F8BT:TFB thin films with 1:1 weight ratio were first investigated by Moons and collaborators [159, 165, 166, 169] and later by Friend [160, 161] by means of atomic force microscopy (AFM): they present micrometer wide domains scattered across a homogeneous phase. A higher fraction of TFB results in bigger patches while an increase of F8BT reduces the domains to 200-300 nm for 2:1 w/w [159, 165, 166, 169].

The morphology of F8BT:TFB in thin film was investigated by AFM, Raman spectroscopy and XPS by Kim *et al.* [160]. Their work was carried out by dispersing the polymers in *p*-xylene and depositing on Indium Thin Oxide (ITO) substrates. The average molecular mass (M_n) of the polymer molecules was about 108.000 for F8BT, while TFB value was approximately 56.000. This study provides a phase diagram at

22 °C, for a blend with a 10-20 mg/ml concentration forming a 100 nm thick thin film, which is helpful for the preparation of spin-coating on such blend. TFB was shown to be more soluble in *p*-xylene, while F8BT is almost insoluble (solubility of about 3.5% in that solvent). It is then likely that a F8BT rich-phase will form first, soon after the start of the evaporation, then a TFB rich-phase will aggregate. Vertical segregation is to be expected as well, since TFB has lower surface energy (approximately 35-40 mJ/m^2 while F8BT's one is roughly 40-45 mJ/m^2) so it prefers interfaces with the substrate and with air, forming a layer on top of F8BT phases (see fig. 5.1). The tendency of TFB to wet substrate is also ascribed to solvent concentration gradient during evaporation. Furthermore, this segregation is compatible with the thermodynamic process behind the reduction of interface energies in a weakly interacting substrate-polymer interface. Kim *et al.* [160] also linked their model for the evolution of F8BT:TFB structures to performances of conjugated polymer based LED.

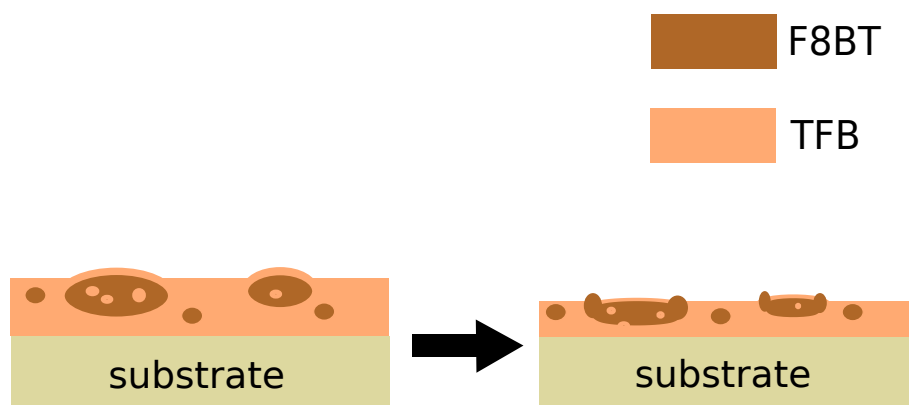


Figure 5.1: Final stages of phases evolution in F8BT:TFB thin film according to Kim *et al.* [160]. The phases are formed by either local fluctuation of density (in 1:1 ratio samples) or nucleation (when components are heavily unbalanced). Solvent evaporation promotes the glass transition, which freezes the phases configuration (schematic on the left). Then *p*-xylene continues to evaporate: in presence of air, F8BT, TFB, and *p*-xylene show a coffee stain behaviour, where the F8BT concentrates at the edges in a crater-like shape. TFB forms a capping layer on top, because its surface energy is lower than that of F8BT (schematic on the right). For the same reason, the interface with the substrate is composed by TFB.

The molecular weight's influence on vertical and horizontal phase separation of F8BT:TFB in thin-film was investigated by Yim *et al.*[161], by use of AFM, XPS and photoluminescence spectroscopy (PL). No lateral phase segregation (on a micrometer scale) was found when one of the polymers presented low average molecular weight ($M_n < 10$ kg/mol), while vertical separation was detected, as a consequence of different molecular weights. Interface with air was again linked to the low M_n polymer, on the grounds of surface energy of terminations and conformational entropy. As expected, when M_n is high for both polymers the horizontal separation is present.

There was no investigation of blend with low and similar molecular weights for both polymers, which could prove interesting as it preserve high performances of devices when driven at high voltages [161]. This was linked to the lowering of mobility in TFB when its molecular weight increases [161]. Moreover, domain size was found to decrease lowering the M_n of one of the polymers [161], so there is an expectation of smaller phases and then wider interfaces, beneficial for exciton splitting and electroluminescence (see par. 1.2.2). However, the phases segregation also depends on other factors, such as relative miscibility and viscosity [161], so the morphology in low M_n blends needs to be investigated.

5.2.3 Relevance of CdSe QDs incorporated in F8BT:TFB

Quantum dots have interesting optoelectronic properties, such as varying energy gap as a function of size, and have been successfully integrated in inorganic solar cells [52, 53] and LEDs [49]. Beside the narrow emission and absorption range of photons, QDs are also useful to promote the quantum efficiency and charge transfer to the rest of the device. This effect was verified in polymer blends mixed with QDs as well [170, 171, 172], leading to improved efficiencies in organic photovoltaic cells [173] and OLED (organic LED) [50] when nanoparticles were added to the blend. Since the low conductivity of electron-transport conjugated polymers is known to worsen the performances of related devices [159], the contribution of QD electron transfer justifies improvements of device performances [1]. A schematic of the effect of QDs on charge transfers in a OLED device is presented in fig. 5.2 as an example: the QDs attract charges because of favourable energy levels, acting as recombination centres for electrons and holes, emitting photons in the process.

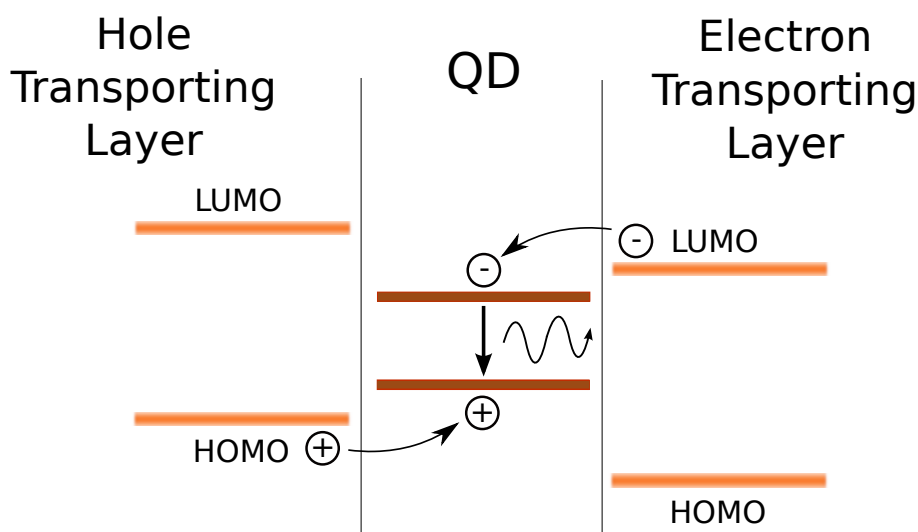


Figure 5.2: Schematic of OLED with quantum dots. These nanoparticles act as recombination centres for the charges, because of favourable energy levels, promoting photon emission [1].

It is then relevant to consider the diffusion of QDs within the blend and particularly in the F8BT phases, as it is the electron-transport material and it is meant to interact with the quantum dots for a better charge transfer. QDs are normally coated with surfactants to promote their dispersion, resulting in a colloidal behaviour in a solvent. A study on F8BT:TFB blend with PbS quantum dots reported a reduction of polymer domains' size, but this paper did not provide detail on QD distribution, which was simply assumed to be homogeneous [1]. A TEM investigation would then be useful to investigate the dispersion of QDs, as nm resolution is needed to locate nanoparticles.

Phase separation in polymer blend-nanoparticle mixtures has not previously been investigated in detail. F8BT:TFB blend with lead-sulfide (PbS) colloidal quantum dots was studied with respect to structural morphology influence on operating optoelectronic devices[1]. The best production procedure was blending colloidal QDs with the polymer mixture and then proceed with the spin-coating of the active layer on a substrate. Uniform dispersion of QDs in the blend was assumed. Confocal fluorescence analysis showed that F8BT:TFB thin films have smaller domains when QDs are added, even though the volume fractions were not reported [1] and this technique does not allow the detection of nanoparticles, so direct location and investigation of QDs is not possible. However, the introduction of nanoparticles proved to affect the phase separation and morphology. This was first investigated by optical microscopy in mixture of styrene and ϵ -caprolactone oligomers: the mobility of monodispersed glass particles was linked to the coarsening of the blend [174]. A simulated dynamics of nanoparticles with preferential wettability in a phase-separated binary blend, suggested their influence on morphology and velocity of phase evolution [175]. A volume fraction as small as 3% still proved to be influential for the morphology. Slow phase growth was linked to the "pinning effect", where the higher affinity of one phase with the nanoparticles leads to intermixing and an increase of viscosity in that domain. The interaction is influenced by density and mobility of particles, and wettability of the blend's constituents. This was verified by TEM in study of PMMA-SAN blend with silica nanoparticles [176] and by AFM on a sample of polystyrene-poly(vinyl methyl ether) polymer blend with layered-silicate nanoparticles [177].

5.2.4 Relevance of TEM in Morphology Studies of Organic Materials

Electron microscopy has the resolution and investigation capability to study and characterise thin films: it can analyse the morphology down to nm scale or more and identify the components of a blend, their structure and even their chemistry. Well ordered phases such as crystals and, to a lesser extent, nanocrystals can be studied (see 2.4.1.1), with particular focus on their structure, while different amorphous region can be distinguished according to their average atomic number and presence of heavy atoms (see 2.4.1.2). Specific elements and molecules can be detected too, by means

of EELS spectroscopy (see. 2.4.2.2), even though we did not use that technique in this chapter. In case of organic materials, these analyses are relevant for studies of morphology in general and for polymer blends in particular, as interfaces are especially relevant. It is however necessary to consider degradation of the organic specimen because of the energetic electron beam. Both structural changes and material loss are possible [69], which could result in considerable alteration. It is then essential to assess (and minimise) these effects on the specimen, to determine whether the results refer to the original specimen or to its damaged version.

Another detrimental effect is the possible appearance of artefacts, as big values of defocus might be necessary. However a huge defocus may introduce deformations in the image [69] beside simultaneously increasing the contrast. This is necessary because the density of many organic materials is typically similar, so little information can be detected by mass-thickness contrast (see par. 2.4.1.2) unless defocus is introduced. Moreover, these materials are normally amorphous, so the diffraction effect does not provide a relevant signal.

The length scale of organic materials is in the order of nm for crystalline structures and up to microns for interfaces of different phases.

5.3 Preparation of Specimens

The preparation of the F8BT:TFB polymer solutions is described in the PhD thesis of Dr. Kalloudis [8]. CdSe quantum dots were isolated from the original toluene solvent by addition of methanol and centrifugation. Then *p*-xylene was added to QDs to reach a concentration of 5 mg/ml: this solution was shaken and underwent ultrasonic bath for 60 minute. This suspension was finally mixed with the 1:4 weight ratio F8BT:TFB solution. Droplets of all the blends (F8BT:TFB with 1:1 weight ratio concentrations, with 1:4 ratio and 1:4 w/w with CdSe QDs) were spin coated (spincoater SPIN150-NPP, SPS-Europe, Putten, the Netherlands) at 4000 rpm for 90 seconds, on freshly cleaved mica sheets (Agar Scientific, Essex, UK) in ambient conditions, producing ultrathin films (roughly 60 - 80 nm). Upon spin cast all the thin films were dried with a stream of nitrogen.

The composite thin film layers were lifted off from mica substrates by gentle immersion into a deionized water bath. The film was then placed on a 200 square mesh copper grid. The specimens were analysed in a FEI Tecnai T20 transmission electron microscope (TEM) EM (FEI, Oregon, United States of America), operated at 200 kV and equipped with an Olympus-SIS Megaview III CCD camera (Olympus Soft Imaging Solutions GmbH, Münster, Germany). We used an objective aperture of 20 μm and defocus value of approximately 10 μm . Digital Micrograph (Gatan, Abingdon, UK) was used for image processing.

STEM analyses were performed with the same sample preparation on a FEI Tecnai TF20 microscope with Schottky FEG gun working at 200 kV and equipped with ADF

and BF STEM detectors, a Gatan Enfina EEL spectrometer and a EDAX EDX spectrometer. The imaging settings for STEM analysis were approximately 9 mrad for the probe convergence angle (α) and 13 mrad for the collection angle (β), corresponding to a probe size of roughly 0.5 nm.

AFM analyses were performed by Dr. Kalloudis on a Bruker AFM Multimode/Nanoscope IIIa (Bruker, Santa Barbara, CA, USA), using RTESP or RTESPA Bruker cantilevers: their spring constant is 40 N/m and the resonant frequency is 300 kHz. Analyses were carried on using “light tapping” mode, in order to have good contrast while minimising the damage on the soft polymer blend. The set-point amplitude ratio, which is the fraction of free oscillation and scanning amplitudes, was close to 1. AFM Image processing employed the Scanning Probe Image Processor software (SPIP, Image Metrology, Hørsholm, Denmark), while the comparison between AFM and TEM images employed the Gwyddion software package [178].

5.4 Results and Discussion

Morphology of F8BT:TFB 1:1 and 1:4 (weight ratios) specimens were investigated by BF-TEM, before and after addition of CdSe quantum dots.

The F8BT:TFB polymer blends, without QDs in this case, when investigated by transmission electron microscopy showed the presence of phase-separated domains, which were detected in the AFM height data [8] (see figures 5.3 and 5.4). An extensive analysis of the domains width is presented, together with considerations on the aspect of the phases in TEM and AFM images.

5.4.1 Analysis of F8BT:TFB Polymer Blend

The TEM images of organic samples are usually based on mass-thickness contrast (see 2.4.1.2), which is related to the concentrations of elements with higher atomic number. This leads to attribute the darkest domain from TEM and thickest areas in AFM images to F8BT [8], which contains heavier elements than TFB, consistently with a previous study of vertical segregation in F8BT:TFB thin film [161]. Moreover, comparable lateral segregation in 1:1 thin film was reported [159, 160, 161], but it was on the micrometer scale. Specifically, Kim et al. [160] investigated thin films of F8BT:TFB ($M_n = 108$ kg/mol and $M_n = 56$ kg/mol respectively), in 1:1 weight ratio, by optical microscopy and micro-Raman spectroscopy and they found F8BT domains upon TFB ones, which created an interface with the substrate.

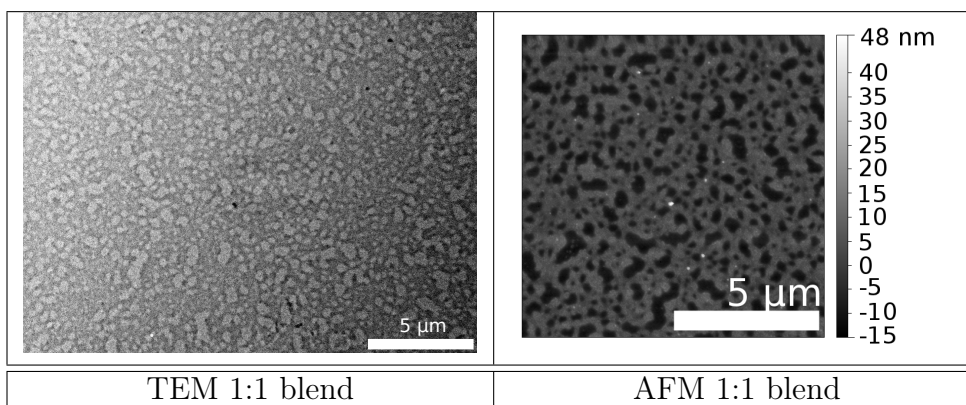


Figure 5.3: Transmission electron microscopy and AFM height images of F8BT:TFB 1:1 weight ratio thin film. The AFM data are provided Dr. Kalloudis, Edinburgh University.

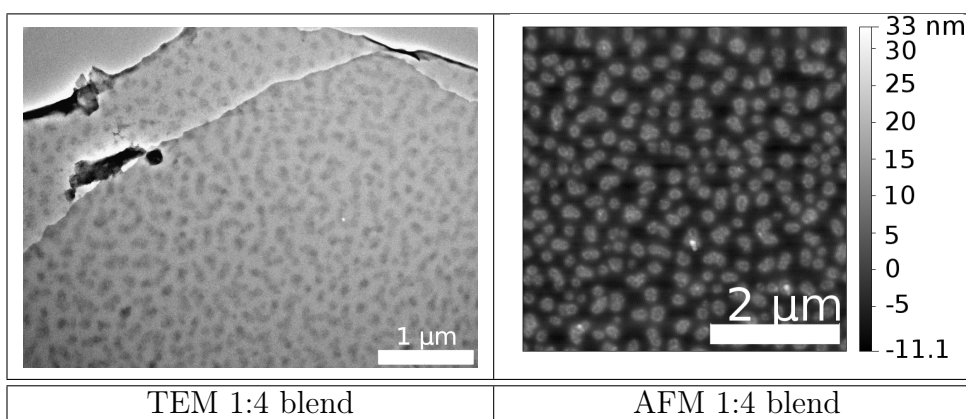


Figure 5.4: Transmission electron microscopy and AFM height images of F8BT:TFB 1:4 weight ratio thin film. The AFM data are provided Dr. Kalloudis, Edinburgh University.

The width of the domains in the 1:1 ratio sample varies between approximately 0.5-1 μm , for both TEM and AFM data (see fig.5.4). On the other hand, the 1:4 ratio sample shows domains which are consistently smaller, about 0.1-0.2 μm (see fig. 5.4). In order to provide a more accurate description of the morphology, the size of phases in two samples was investigated and the results from AFM and TEM were compared. In order to improve the accuracy of the analysis, our data underwent some modifications like background interpolation and subtraction, FFT filtering and correction of AFM scan artifacts (like the “scars”, lines of constant brightness from where the tip lost contact with the specimen). The phase identification was then performed on these improved images, using a threshold level (an example is shown in fig. 5.6 and 5.5, for AFM and TEM images respectively): all areas within a given range of brightness were considered to be the same phase. The threshold level was set manually for every image, in order to properly detect TFB phases in 1:1 ratio samples and F8BT areas in 1:4 ratio

specimens: this was necessary because automated procedures did not provide accurate identifications. This process was applied to both AFM and TEM data, even though the brightness corresponds to a different physical quantity, namely height or electron intensity. All the image filtering and the phase identification steps were performed with the Gwyddion software [178].

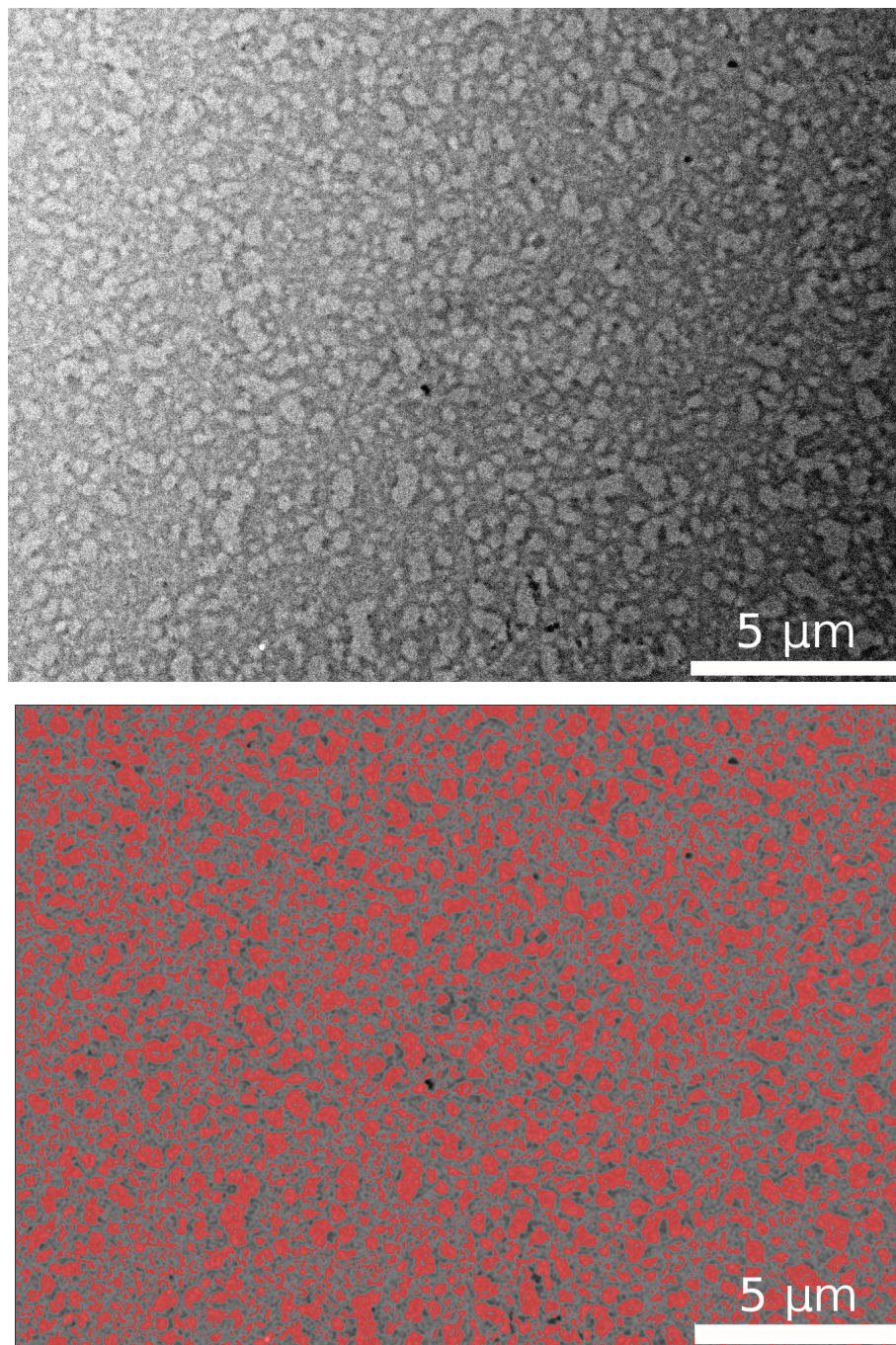


Figure 5.5: An example of TEM image F8BT:TFB 1:1 weight ratio and corresponding phase identification by use of manual threshold (areas in red). The lower picture is a part of the upper image where the phases are more clear. Background subtraction and FFT filtering were applied on the original TEM image before the phase identification.

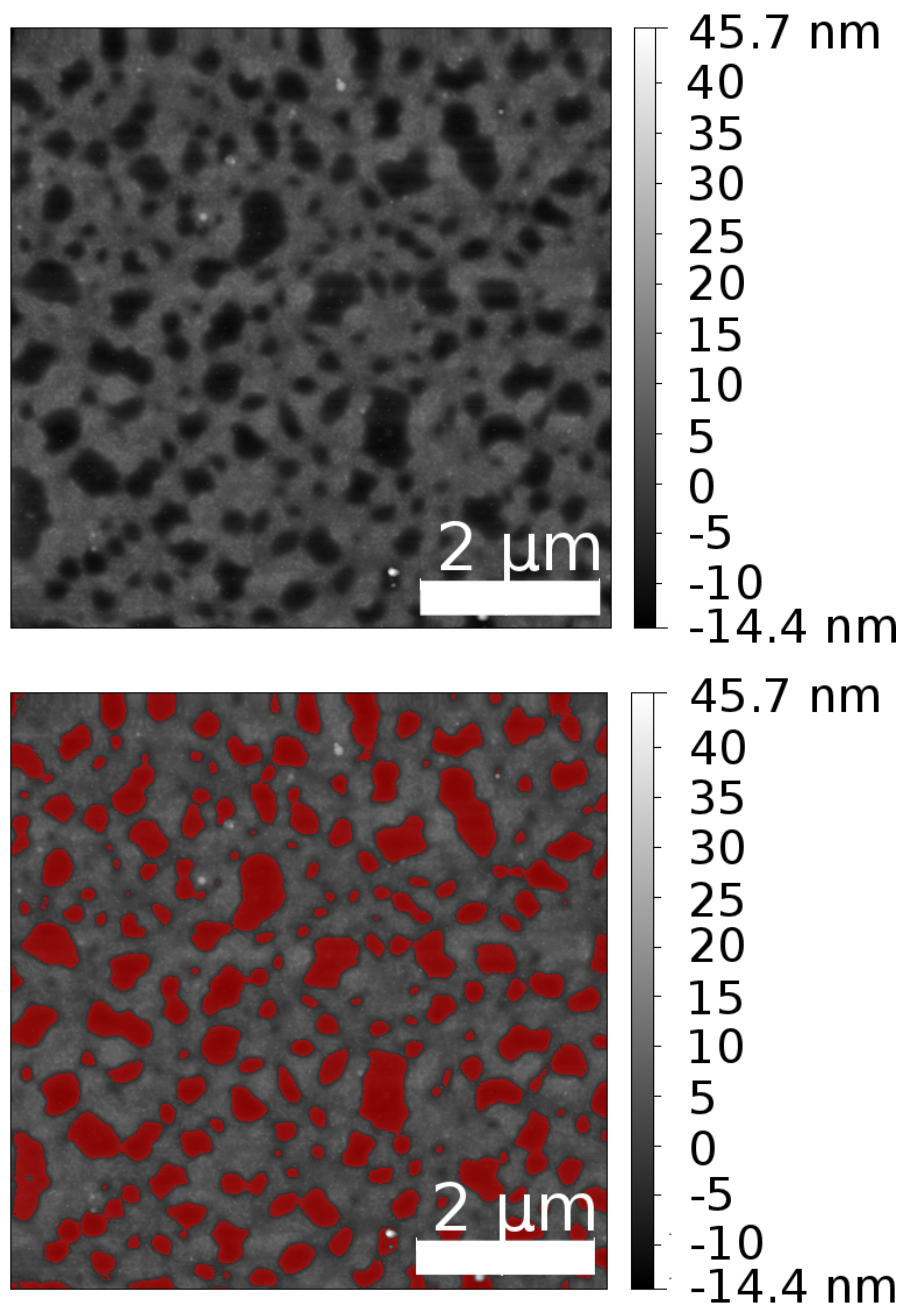


Figure 5.6: An example of AFM height image F8BT:TFB 1:1 weight ratio (courtesy of Dr. Kalloudis, Edinburgh University) and corresponding phase identification by use of manual threshold (areas in red). The corresponding surface areas are shown in fig. 5.7.

The areas of the identified phases were measured and plotted using histograms: an example is shown in fig. 5.7. A high number of small areas is detected as a consequence of noise: this is caused by small group of pixels which happen to have the same brightness of real phases, so the corresponding area is calculated and included in the histogram. However, the image in fig. 5.6 point approximately at the actual area of F8BT and TFB phases and the corresponding value can be identified in the histograms. In fact, both fig. 5.6 and 5.7 suggest the presence of areas in the order of

approximately $0.1\text{-}0.15 \mu\text{m}^2$, even though the variance is considerable and the influence of noise is very noticeable in the histogram.

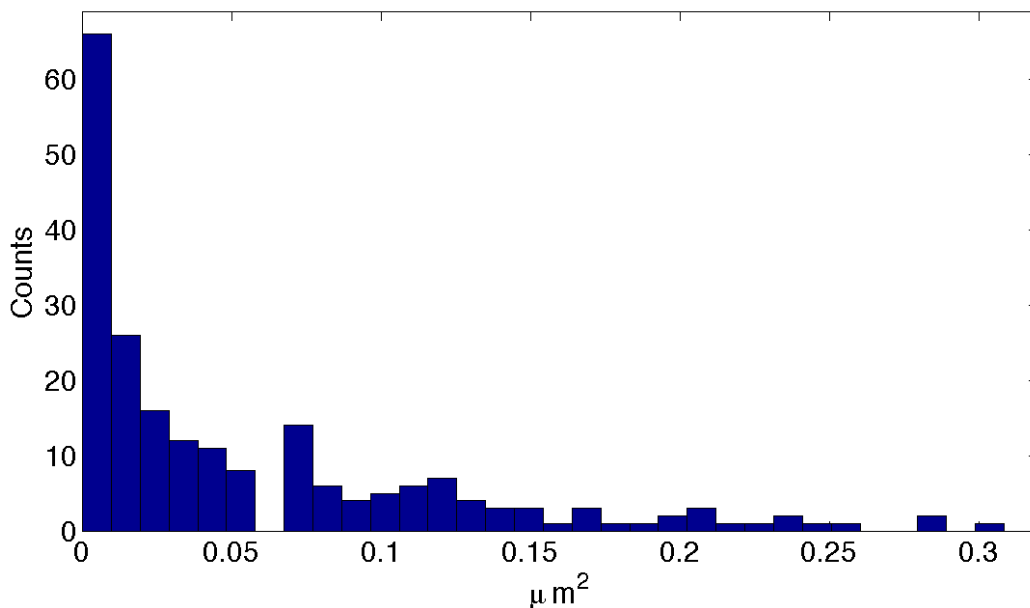


Figure 5.7: An example of areas' histogram of detected phases in 1:1 weight ratio sample (from AFM data in fig. 5.6). The huge quantity of small areas (i.e. the leftmost column) is due to noise in the image, while the actual areas are believed to be in the order of $0.1\text{-}0.15 \mu\text{m}^2$.

In order to provide a better statistic, the results from more images were aggregated when possible: 4 AFM measurements for the 1:1 ratio sample, 6 for the 1:4, as well as 2 TEM images for the 1:4 ratio. In case of TEM analysis of the 1:1 composition sample, a single image including a large number of domains (such as fig. 5.5) was considered adequate. Eventually, at least a hundred domains or more (in addition to noisy pixels) were investigated for each of the comprehensive histograms. All these findings are plotted in fig. 5.8 and 5.9, for the 1:1 and 1:4 weight ratio respectively: the results from AFM and TEM are both shown for comparison. The leftmost column in each graph was partly excluded because it is deemed to be heavily influenced by noise. It is still useful however to consider the phase sizes in the images, such as fig. 5.5, to help the interpretation of the histograms of 1:1 weight ratio sample: areas of roughly $0.2 \mu\text{m}^2$ can be seen in the pictures (see fig. 5.3). A similar order of magnitude can be seen in the corresponding plot from TEM data, in fig. 5.8. In particular, the TEM histogram shows small areas, mostly below $0.2 \mu\text{m}^2$. Similarly, the AFM data present values concentrated below $0.25 \mu\text{m}^2$ (see fig. 5.8), confirming the similarity noticed in TEM and AFM images. These values are different from the AFM results reported in literature [160], which present $2\text{-}5 \mu\text{m}$ domain size: some areas are close to that extension in both images of fig. 5.3, but the majority of domains present a smaller size in our data, roughly $0.5\text{-}1 \mu\text{m}$.

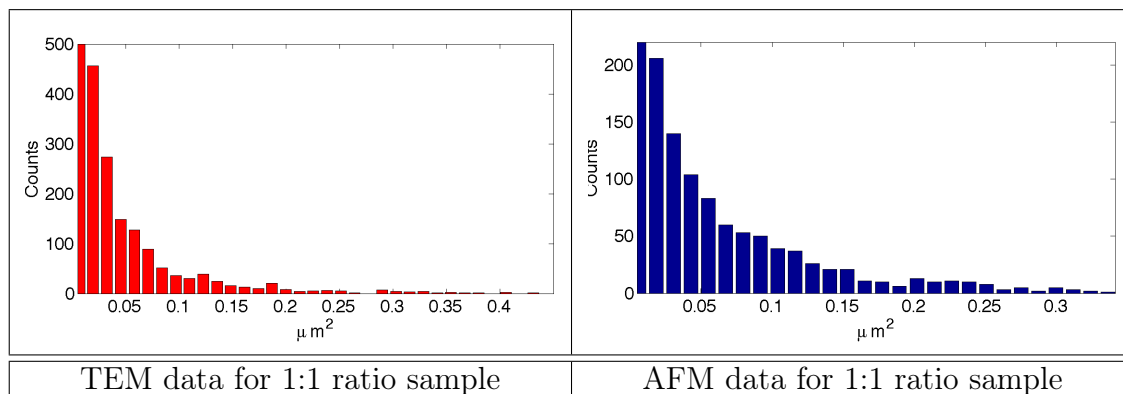


Figure 5.8: Surface area histograms of phases in 1:1 weight ratio samples, from AFM and TEM images. Noise tends to introduce a high number of small areas (the leftmost column), which are not entirely presented. There seems to be a relevant fraction of areas below $0.2 \mu\text{m}^2$ for the TEM data and $0.25 \mu\text{m}^2$ for the AFM histogram.

The 1:4 weight ratio sample, on the other hand, present similar results. In fig. 5.9 the TEM data show a different distribution, where most of the areas are in the range of $0.005\text{-}0.02 \mu\text{m}^2$, while a great amount of domains in the AFM data are in the order of $0.02\text{-}0.05 \mu\text{m}^2$. This last histogram also show an amount of areas comparable with the value in the leftmost column, which is not partially excluded in this plot. These latter values are close to those reported in literature for a similar composition of F8BT:TFB: Kim *et al.* [160] reports $0.5\text{-}1 \mu\text{m}$ domain width for a 1:3 weight ratio sample. The measures from the different techniques in the 1:4 ratio sample are similar and point towards an average area well below that of 1:1 ratio samples: it is at least an order of magnitude smaller.

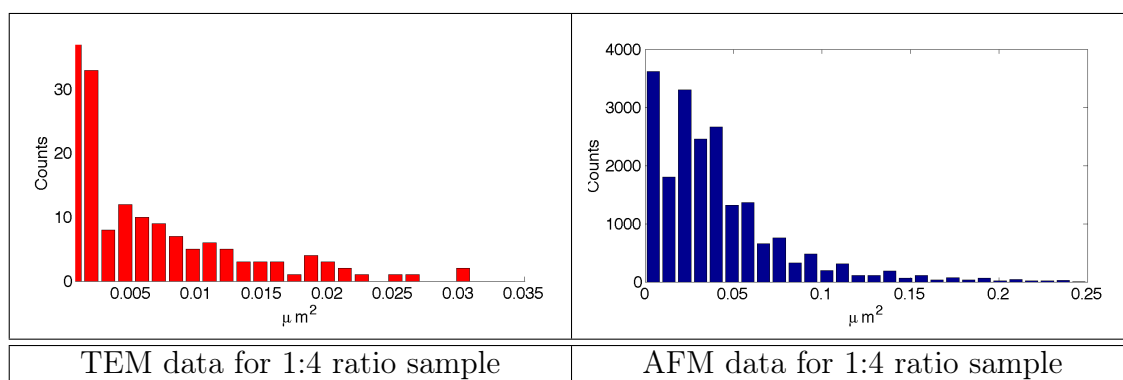


Figure 5.9: Surface area histograms of phases in 1:4 weight ratio samples, from AFM and TEM images. Noise tends to introduce a high number of small areas. The average area seems to be approximately below $0.02 \mu\text{m}^2$ for the TEM data and concentrated between 0.02 and $0.05 \mu\text{m}^2$ in the AFM histogram. These values are well below those of the 1:1 ratio sample (which are in the order of $0.2 \mu\text{m}^2$).

The influence of quantum dots was also considered on domains, as it was reported that nanoparticles can affect the morphology of the blend (see par. 5.2.3). A specimen prepared with 1:4 weight ratio composition and mixed with CdSe quantum dots was investigated by TEM, as the previous samples. Three different TEM images were used, QDs clusters were removed from the picture adding a mask to avoid confusion in the identification of areas. 91 domains were identified, in addition to the noisy pixels. The measured areas are shown in fig. 5.10. The histogram presents a small peak around $0.01 \mu\text{m}^2$, which is within to the range detected in the pure 1:4 w/w specimen: 0.005 - $0.02 \mu\text{m}^2$. A reduction of size was expected, according to the literature (see par. 5.2.3) but our results are not accurate enough to support this hypothesis.

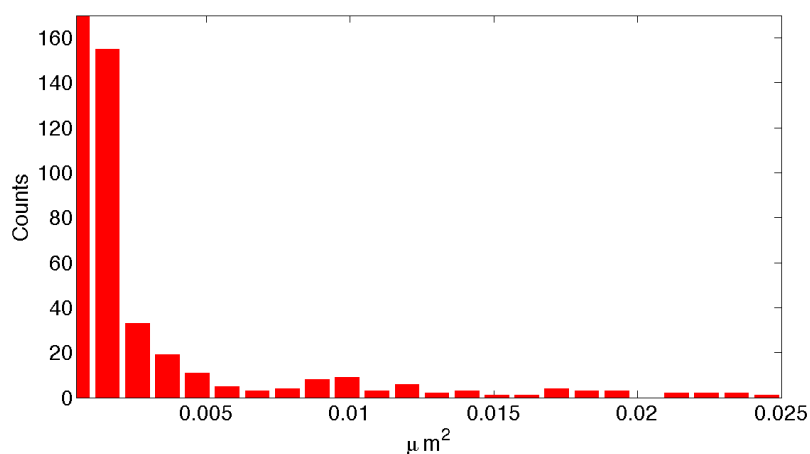


Figure 5.10: Surface area histograms of phases in 1:4 weight ratio samples mixed with QDs, from TEM images. Noise tends to introduce a high number of small areas, but the two measures do not agree: the average area seems to be between 0.4 and $0.1 \mu\text{m}^2$.

5.4.2 Analysis of CdSe Quantum Dots in F8BT:TFB Polymer Blend

The detection and analysis of quantum dots was entirely a matter of electron microscopy, since both nanometer resolution and in-depth investigation beyond surface are necessary to detect nm wide nanoparticles embedded in the thin film. The significant density and structural difference between QDs and the conjugated polymers allowed to detect nanoparticles and the polymer blend phases to be discerned. This is thanks to additional diffraction contrast from the crystalline quantum dots in the amorphous matrix. BF-TEM data in fig. 5.11 present quantum dots as black, a consequence of diffraction contrast. The F8BT dark phase and the TFB underlying matrix can also be easily noticed.

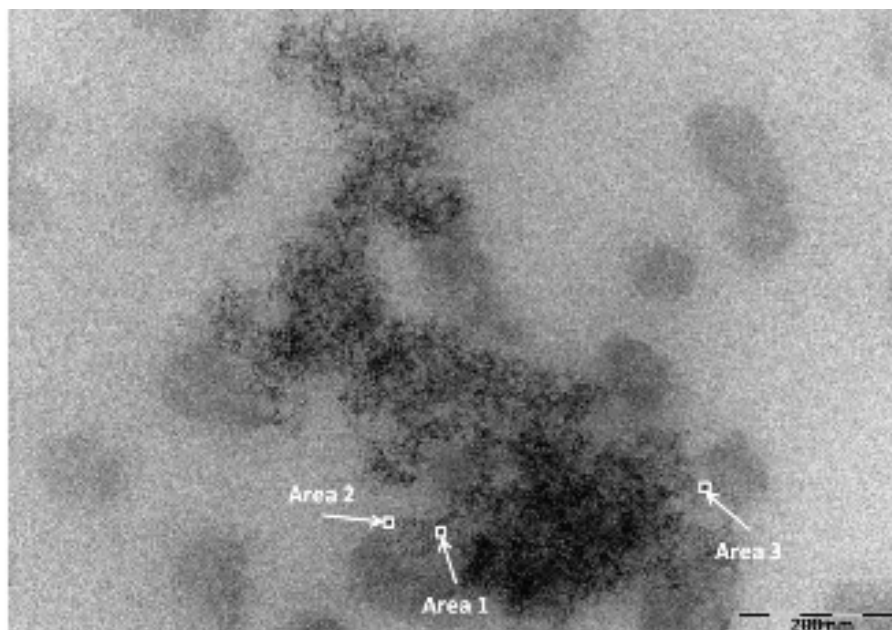


Figure 5.11: BF-TEM image of F8BT:TFB 1:4 thin film with quantum dots. The phase-separated polymer blend domains and the segregated QDs (resembling a black cloud) are presented in the image. Three different regions (area 1, 2 and 3) in the interface of F8BT and TFB domains were studied for QD detection.

Since the diffraction contrast from the QDs could be better observed by HAADF STEM imaging, the same sample was investigated with that technique: the results are shown in fig. 5.12. A morphology similar to previous findings (see fig. 5.11, for example) can be discerned. The QDs provide a good intensity, as expected, but the F8BT phases are quite dim and do not present a similar contrast, casting a doubt about the presence of nanoparticles within those domains.

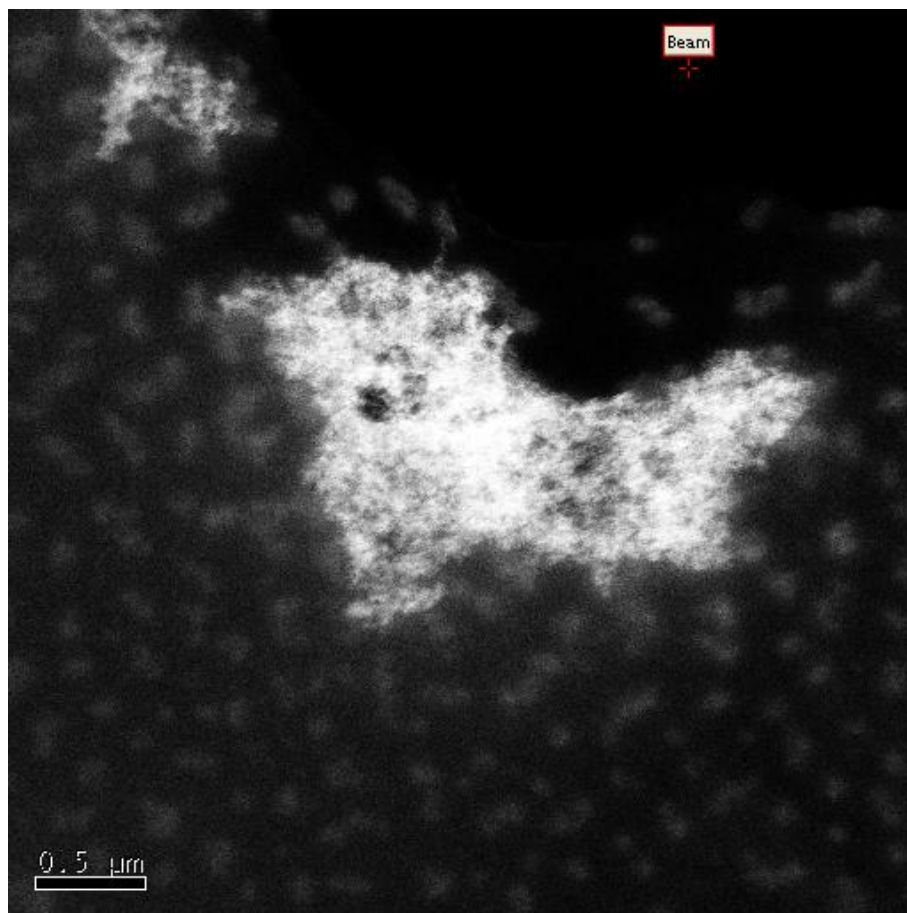


Figure 5.12: HAADF STEM images of F8BT:TFB 1:4 thin film with quantum dots. The phase-separated polymer blend domains, consisting of the dark matrix and grey areas, and the QDs (the white regions) are presented in the image. The position of the beam after the measurement is marked in the top. Image acquired by Dr. McFadzean.

The contrast in the images was then investigated to detect and quantify the expected changes due to QDs. Two samples were analysed, both with 1:4 weight ratio blend: one had quantum dots in the blend, while the other did not. For each sample the brightness of three different areas were measured: in F8BT phases, TFB-rich areas and empty zones (see fig. 5.13), the latter being used as internal reference for beam intensity, as it can be detected where the sample is absent. The knowledge of the beam intensity allows to compare measures taken under different illumination conditions, as well as to compensate the automatic contrast adjustment of the image recording system.

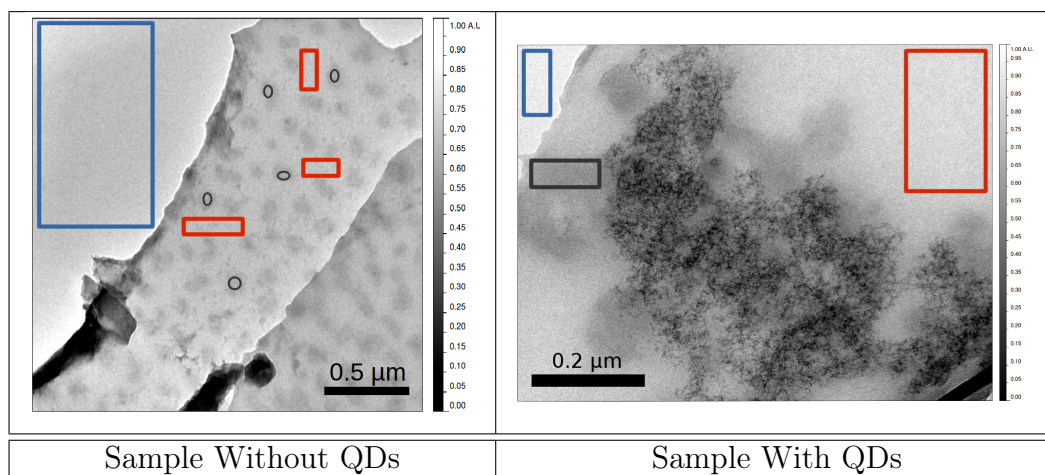


Figure 5.13: BF-TEM images of a F8BT:TFB 1:4 thin film without QDs (on the left) and with QDs (on the right). Areas of investigation of F8BT, TFB and beam intensity are marked: measured F8BT phases are shown in black, TFB domains in red and empty areas in blue. The brightness of the images was normalised, as shown by the colour bar beside the images.

It is worth noting that the brightness detected in the empty areas is not the highest value in the image, because the defocus causes the edge of the sample to be extremely bright: this effect is called a Fresnel fringe and it can be seen in fig. 5.13. The automated contrast adjustment then changes the brightness levels, resulting in empty areas near the edge which are darker than the specimen (see tab. 5.1): however, the relative contrast level are maintained, so the brightness values of the two phases were normalised against the brightness of the empty area. This procedure was applied to many locations or to large areas in the samples, then the average brightness level was considered for normalisation. The contrast was calculated as a difference in the normalised brightness between the dark F8BT phase and the light grey TFB: the differences were in a range of 10%-22% in three samples without QDs, while 20% was measured in the specimen with nanoparticles: the details are presented in tab. 5.1. These percentages are referred to “empty area” intensity, so, for example, the brightness change between a completely black area and the measured empty zone would be 100%. The quantum dots do not seem to have a decisive influence on the brightness change and contrast, since the value of the sample with QDs is in the range of values detected from the sample without those nanoparticles.

	Sample 1 (No QDs)	Sample 3 (No QDs)	Sample 3 (No QDs)	Sample with QDs
Illumination from empty areas	0.71	0.63	0.49	0.93
F8BT (dark phase)	0.63 (88%)	0.61 (96%)	0.67 (137%)	0.66 (71%)
TFB (light grey phase)	0.70 (99%)	0.68 (106%)	0.56 (115%)	0.84 (91%)
Difference	11%	10%	22%	20%

Table 5.1: Average values of normalised brightness and relative percentages as referred to illumination in empty areas. Some examples of acquisition areas are presented in fig. 5.13. Values above 100% are due to extremely bright areas near the edge of some specimens, as a result of the Fresnel fringe.

However, the identification of single quantum dots was carried on, in order to identify their position and investigate possible patterns. The intensity profiles in fig.5.14 were measured over single quantum dots, averaged over the width of the QDs (that is approximately over 2nm). The drop of intensity value is attributed to the quantum dots because their crystalline structure creates diffraction contrast with the amorphous polymers: the Bragg diffraction deviates the electron beam from the optical axis, where the BF detector is, resulting in a lower intensity for such nanoparticles. Moreover, the size of the low intensity areas is consistently similar to that expected for QDs, which is roughly 2.1 nm (according to supplier's information).

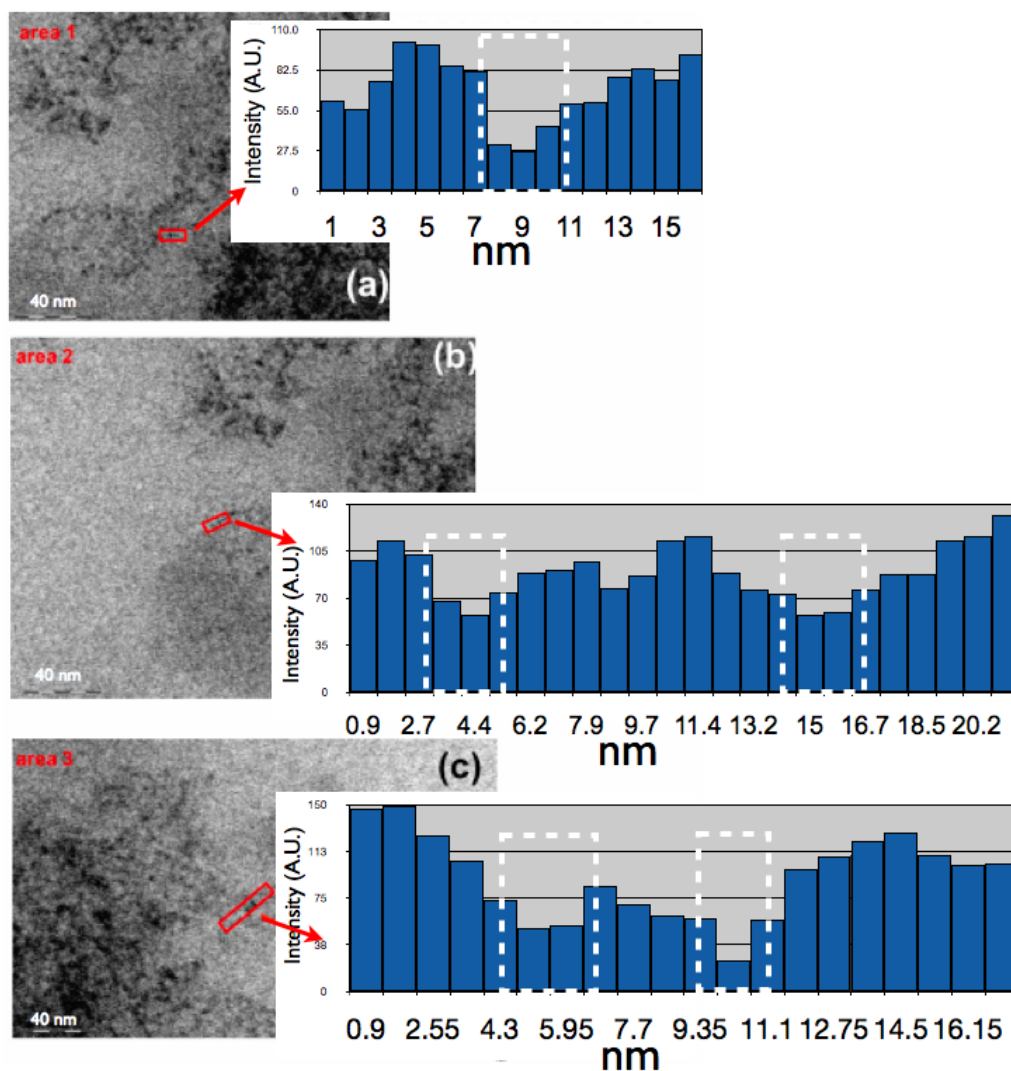


Figure 5.14: BF-TEM images and intensity profiles of F8BT:TFB 1:4 thin film with quantum dots (zoom of areas 1, 2 and 3 from fig.5.11). Three different regions (area 1, 2 and 3) in the interface of F8BT and TFB domains were studied for QD detection. Intensity profiles were taken across the red boxes of area 1(a), area 2(b) and area 3(c). Intensities were averaged over the width of the quantum dot. Dashed white rectangles are placed above the low intensity regions of quantum dots. Their size is approximately 2nm, as expected.

Even though the detected contrast and brightness level can be shared with samples without QDs, the measures in fig. 5.14 were performed near a quantum dots cluster (see fig.5.11 for an image of the entire area of investigation); together with the detected sizes in the intensity profiles, which match those of QDs, this seems to strongly support the conclusion of the identification of QDs in our measures. However, no consistent indication of distribution patterns could be proved, either by BF-TEM or STEM.

5.5 Conclusions

BF-TEM capabilities were investigated and applied to real case of technological relevance. Together with Dr. Kalloudis, we investigated the phase-separation and morphology of F8BT:TFB polymer blend in thin film, as well as the changes introduced by addition of quantum dots. BF-TEM was used to analyse the blend and its conformation, but mostly to detect single quantum dots and to study their distribution and influence on phase separation. AFM data were used for comparison and to complement our conclusions. Phase-separation was not affected by quantum dots, as domains showed no significant change of size when nanoparticles were added to the blend. In case of 1:1 weight ratio TFB rich sub-micrometer domains were embedded in a F8BT rich layer. In the 1:4 F8BT:TFB polymer blend phase-separation changed, presenting a continuous TFB rich matrix, populated by F8BT domains whose size was found to be below $0.02 \mu m^2$.

The CdSe nanoparticles were detected in the blend by BF-TEM and HAADF STEM: single particles were located but no consistent pattern in the nanoparticles distribution could be detected, either by STEM analysis or contrast measurements.

Chapter 6

General Conclusions and Suggested Future Work

6.1 General Conclusions

Electron microscopy and various related techniques, namely STEM and EELS, proved effective in describing the morphological properties of useful materials of different kind and related to different devices. Inorganic, organic and composite samples were investigated, providing useful information on their morphology, which can be linked to performances and production process: this will help to understand the best preparation method and the effects of the production parameters. Different length scales were investigated effectively, such as the angstrom scale or micrometer one, to analyse the relevant distance for the properties of the materials: micron wide interfaces in case of polymer blends and single unit cells in case of ceramic microwave dielectrics.

6.1.1 Atomic Structure and Chemistry of $Ba_{6-3x}Nd_{8+2x}Ti_{18}O_{54}$ Microwave Dielectric

Microwave ceramics are a class of materials which allows miniaturisation of key components of telecommunication devices, such as mobile phones. The main relevant properties of these ceramics are influenced by their atomic structure and chemistry, which were investigated using HAADF data and EELS spectroscopy on a Barium Neodymium Titanate ($Ba_{6-3x}Nd_{8+2x}Ti_{18}O_{54}$) sample. An extensive data analysis of those experimental results led to the description of the unit cell of this material with sub-Å precision. Study of samples with different compositions and cooling rates showed that the crystal structure was not affected by those factors. The composition of the sample was also probed with atomic resolution, showing presence of Ba in Neodymium sites, namely with a bigger density in $Nd[3]$, a lower one in $Nd[2]$ sites and the least in $Nd[1]$.

Our findings can constrain and integrate further Rietveld refinements of X-ray diffraction and lead to a more comprehensive description of the atomic structure of $Ba_{6-3x}Nd_{8+2x}Ti_{18}O_{54}$.

6.1.1.1 Proposed Complementary Characterisation of $Ba_{6-3x}Nd_{8+2x}Ti_{18}O_{54}$

Our conclusions could be integrated and validated by additional simulations and analyses: for example it would be interesting to know the effect of the beam spreading on EELS spectroscopy. A simulation of our areal densities and EELS data could help to identify the contribution of various elements and sites, in order to validate the fairly complicated model we present. The integration of our result in Rietveld refinements of X-ray can both support our findings and improve the description. It could also be interesting to apply these two techniques to other materials, in order to prove the potential of these two complementary methods, particularly in the detection of substitution ratios and patterns in crystals.

A more detailed investigation of $Ba_{6-3x}Nd_{8+2x}Ti_{18}O_{54}$ could benefit from a 3D description, which could come from the same sample in a different orientation. This could lead to a better characterisation of atomic position and substitution in various sites, even though it appears more complex to identify the sites (for example see fig. 4.17).

It would also be interesting to measure the properties of the materials, such as permittivity, to link it to our crystallographic model and to the preparation methods, in order to better understand the effects and consequences of the preparation to achieve an optimisation of the process.

6.1.2 Morphology Study of Organic-Inorganic Compounds

The conjugated polymers are considered a low cost alternative to inorganic semiconductors in many applications. The addition of quantum dots in the blend caused improvement of the efficiency in optoelectronic devices based on conjugated polymers. However, the nanoscale structure of the blend can influence the performance of devices, so it needs to be studied. The F8BT:TFB is one of the relevant compounds for optoelectronic applications and its morphology in case of low molecular weight was studied in this work. A thin film of F8BT:TFB polymer blend was investigated: the 1:1 and 1:4 weight ratio composition were analysed by BF-TEM and the data were complemented by AFM measurements. The phase separation changed significantly: the 1:1 ratio specimen presents TFB sub-micrometer domains in a F8BT matrix; in the 1:4 weight ratio sample, F8BT formed separated phases in a TFB layer, whose size is below $0.02 \mu m^2$. The introduction of CdSe quantum dots in 1:4 weight ratio blend was investigated as well, with specific focus on both domains segregation and single quantum dot detection. The majority of QDs was found to be clustered, even though some single nanoparticles were detected. The quantum dots did not present any specific pattern in their dispersion and the size of polymer domains did not show any noticeable difference after the addition of QDs. Based on these result, the nanoparticles are not expected to be hugely beneficial for a device based on this blend.

6.1.2.1 Proposed Polymers-QDs Blend Characterisation Improvement

A further analysis of quantum dots dispersion in the phases could help to characterise the morphology with more detail, which would improve the design of related devices. A 3D reconstruction of the thin film would be an interesting contribution to the characterisation of quantum dots dispersion, relative to the polymer phases. The electron microscope has the ability to use tomography techniques and this sample is promising, considered the good contrast of the QDs and its good durability under the electron beam.

Appendix

MATLAB Scripts List

I personally wrote the following scripts (whose name are in *italic*, code is shown after the description), with the exception of *ploterr*, which was published on internet [219] by Felix Zoergiebel, Copyright © 2008, All rights reserved. All scripts were written and used on MATLAB® software, on the 7.10.0 (R2010a) 64-bit version.

Ploterr plots points and their error margins in 2D. It was used to create map of unit cells and the site variances.

Cellan identifies adjacent unit cells in a matrix. It requires the global list of sites from the image interpolation and one initial unit cell. The number of cells to be searched can be decided, as well as their position relative to the first one. The initial cell is used to calculate lattice constants, which are used as characteristic distances to locate additional cells. New sites are expected to be found by adding or subtracting integer number of lattice constants from initial coordinates: an error margin is set for acceptance. If no site is found, or more than one are found within the error zone, the *Atom_search* script is used to select manually the right atom. The resulting cells are overlapped by aligning to the their central atom.

```
function [ cellx , celly ] = cellan( datax , datay , ucx , ucy )
%   ucx , ucx have to be not centered
%   corners of rectangular cell , Perovskite is suitable

[ minx , imix ] = min( ucx );
[ miny , imiy ] = min( ucy );
[ maxx , imax ] = max( ucx );
[ maxy , imay ] = max( ucy );

na=length(ucx); %number of atoms in the cell
nd=length(datax); %number of atoms in data

corni=[imix imiy imax imay];
corn=find( diff( sort( corni ) ) ==0 , 1);%test for same corners

if ~isempty( corn )
```

```

theta=pi/4; % in Radians
rotm=[cos(theta) -sin(theta); sin(theta) cos(theta)];

rcx=rotm(1,:)*[ucx; ucy]; %counterclockwise rotation
rcy=rotm(2,:)*[ucx; ucy];

[~, imix]=min(rcx);
[~, imiy]=min(rcy);
[~, imax]=max(rcx);
[~, imay]=max(rcy);
corni=[imix imiy imax imay];

end

a1=[ucx(imax)-ucx(imiy) ucy(imax)-ucy(imiy)];
a2=[ucx(imiy)-ucx(imix) ucy(imiy)-ucy(imix)];

figure
plot(datax, datay, '.', ucx, ucy, 'r.')
hold on
title('Titanium in Blue, Cations in Black')

t=3.5; %threshold

center=[(maxx+minx)/2 (maxy+miny)/2];

shiftx=[ucx-center(1)]; % center is the origin to be shifted
shifty=[ucy-center(2)];

inew=zeros(na,1);
newx=shiftx;
newy=shifty;
num=1;

%% TRIAL FEW CELLS
% s_a=[0 1; 0 -1; 1 0; -1 0; 0 0; 0 2; 0 -2; 2 0; -2 0];

s_a=[0 0; 0 1; 1 0; 0 -1; 0 3; 1 -2; 1 -1; 1 3; 1 4; 2 3];

num=length(s_a);

```

```

cellx=[zeros(num,length(shiftx))];
celly=[zeros(num,length(shiftx))];

for s=1:length(s_a)

    for j=1:na

        px=center(1)+shiftx(j)+s_a(s,1)*a1(1)+s_a(s,2)*a2(1);
        py=center(2)+shifty(j)+s_a(s,1)*a1(2)+s_a(s,2)*a2(2);

        ind=find( (abs(datax-px)<t) & (abs(datay-py)<t));
        % match between data and shifted center

        if length(ind)~=1
            inew(j)=atom_search(datax,datay,px,py,shiftx,shifty,j);

            else inew(j)=ind;
                display('atom found')
            end

        newx(j)=datax(inew(j));% original data
        newy(j)=datay(inew(j));

        end

    uc=[imix, imay, imax, imiy, imix];
    plot(newx(uc),newy(uc),'k')

    cellx(s,:)=newx;
    celly(s,:)=newy;

end

% center does not have to be an atom,
% just x and y but need "local" centre
end

```

Atom_search allows to manually identify which site actually corresponds to a given atom of a unit cell. This is necessary when the expected position of the unit cell does not match the real data. The script plots the expected position of a cell over the actual coordinates of nearby sites. The position of the ambiguous atom is presented in a different colour and the user can click on the site which is deemed correct with the

mouse. Its coordinates are returned to the *cellan* script.

```
function [ ic ] = atom_search( datax , datay , px , py , shiftx , shifty , i )

j=0;

while j==0
    pcx=shiftx-shiftx(i)+px; pcy=shifty-shifty(i)+py;
    figure
    plot(pcx,pcy,'ko',datax(1:247),datay(1:247),'.',...
%First 247 coordinates refer to one element
        datax(248:end),datay(248:end),'k.',...
%Second element, from 248 on (different
        px,py,'rs')
%colour in the plot)

    axis([px-60 px+60 py-100 py+100])
    [x,y]=ginput(1);
    index=find( (abs(datax-x)<5) &...
                (abs(datay-y)<5));

    close % close last figure

    axis auto
    ic=index;

    if isempty(index) || length(index)>1
        j=0;
    else
        j=index;
    end
end

end
```

Seg_sort allows to select all the sites close to a line drawn by the user. It was used to select particular sites, such as Nd[2] and Ba ones, from the global list of coordinates. An error margin can be set with the input: all coordinates within that distance from the drawn line will be sorted and returned by the script.

```
function [s,n]=seg_sort(x,y,mar)
% Detect ONLY points near the segment defined by user
```

```

hold on
plot(x,y, '. ')
title('RIGHT MOUSE BUTTON TO FINISH')
but = 1;
n=0;
while but == 1

    n = n+1;
    [xi, yi, but] = ginput(2);
    plot(xi, yi, 'r-', 'LineWidth', 2)
    xy(n,:) = [xi.' yi.']; %x1 x2 y1 y2

end

hold off
close

for i=1:n
    if abs(xy(i,1)-xy(i,2)) >= 0.01*mar
        p=polyfit(xy(i,1:2), xy(i,3:4), 1);
        ind=find( abs(p(1)*x+p(2)-y) < mar & ...
                min(xy(i,1:2)) <= x & x <= max(xy(i,1:2)) );
    else
        ind=find( min(xy(i,3:4)) <= y & ...
                y <= max(xy(i,3:4)) & ...
                abs(xy(i,1)-x) < mar );
    end

    [~, s_ind]=sort(x(ind));
    s.(['line ' num2str(i)])=ind(s_ind);

end
end

```

Pinpoint plots an intensity map and collects a list of pixels selected by the user with mouse clicks. These points are then used by the *maxima* script (see below) to find a local intensity maximum within a given range, selected by the user. The *pinpoint* script is used to find the maximum value of intensity corresponding to atomic columns in areal density maps.

```
function [M9, xp, yp] = pinpoint(map, edge)
```

```

contourf(map) hold on

% Initially , the list of points is empty.
M9 = [];
xp = [];
yp = [];

n = 0;

% Loop, picking up the points.
disp('Left mouse button picks points.')
disp('Right mouse button picks last point.')
but = 1;

while but == 1

    [xi ,yi ,but] = ginput(1);
    plot(xi ,yi , 'ko' , 'MarkerSize' ,12)
    n = n+1;
    xi=round(xi);
    yi=round(yi);
    xp(n)=xi;
    yp(n)=yi;

end

close

[M9,xp ,yp]=maxima(xp ,yp ,map , edge );

end

    Maxima script finds which of the coordinates provided as input correspond to the
    area of highest intensity: a sum of the pixel indicated by the coordinates and the 8
    surrounding ones is considered to identify the highest value.

function [M,Mx,My] = maxima(ix , iy , map, edge)

ix=round(ix); %round to pixels
iy=round(iy);
siz=size(map);

```

```

for at=1:length(ix)
x=ix(at);

if (x<4)
%intensity is analysed in an area 4 pixel wide,around x,y

        x=4;
%original coordinates are scanned, as well as the surroundings

elseif (x>siz(2)-4)

        x=siz(2)-4;

end

y=iy(at);

if (y<4)

        y=4;

elseif (y>siz(1)-4)

        y=siz(1)-4;

end

m=0;

for incx=-1*edge:edge % scan around roi
    for incy=-1*edge:edge

        roix=x+incx;
        roiy=y+incy;
        s=sum([map(roiy-1,roix-1:roix+1)...
                map(roiy,roix-1:roix+1)...
                map(roiy+1,roix-1:roix+1)]);

        %9 pixels

        if (s>=m)

```

```

        m=s;
        M(at)=s;
            %minus minimum in 9 pixels (so it's >0);
        Mx(at)=roix;
        My(at)=roiy;
    end
end
end
end
end

```

Corr scans areal densities of different elements to normalise their concentration and helps the user to label sites according to crystallographic criteria. Namely, sites which are equivalent because of symmetric relations (such as Nd[1] and Nd[5]), have their areal densities grouped together. First, given the maxima found by *pinpoint* areal densities were calculated for areas of 3x3 pixels, approximately corresponding to those of atomic columns. Nearby sites of different elements were considered and their average densities were calculated for normalisation. This procedure includes only neighbouring locations to account for thickness variations. Once normalisation is completed the user can select manually the symmetrically equivalent sites, whose areal densities are then grouped together for later analyses.

```

clc
close all
clear all          % clear previous variables and close figures

load final_x3_corr.mat %load set of data

edge=2;

[Tima9, Tix, Tiy]=pinpoint(Ti05, edge);
[Ndma9, Ndx, Ndy]=pinpoint(Nd08, edge);
[Bama9, Bax, Bay]=pinpoint(Ba08, edge);

mNd9=max(Ndma9);
mBa9=max(Bama9);
nNd=length(Ndx);
nBa=length(Bax);

% rNd_Ba=zeros(1, nNd); % convBa=zeros(1, nNd);
% Ba_map=zeros(size(Ba08)); % Nd_map=zeros(size(Ba08));
Bax_2=Bax;
Bay_2=Bay;
Ndx_2=Ndx;

```

```

Ndy_2=Ndy;

i=find (Bax_2<edge+1);

if size (i)>0
    Bax_2(i)=edge+1;
end
i=find (Bax_2>max( size (Ba08))-edge );
if size (i)>0
    Bax_2(i)=max( size (Ba08))-edge ;
end

i=find (Bay_2<edge+1);
if size (i)>0
    Bay_2(i)=edge+1;
end

i=find (Bay_2>max( size (Ba08))-edge );
if size (i)>0
    Bay_2(i)=max( size (Ba08))-edge ;
end

i=find (Ndx_2<edge+1);
if size (i)>0
    Ndx_2(i)=edge+1;
end

i=find (Ndx_2>max( size (Ba08))-edge );
if size (i)>0
    Ndx_2(i)=max( size (Ba08))-edge ;
end

i=find (Ndy_2<edge+1);
if size (i)>0
    Ndy_2(i)=edge+1;
end

i=find (Ndy_2>max( size (Ba08))-edge );
if size (i)>0
    Ndy_2(i)=max( size (Ba08))-edge ;
end

```

```

% save BaNd08.mat

Ba_map=Ba08/mBa9;
Nd_map=Nd08/mNd9;
for a=1:nNd

    iTi=find( abs(Tix-Ndx(a))<15 & ...
              abs(Tiy-Ndy(a))<15 );

    iTi=find( abs(Bax-Ndx(a))<15 & ...
              abs(Bay-Ndy(a))<15 );

    mTi=mBa9;

    conv=mTi/sum(...
          [Nd111(tiy111(a)-1,tix111(a)-1:tix111(a)+1)...
           Nd111(tiy111(a) ,tix111(a)-1:tix111(a)+1)...
           Nd111(tiy111(a)+1,tix111(a)-1:tix111(a)+1)]);

    iBa=find( abs(Bax-Ndx(a))<15 & ...
              abs(Bay-Ndy(a))<15 );

    peakBa=mean(Bama9(iBa)/mBa9); % already 9 pixels

    convBa(a)=mTi/peakBa;

    rNd_Ba(a)=mTi/(convBa(a)*sum(...
                  [Ba08(Ndy(a)-1,Ndx(a)-1:Ndx(a)+1)...
                   Ba08(Ndy(a) ,Ndx(a)-1:Ndx(a)+1)...
                   Ba08(Ndy(a)+1,Ndx(a)-1:Ndx(a)+1)]));

%scale Ba as well
%Nd scaled up to Ti (9 pixels)

Ba_map(Ndx_2(a)-2:Ndx_2(a)+2,Ndy_2(a)-2:Ndy_2(a)+2)=...
    convBa(a)*...
    Ba08(Ndy_2(a)-2:Ndy_2(a)+2,Ndx_2(a)-2:Ndx_2(a)+2);
%Ba scaled up to Ti (9 pixels)

Nd_map(Ndx_2(a)-2:Ndx_2(a)+2,Ndy_2(a)-2:Ndy_2(a)+2)=...
    mTi/Nd08(Ndy(a) ,Ndx(a) ) * ...
    Nd08(Ndy_2(a)-2:Ndy_2(a)+2,Ndx_2(a)-2:Ndx_2(a)+2);

```

```

% convert Nd peak to Ti KEEP PEAK COORDINATES
% 9 adjacent pixels

end

rBa_Nd=zeros(1,nBa);
convNd=zeros(1,nBa);

for a=1:nBa

    iTi=find( abs(Tix-Bax(a))<15 & ...
             abs(Tiy-Bay(a))<15 );

    iTi=find( abs(Ndx-Bax(a))<15 & ...
             abs(Ndy-Bay(a))<15 );

    mTi=mNd9;

    conv=mTi/sum( ...
                [Nd08(Tiy(a)-1,tix111(a)-1:tix111(a)+1)...
                 Nd111(tiy111(a) ,tix111(a)-1:tix111(a)+1)...
                 Nd111(tiy111(a)+1,tix111(a)-1:tix111(a)+1)]);
%9 pixels

    iNd=find( abs(Ndx-Bax(a))<15 & ...
             abs(Ndy-Bay(a))<15 );

    s=0;

    for b=1:length(iNd)

        if (ndx111(iNd)==1)
            ndx111(iNd)=2;
        end

        if (ndy111(iNd)==1)
            ndy111(iNd)=2;
        end
    end
end

```

```

    if (ndx111(iNd)==siz(2))
        ndx111(iNd)=siz(2)-1;
    end

    if (ndy111(iNd)==siz(1))
        ndy111(iNd)=siz(1)-1;
    end

    s=s+sum( sum(
        Nd111(ndy111(iNd)-1:ndy111(iNd)+1,...
            ndx111(iNd)-1:ndx111(iNd)+1)));
        %9 pixels

end

peakNd=mean(Ndma9(iNd)/mNd9);
convNd(a)=mTi/peakNd;
rBa_Nd(a)=mTi/(convNd(a)*sum(...
    [Nd08(Bay(a)-1,Bax(a)-1:Bax(a)+1)...
    Nd08(Bay(a) ,Bax(a)-1:Bax(a)+1)...
    Nd08(Bay(a)+1,Bax(a)-1:Bax(a)+1)]));
%scale Nd as well
%Nd scaled up to Ti (9 pixels)

Ba_map(Bax_2(a)-2:Bax_2(a)+2,Bay_2(a)-2:Bay_2(a)+2)=...
    mTi/Ba08(Bay(a),Bax(a))*...
    Ba08(Bay_2(a)-2:Bay_2(a)+2,Bax_2(a)-2:Bax_2(a)+2);
%convert Nd peak to Ti
% 9 adjacent pixels

Nd_map(Bax_2(a)-2:Bax_2(a)+2,Bay_2(a)-2:Bay_2(a)+2)=...
    convNd(a)*...
    Nd08(Bay_2(a)-2:Bay_2(a)+2,Bax_2(a)-2:Bax_2(a)+2);

end

Bam=rot90( Ba_map-min(min(Ba_map)) );
Ndm=rot90( Nd_map-min(min(Nd_map)) );

```

```

mm=max(max([Bam Ndm]));
fig= zeros ([ size(Bam) 3]);
fig (:,:,1)= flipud (Bam/mm);
fig (:,:,3)= flipud (Ndm/mm);
imshow (fig , 'InitialMagnification ', 'fit ')

cont=Ba_map+Nd_map;
figure
contourf (rot90 (cont))
colorbar

figure
imagesc (Nd08)
hold on
plot (Ndx_2,Ndy_2, '.' , 'MarkerSize ',12)
ind=zeros (length (Ndx_2) ,1);

cxy = [];
n = 0; % Loop, picking up the points.

disp ('Central Points ')
disp ('Right mouse button picks last point. ')

but = 1;

while but == 1

    [xi2 ,yi2 ,but] = ginput (1);
    plot (xi2 ,yi2 , 'ko' , 'MarkerSize ',12)
    n = n+1;
    xi2=round (xi2);
    yi2=round (yi2);
    cxy (:,n) = [xi2 ;yi2 ];

end

for a=1:length (cxy)

    i2=find ( abs (Ndx_2-cxy (1,a))<2 & ...
    abs (Ndy_2-cxy (2,a))<2 );
    ind (i2)=2;

```

```

end

disp('Press any button to continue')
pause

% sites 3 4
xy34 = [];
n = 0; % Loop, picking up the points.
disp('Extreme Points, site 3 and 4')

but = 1;
while but == 1

    [x34,y34,but] = ginput(1);
    plot(x34,y34,'ro','MarkerSize',12)
    n = n+1;
    x34=round(x34);
    y34=round(y34);
    xy34(:,n) = [x34;y34];

end

for a=1:length(xy34)

    i34=find( abs(Ndx_2-xy34(1,a))<2 & ...
    abs(Ndy_2-xy34(2,a))<2 );
    ind(i34)=4;

end

disp('Press any button to continue')
pause

% sites 1 5
xy15 = [];
n = 0; % Loop, picking up the points.
disp('Middle Points, site 1 and 5')

but = 1;
while but == 1

```

```

[x15 , y15 , but] = ginput (1);
plot (x15 , y15 , 'go' , 'MarkerSize' , 12)
n = n+1;
x15=round(x15);
y15=round(y15);
xy15 (: , n) = [x15 ; y15 ];

end

for a=1:length(xy15)

    i15=find( abs(Ndx_2-xy15(1 , a))<2 & ...
              abs(Ndy_2-xy15(2 , a))<2 );

ind(i15)=1;

end

l=length(Ndx_2);
pBa=zeros(1 , l);
sBa=zeros(1 , l);
sNd=zeros(1 , l);

for a=1:l

    sBa(a)=sum(sum( ...
                Ba_map(Ndy_2(a)-2:Ndy_2(a)+2 , Ndx_2(a)-2:Ndx_2(a)+2)));

    sNd(a)=sum(sum( ...
                Nd_map(Ndy_2(a)-2:Ndy_2(a)+2 , Ndx_2(a)-2:Ndx_2(a)+2)));

    pBa(a)=sBa(a)/(sNd(a)+sBa(a));

end

ic=find(ind==2);
ie=find(ind==4);
im=find(ind==1);

r1=pBa(im); % ratio for Nd1
r2=pBa(ic); % for Nd2 etc .

```

```
r3=pBa(ie);
```

```
mnd=[mean(r1),mean(r2),mean(r3)];
```

```
snd=[std(r1),std(r2),std(r3)];
```

```
figure
```

```
bar([mnd' snd'],'grouped')
```

```
title('Percentage of Ba in Nd Sites (x=0.3)','fontsize',12)
```

```
xlabel('Nd Sites')
```

```
legend('Percentage','\sigma','fontsize',12,'Location','NorthWest')
```

Bibliography

- [1] Cloutier, S. G., Hybrid Polyfluorene-Based Optoelectronic Devices. In: Fadhali M, editor. *Advanced Photonic Sciences*. Rijeka, Croatia: InTech, 2012. pp. 177
- [2] Sariciftci, N. S., Smilowitz, L., Heeger, A. J., Wudl, F., *Science* 258 (1992) 1474
- [3] Friend, R. H., Gymer, R. W., Holmes, A. B., Burroughes, J. H., Marks, R., Taliani, C., et al., *Nature* 397 (1999) 121
- [4] Kraft, A., Grimsdale, A. C., Holmes, A. B., *Angew Chem Int Ed* 37 (1998) 402
- [5] Bernius, M. T., Inbasekaran, M., O'Brien, J., Wu, W., *Adv Mater* 12 (2000) 1737
- [6] Baeg, K. J., Binda, M., Natali, D., Caironi, M., Noh, Y. Y., *Adv. Mater.* 25 (2013) 4267
- [7] Friend, R. H., Gymer, R. W., Holmes, A. B., Burroughes, J. H., Marks, R. N., Taliani, C., Bradley, D. D. C., Dos Santos, D. A., Bredas, J. L., Lögdlund, M., Salaneck, W. R., *Nature* 397 (1999) 121
- [8] Kalloudis, M., PhD Thesis, University of Edinburgh, 2013
- [9] Shirakawa, H., Louis, E. J., MacDiarmid, A. G., Chiang, C. K., Heeger A. J., *J. Chem. Soc. Chem. Commun.* 579 (1977)
- [10] Chiang, C. K., Fischer, C. R., Park, Y. W., Heeger, A. J., Shirakawa, H., Louis, E. J., Gau, S. C., MacDiarmid, A. G., *Phys. Rev. Lett.* 39 (1977) 1098
- [11] Garnier, F., Hajlaoui, R., Yassar, A., Srivastava, P., *Science* 265 (1994) 1684
- [12] Yang, Y., Heeger, A. J., *Nature* 372 (1994) 344
- [13] Sirringhaus, H., Tessler, N., Friend, R. H., *Science* 280 (1998) 1741
- [14] Gelinck, G., Geuns, T., de Leeuw, D., *Appl. Phys. Lett.* 77 (2000) 14887
- [15] Crone, B., *Nature* 403 (2000) 521
- [16] Burroughes, J. H., Bradley, D. D. C., Brown, A. R., Marks, R. N., Mackay, K., Friend, R. H., Burns, P. L., Holmes, A. B., *Nature* 347 (1990) 539

- [17] Yu, G., Gao, J., Hummelen, J. C., Wudl, F., Heeger, A. J., *Science* 270 (1995) 1789
- [18] Halls, J. J. M., Walsh, C. A., Greenham, N. C., Marseglia, E. A., Friend, R. H., Moratti, S. C., Holmes, A. B., *Nature* 376 (1995) 498
- [19] Brabec, C. J., Sariciftci, S., Hummelen, J. C., *Adv. Funct. Mater.* 11 (2001) 1526
- [20] Grice, A. W., Bradley, D. D. C., Bernius, M. T, Inbasekaran, M., Wu, W. W., Woo, E. P., *Appl. Phys. Lett.* 73 (1998) 5
- [21] Grivas, C, Pollnau, M., *Laser Photonic Rev.* 6 (2012) 419
- [22] McGehee, M. D., Heeger, A. J., *Adv. Mater.* 12 (2000) 1655
- [23] Samuel, I. D. W., Turnbull, G. A., *Chem. Rev.* 107 (2007) 1272
- [24] Tessler, N., *Adv. Mater.* 11 (1999) 363
- [25] Cho, B., Song, S., Ji, Y., Kim, T. W., Lee, T., *Adv. Funct. Mater.* 21 (2011) 2806
- [26] Binda, M., Rottondi, C., Iacchetti, A., Natali, D., Sampietro, M., Beverina, L., “Organic photodetector directly deposited onto the cut end of a plastic optical fiber”, presented at 2012 Symposium on Photonics and Optoelectronics (SOPO), Shanghai, 2012
- [27] Chen, Q., Hajagos, T., Pei, Q., *Annual Reports Section “C” (Physical Chemistry)* 107 (2011) 298
- [28] Binda, M., Natali, D., Sampietro, M., Agostinelli, T., Beverina, L., *Nucl. Instrum. Meth. A* 624 (2010) 443
- [29] Fraboni, B., Ciavatti, A., Merlo, F., Pasquini, L., Cavallini, A., Quaranta, A., Bonfiglio, A., Fraleoni-Morgera, A., *Adv. Mater.* 24 (2012) 2289
- [30] Iacchetti, A., Binda, M., Natali, D., Giussani, M., Beverina, L., Fiorini, C., Peloso, R., Sampietro, M., *IEEE T. Nucl. Sci.* 59 (2012) 1862
- [31] Zhang, Y., Blom, P. W. M., *Appl. Phys. Lett.* 98 (2011) 143504
- [32] Vohra, V., Giovanella, U., Tubino, R., Murata, H., Botta, C., *ACS Nano* 5 (2011) 5572
- [33] Sarasqueta, G., Choudhury, K. R., Subbiah, J., So, F., *Adv. Funct. Mater.* 21 (2011) 167
- [34] G. M. Lazzerini, G. M., Di Stasio, F., Fléchon, C., Caruana, D. J., Cacialli, F., *Appl. Phys. Lett.* 99 (2011) 243305

- [35] Bhattacharyya, S., Patra, A., *Journal of Photochemistry and Photobiology C: Photochemistry Reviews* 20 (2014) 51
- [36] Szymanski, C., Wu, C., Hooper, J., Salazar, M.A., Perdomo, A., Dukes, A., McNeill, J., *J. Phys. Chem. B* 109 (2005) 8543
- [37] Pecher, J., Mecking, S., *Macromolecules* 40 (2007) 7733
- [38] Ong, B.S., Wu, Y., Liu, P., Gardner, S., *Adv. Mater.* 17 (2005) 1141
- [39] Wang, F., Han, M.Y., Mya, K.Y., Wang, Y., Lai, Y.H., *J. Am. Chem. Soc.* 127 (2005) 10350
- [40] Bawendi, M. G., Steigerwald, M. L., Brus, L. E., *Annu.Rev. Phys. Chem.* 41 (1990) 477
- [41] Tomczak, N., Janczewska, D., Hana, M., Vancso, G. J., *Progress in Polymer Science* 34 (2009) 393
- [42] Brus, L.E., *J Chem Phys* 79 (1983) 5566
- [43] Brus, L.E., *J Chem Phys* 80 (1984) 4403
- [44] Efros, A.L., Rosen, M., *Annu Rev Mater Sci* 30 (2000) 475
- [45] Brus, L.E., *J Phys Chem* 90 (1986) 2555
- [46] Chen, G., Seo, J., Yang, C., Prasad, P.N., *Chem. Soc. Rev.* 42 (2013) 8304
- [47] Vijayakumar, C., Balan, B., Saeki, A., Tsuda, T., Kuwabata, S., Seki, S., *J. Phys. Chem. C* 116 (2012) 17343
- [48] Lee, J., Sundar, V.C., Heine, J.R., Bawendi, M.G., Jensen, K.F., *Adv Mater* 12 (2000) 1102
- [49] Coe, S., Woo, W. K., Bawendi, M., Bulovic, V., *Nature* 420 (2002) 800
- [50] Coe, S., Woo, W. K., Bawendi, M., Bulovic, V., *Nature* 420 (2002) 6917
- [51] Wang, Y., Herron, N., *J Lumin* 70 (1996) 48
- [52] Goodman, M. D., Xu, J., Wang, J., Lin, Z., *Chemistry of Materials* 21(2009) 5
- [53] Gur, I., Fromer, N. A., Geier, M. L., Alivisatos, A. P., *Science* 310 (2005) 5747
- [54] Vanderah, T. A., *Science* 298 (2002) 1182
- [55] Richtmyer, R. D., *J. Appl. Phys.*, 10 (1939) 391
- [56] Mongia, R. K., Bhartia, P., *International Journal of Microwave and Millimeter-Wave Computer-Aided Engineering* 4 (1994) 3

- [57] Stenzel, O., *Optical Coatings*. Springer Series in Surface Sciences Volume 54. Springer-Verlag Berlin Heidelberg 2014
- [58] Reaney, I. M., Iddles, D., *J. Am. Ceram. Soc.*, 89 (2006) 7
- [59] Freer, R., Azough, F., *Journal of the European Ceramic Society* 28 (2008) 1433
- [60] Wakino, K., Murata, M. and Tamura, H., *J. Am. Ceram. Soc.* 69 (1986) 34
- [61] Ohsato, H., *J. Ceram. Soc. Jpn.*, 113 (2005) 11
- [62] Kawashima, S., Nishida, J., Ueda, J., Ouchi, H., *J. Am. Ceram. Soc.* 66 (1983) 6
- [63] Tamura, H., Konoike, Y. T., Sakabe, Y., Wakino, K., *J. Am. Ceram. Soc.* 67 (1984) 4
- [64] Matsumoto, K., Hiuga, T., Takeda, K., Ichimura, H., Ba(Mg^{1/3} Ta^{2/3})O₃ ceramics with ultra low loss at microwave frequencies. In *Proceedings of the Sixth IEEE International Symposium on Application of Ferroelectrics*, 1986, pp. 118–121.
- [65] Wakino, K., Murata, M., Tamura, H., *J. Am. Ceram. Soc.* 69 (1986) 34
- [66] Tang, C.C., Roberts, M. A., Azough, F., Leach, C., and Freer, R., *J. Mater. Res.* 17 (2002) 3
- [67] Andrews, K.W., Dyson, D. J., Keown, S. R., *Interpretation of Electron Diffraction Patterns* 2nd Ed. (1971) Plenum Press, New York
- [68] Chapman, J. N., Johnston, A. B., Heyderman, L. J., McVitie, S., Nicholson, W. A. P., *IEEE Trans. Magn.* 30 (1994) 4479
- [69] Williams, D. B., Carter, C. B. “*Transmission Electron Microscopy*” Springer 1996 ISBN: 978-0-387-76500-6
- [70] Egerton, R.F. “*Electron Energy-Loss Spectroscopy in the Electron Microscope*” Springer 2011 ISBN: 978-1-4419-9582-7
- [71] Crewe, A. V., Wall, J., Welter, L. M., *J. Appl. Phys.*, 39 (1968) 13
- [72] Crewe, A. V., *Science*, 154 (1966) 3750
- [73] MacLaren, I., Wang, L.Q., Morris, O., Craven, A. J., Stamps, R. L., Schaffer, B., Ramasse, Q. M., Miao, S., Kalantari, K., Sterianou, I., Reaney I. M., *APL Mater.* 1 (2013) 021102
- [74] Busch, H., *Arch. Elektro-tech.* 18 (1927) 583
- [75] Crewe, A.V. “*High Intensity Electron Sources and Scanning Electron Microscopy*” in U. Valdre (ed.) *Electron Microscopy in Material Science*, Academic Press. 1971

- [76] Knoll, M., Ruska, E., *Z. Phys.*, 78 (1932) 5
- [77] Lord Rayleigh F. R. S., *Philosophical Magazine Series 8* (1879) 261
- [78] Goodhew, P. et al. "Aberration-Corrected Analytical Transmission Electron Microscopy" John Wiley & Sons 2011 ISBN: 978-0-470-51851-9
- [79] Scherzer, O., *Zeitschrift für Physik* 101 (1936) 5
- [80] Scherzer, O., *Journal of Applied Physics* 3 (1948) 8
- [81] Krivanek O.L. et al., *Ultramicroscopy*, 78 (1999) 1
- [82] Haider, M., Braunshausen, G., Schwan, E. *Optik (Jena)* 99 (1995) 4
- [83] Nion Company, Kirkland, WA, USA. nion.com
- [84] CEOS GmbH, Heidelberg, Germany. <http://www.ceos-gmbh.de/>
- [85] Hawkes, P.W., Kasper, E. in: *Principles of Electron Optics*, Vol. 2, Academic Press, London and San Diego, Ch. 41. 1996
- [86] Beck, V.D., *Optik*, 53 (1979) 241
- [87] Rose, H., *Nucl. Inst. & Methods*, 187 (1981) 187
- [88] Haider, M. et al. *Nature*, 392 (1998) 768
- [89] Scherzer, O., *Optik* 2 (1947) 114
- [90] Jenkins, M. L., and Kirk, M. A. "Characterization of Radiation Damage by Electron Microscopy" IOP Series Microscopy in Materials Science, Institute of Physics, Bristol. 2001 ISBN: 0 7503 0748 X.
- [91] Wentzel, G., *Z. Phys.*, 36 (1927) 574
- [92] Lenz, F. Zur Streuung mittelschneller Elektronen in kleinste Winkel. *Z. Naturforsch.* 9A (1954) 185
- [93] Howie, A., *Journal of Microscopy*, 117 (1979) 11
- [94] Tracey, M. M. J., Howie, A., *Journal of Catalysis* 63 (1980) 1
- [95] Pennycook, S. J., Jesson, D. E., *Phys. Rev. Lett.* 64 (1990) 938
- [96] Pines, D., *Elementary Excitations in Solids*, Benjamin, New York, NY. (1963)
- [97] Nelayah, J., Kociak, M., Stephan, O., Garcia de Abajo, F. J., Tence, M., Henrard, L., Taverna, D., Pastoriza-Santos, I., Liz-Marzan, L. M., and Colliex, C., *Nat. Phys.* 3 (2007) 348

- [98] Williams, D. B., and Edington, J. W., *J. Microsc.* 108 (1976) 113
- [99] Inokuti, M., *Review of Modern Physics* 43 (1971) 3
- [100] Williams, B. G., Sparrow, T. G., and Egerton, R. F., *Proc. R. Soc. Lond.* A393 (1984) 409
- [101] Slater, J. C., *Phys. Rev.* 36 (1930) 57
- [102] Slater, J. C., *Phys. Rev.* 81 (1951) 385
- [103] Mele, E. J., Ritsko, J. J., *Phys. Rev. Lett.* 43 (1979) 68
- [104] Leapman, R. D., Fejes, P. L., and Silcox, J., *Phys. Rev. B* 28 (1983) 2361
- [105] Dirac, P. A. M., *Proceedings of the Royal Society A* 114 (1927) 243
- [106] Manson, S. T., and Cooper, J. W., *Phys. Rev.* 165 (1968) 126
- [107] Leapman, R. D., Grunes, L. A., and Fejes, P. L., *Phys. Rev. B* 26 (1982) 614
- [108] Grunes, L. A., *Phys. Rev. B* 27 (1983) 2111
- [109] Heine, V., *Solid State Phys.* 35 (1980) 1
- [110] Glen, G. L., Dodd, C. G., *J. Appl. Phys.* 39 (1968) 5372
- [111] Lazar, S., Botton, G. A., Wu, M.-Y., Tichelaar, F. D., Zandbergen, H. W., *Ultramicroscopy* 96 (2003) 535
- [112] Kothleitner, G., and Hofer, F., *Micron* 34 (2003) 211
- [113] Manson, S. T., *Phys. Rev. A* 6 (1972) 1013
- [114] Leapman, R. D., Rez, P., Mayers, D. F., *J. Chem. Phys.* 72 (1980) 1232
- [115] Weng, X., Rez, P., *Ultramicroscopy* 25 (1988) 345
- [116] Egerton, R. F., *Ultramicroscopy* 3 (1978) 243
- [117] Craven, A. J., Buggy, T. W., Ferrier, R. P., Post-specimen lenses in electron spectroscopy. In *Quantitative Microanalysis with High Spatial Resolution*, The Metals Society, London 1981 pp. 3–6.
- [118] Warusawithana, M. P., Richter, C., Mundy, J. A., Roy, P., Ludwig, J., Paetel, S., Heeg, T., Pawlicki, A. A., Kourkoutis, L. F., Zheng, M., Lee, M., Mulcahy, B., Zander, W., Zhu, Y., Schubert, J., Eckstein, J. N., Muller, D. A., Hellberg, C. S., Mannhart, J., Schlom, D. G., *Nat. Commun.* 4 (2013) 9
- [119] Forbes, B. D., D'Alfonso, A. J., Williams, R. E. A., Srinivasan, R., Fraser, H. L., McComb, D. W., Freitag, B., Klenov, D. O., Allen, L. J., *Phys. Rev. B* 86 (2012) 024108

- [120] Forbes, B. D., D'Alfonso, A. J., Williams, R. E. A., Srinivasan, R., Fraser, H. L., McComb, D. W., Freitag, B., Klenov, D. O., Allen, L. J., Phys. Rev. B 86 (2012) 024108 Pennycook, S. J., Ultramicroscopy 26 (1988) 239
- [121] Robb, P. D., Finnie, M., Longo, P., Craven, A. J., Ultramicroscopy 114 (2012) 11
- [122] Varela, M., Findlay, S. D., Lupini, A. R., Christen, H. M., Borisevich, A. Y., Dellby, N., Krivanek, O. L., Nellist, P. D., Oxley, M. P., Allen, L. J., Pennycook S. J., Phys. Rev. Lett. 92 (2004) 9
- [123] <http://www.er-c.org/barthel/drprobe>
- [124] Lifshitz, M. A., Gaussian Random Functions, Kluwer Academic Publishers Group, Dordrecht, The Netherlands
- [125] Le Cam, L., Statist. Sci. 1 (1986) 78
- [126] Browning, N. D., Chisholm, M. F., Pennycook, S. J., Norton, D. P., Lowndes, D. H., Physica C 212 (1993) 1–2
- [127] McGibbon, M. M., Browning, N. D., Chisholm, M. F., McGibbon, A. J., Pennycook, S. J., Ravikumar, V., Dravid, V. P., Science 266 (1994) 5182
- [128] MacLaren, I., Ramasse, Q. M., International Materials Reviews 59 (2014) 3
- [129] MacLaren, I., Wang, Z. L., Wang, H. S., Li, Q., Appl. Phys. Lett. 80 (2002) 8
- [130] Houben, L., Thust, A., Urban, K., Ultramicroscopy 106 (2006) 3
- [131] MacLaren, I., Villaurrutia, R., Schaffer, B., Houben, L., Peláiz-Barranco, A., Adv. Funct. Mater. 22 (2012) 261
- [132] L. Houben, "iMtools imaging processing software," <http://www.er-c.org/centre/software/imtools.htm>, 2009
- [133] Choi, E.M., Fix, T., Kursumovic, A., Kinane, C. J., Arena, D., Sahonta, S. L., Bi, Z., Xiong, J., Yan, L., Lee, J. S., Wang, H., Langridge, S., Kim, Y. M., Borisevich, A. Y., MacLaren, I., Ramasse, Q. M., Blamire, M. G., Jia, Q., MacManus-Driscoll, J. L., Adv. Funct. Mater. 00 (2014) 1, manuscript in preparation
- [134] F. Azough, F., Cernik, R. Freer, R., Bigatti, M., MacLaren, I., Barthel, J., Schaffer, B., Ramasse, Q.M., Kepaptsoglou, D.M., Journal of the American Ceramic Society (2015) manuscript in preparation
- [135] EELS Analysis user manual v. 2.3.0 Gatan Inc. 2013
- [136] Ahn, C.C., Rez, P., Ultramicroscopy 17 (1985) 105

- [137] Hofer, F., *Microsc. Microanal. Microstruct.*, 2[2-3] (1991) 215
- [138] MacLaren, I., Schierholz, R., Trusty, P. A., Ponton, C. B., *J. Am. Ceram. Soc.*, 90 (2007) 10
- [139] Bach, D., Schneider, R., Gerthsen, D., *Microsc. Microanal.* 15 (2009) 524
- [140] Dwyer, C., Erni, R., and Etheridge, J., *Ultramicroscopy* 110 (2010) 952
- [141] Bar-Sadan, M., Barthel, J., Shtrikman, H., Houben, L., *Nano Lett.* 12 (2012) 2352
- [142] <http://www.er-c.org/barthel/drprobe/BNTO4/>
- [143] Mott, N. F., Massey, H. S. W., *The Theory of Atomic Collisions* Oxford University Press Oxford 1965
- [144] Green, M., Cosslett, V.E., *Proc. Phys. Soc.* 78 (1961) 1206
- [145] Powell, C. J., *Evaluation of Formulas for Inner-shell Ionization Cross Sections in Use of Monte Carlo Calculations in Electron Probe Analysis and Scanning Electron Microscopy* 97–104 NBS Special Publication 460 Eds. KFJ Heinrich, DE Newbury and H Yakowitz U.S. Department of Commerce/NBS Washington DC. 1976
- [146] Powell, C. J., *Evaluation of formulas for inner-shell ionization cross sections.* Tech. Report Special Publication 460, pp. 97-104. NBS. 1976
- [147] Schreiber, T. P., and Wims, A. M., *Relative Intensity Factors for K, L and M Shell X-ray Lines* *X-ray Spectrometry* 11 42–45. 1982
- [148] Zaluzec, N. J., *Quantitative X-ray Microanalysis: Instrumental Considerations and Applications to Materials Science in Introduction to Analytical Electron Microscopy* Eds. JJ Hren JJ Goldstein and DC Joy 121–167 Plenum Press NY. 1979
- [149] Colvin, V. L., Schlamp, C., Alivisatos, A. P., *Nature* 370 (1994) 6488
- [150] Dabbousi, B. O., Bawendi, M. G., *Appl. Phys. Lett.* 66 (1995) 11
- [151] Tessler, N., Medvedev, V., Kazes, M., Kan, S., Banin, U., *Science* 295 (2002) 5559
- [152] Koktysh, D. S., Gaponik, N., Reufer, M., Crewett, J., Scherf, U., Eychmüller, A., Lupton, J. M., Rogach, A. L., Feldmann, J., *ChemPhysChem* 5 (2004) 9
- [153] Huynh, W. U., Dittmer, J. J., Alivatos, A. P., *Science* 295 (2002)
- [154] Campbell, I. H., Crone, B. K., *Adv. Mat.* 18 (2006) 1

- [155] McDonald, S. A., Konstantatos, G., Zhang, S., Cyr, P. W., Klem, E. J. D., Levina, L., Sargent, E. H., *Nat Mater* 4 (2005) 2
- [156] Maria, S. B., Susha, A. S., Sommer, M., Talapin, D. V., Rogach, A. L., Thelakkat. M., *Macromolecules* 41 (2008) 16
- [157] Jiang, G., Susha, A. S., Lutich, A. A., Stefani, F. D., Feldmann, J., Rogach, A. L., *ACS Nano* 3 (2009) 12
- [158] Wang, P., Abrusci, A., Wong, H. M. P., Svensson, M., Andersson, M. R., Greenham, N. C., *Nano Letters* 6 (2008) 8
- [159] Moons, E., *Journal of Physics: Condensed Matter* 14 (2002) 47
- [160] Kim, J. S., Ho, P. K. H., Murphy, C. E., Friend, R. H., *Macromolecules* 37 (2004) 8
- [161] Yim, K.-H., Doherty, W. J., Salaneck, W. R., Murphy, C. E., Friend, R. H., Kim, J.-S., *Nano Letters* 10 (2010) 2
- [162] McNeill, C. R., Greenham, N. C., *Adv. Mat* 21 (2009) 38
- [163] Barlow, I. A., Kreouzis, T., Lidzey, T. G., *Appl. Phys. Lett.* 94 (2009) 243301
- [164] Ma, X., Xu, F., Cloutier, S. G., *Ieee, High-performances 1550 nm polymer-based LEDs on silicon using hybrid polyfluorene-based type-II heterojunctions*. In 2010 "7th Ieee International Conference on Group IV Photonics", Ieee, New York, 2010, p.4
- [165] Cina, S., Baynes, N., Moons, E., Friend, R. H., Burroughes, J., Towns, C., Heeks, K., O'Dell, R., O'Connor, S., Athanassopoulou, N., New, efficient light emitting polymer diode for flat panel display applications. In *Organic and Photonic Materials and Devices III*, Kippelen, B., Bradley, D. D. C., Eds. *Spie-Int Soc Optical Engineering: Bellingham*, 2001; Vol 4279 p. 221
- [166] Cina, S., *Materials Research Society Spring Conference (MRS 2001)*, San Francisco, CA, *MRS Symposium Proceedings: San Francisco, Ca*, 2001
- [167] Morteani, A., Dhoot, A., Kim, J. S., Silva, C., Greenham, N., Murphy, C., Moons, E., Cina, S., Burroughes, J., Friend, R., *Advanced Materials* 15 (2003) 20
- [168] Kim, J. S., Ho, P. K. H., Murphy, C. E., Baynes, N., Friend, R. H., *Advanced Materials* 14 (2002) 3
- [169] Moons, E., *Symposium on New Developments in Display Applications*, Oxford: RAL Laboratory, Oxford: RAL Laboratory 2000
- [170] Greenham, N. C., Peng, X., Alivisatos, A. P., *Physical Review B* 54 (1996) 24

- [171] Ginger, D. S., Greenham, N. C., *Physical Review B* 59 (1999) 16
- [172] Rehm, J. M., McLendon, G. L., Nagasawa, Y., Yoshihara, K., Moser, J., Grätzel, M., *The Journal of Physical Chemistry* 100 (1996) 23
- [173] Huynh, W. U., Dittmer, J. J., Alivisatos, A. P., *Science* 295 (2002) 5564
- [174] Tanaka, H., Lovinger, A. J., Davis, D. D., *Phys. Rev. Lett.* 72 (1994) 16
- [175] Balazs, A. C., Ginzburg, V. V., Qiu, F., Peng, G., Jasnow, D., *Journal of Physical Chemistry B* 104 (2000) 15
- [176] Chung, H.-J., Taubert, A., Deshmukh, R. D., Composto, R. J., *Europhys. Lett.* 68 (2004) 2
- [177] Yurekli, K., Karim, A., Amis, E. J., Krisnamoorti, R., *Macromolecules* 36 (2003) 19
- [178] <http://gwyddion.net/>
- [179] Valant, M., Suvorov, D., Hoffmann, C., Sommariva, H., *J. Eur. Ceram. Soc.* 21 (2001) 2647
- [180] Wakino, K., Minai, K., Tamura, H., *J. Am. Ceram. Soc.* 67 (1984) 278
- [181] Kawashima, S., Nishida, J., Ueda, J., Ouch, H., *J. Am. Ceram. Soc.* 66(6) (1983) 421
- [182] Tamura, H., Konoike, Y. T., Sakabe, Y., Wakino, K., *J. Am. Ceram. Soc.* 67(4) (1984) C59
- [183] Matsumoto, K., Hiuga, T., Takeda, K., Ichimura, H., Ba(Mg_{1/3}Ta_{2/3})O₃ ceramics with ultra low loss at microwave frequencies. In *Proceedings of the Sixth IEEE International Symposium on Application of Ferroelectrics*, 1986, pp. 118
- [184] Azough, F., Freer, R., Microstructural development and microwave dielectric properties of ZrTiO₄-based ceramics. In *Proceedings of the Seventh IEEE International Symposium on Applications of Ferroelectrics*, 1990. IEEE, Piscataway, NJ, 1991, pp. 198
- [185] Glazer, A. M., *Acta Cryst.* B28 (1972) 3384
- [186] Colla, E. L., Reaney, I. M., Setter, N., *J. Appl. Phys.* 74 [5] (1993) 3414
- [187] Reaney, I. M., Colla, E. L., Setter, N., *Jpn. J. Appl. Phys.* 33 [7A] (1994) 3984
- [188] Zheng, H., Reaney, I. M., Muir, D., Price, T., Iddles, D. M., *Jpn. J. Appl. Phys.* 44 [5A] (2005) 3087
- [189] Ohsato, H., *J. European Ceram. Soc.* 21[15] (2001) 2703

- [190] Ubic, R., Reaney, I. M., Lee, W. E., *Int. Mater. Rev.* 43[5] (1998) 205
- [191] Fiedziuszko, S. J., Hunter, I. C., Itoh, T., Kobayashi, Y., Nishikawa, T., Stitzer, S. N., Wakino, K., *IEEE Transactions on Microwave Theory and Techniques*, 50 (2002) 3
- [192] Nishikawa, T., *Trans. Inst. Electron. Inf. Commun. Eng.* E 74 (1991) 6
- [193] Miyake, H., Kitazawa, S., Ishizaki, T., Yamada, T., Nagatomi, Y., "A miniaturized dual band filter using ceramic lamination technique for dual mode portable telephones," in *IEEE MTT-S Int. Microwave Symp. Dig.*, 1997.
- [194] Bailey, A., Foley, W., Hageman, M., Murray, C., Piloto, A., Sparks, K., Zaki, K., "Miniature LTCC filters for digital receivers," in *IEEE MTT-S Int. Microwave Symp. Dig.*, vol. 2, 1997.
- [195] Ishizaki, T., Yamada, T., Miyake, H., "A first practical model of very small and low insertion loss laminated duplexer using LTCC suitable for W-CDMA portable telephones," in *IEEE MTT-S Int. Microwave Symp. Dig.*, vol. 2, 2000.
- [196] Bolton, R. L., "Temperature Compensating Ceramics Capacitors in the System Baria-Rare-earth-oxide Titania," pp. Pages, PhD Thesis, University of Illinois, 1968
- [197] Kolar, D., Stadler, Z., Gaberscek, S., Suvorov, D., *Berichte der Deutschen Keramischen Gesellschaft* 55 (1978) 346
- [198] Kolar, D., Gaberscek, S., Volavsek, B., Parker, H. S., Roth, R. S., *Journal of Solid State Chemistry* 38[2] (1981) 158
- [199] Razgon, E. S., Gens, A. M., Varfolomeev, M. B., Korovin, S. S., Kostomarov, V. S., *Zhurnal Neorg. Khimii* 25[6] (1980) 1701
- [200] Razgon, E. S., Gens, A. M., Varfolomeev, M. B., Korovin, S. S., Kostomarov, V. S., *Zhurnal Neorg. Khimii* 25[8] (1980) 2298
- [201] Takahashi, J., Ikegami, T., Kageyama, K., *J. Am. Ceram. Soc.* 74[8] (1991) 1868
- [202] Takahashi, J., Ikegami, T., Kageyama, K., *J. Am. Ceram. Soc.* 74[8] (1991) 1873
- [203] Jaakola, T., Uusimaki, A., Rautioaho, R., Leppavuori, S., *J. Am. Ceram. Soc.* 69[10] (1986) C234
- [204] Valant, M., Suvorov, D., Kolar, D., *Jpn. J. Appl. Phys. Part 1* 35[1A] (1996) 144
- [205] Suvorov, D., Valant, M., Kolar, D., *J. Mater. Sci.* 32[24] (1997) 6483
- [206] Varfolomeev, M. B., Mironov, A. S., Kostomarov, V. S., Golubtsova, L. A., Zolotova, T. A., *Zhurnal Neorg. Khimii* 33[4] (1988) 1070

- [207] Ohsato, H., Ohhashi, T., Nishigaki, S., Okuda, T., Sumiya, K., Suzuki, S., *Jpn. J. Appl. Phys. Part 1* 32[9B] (1993) 4323
- [208] Matveeva, R. G., Varfolomeev, M. B., Ilyushchenko, L. S., *Zhurnal Neorg. Khimii* 29[1] (1984) 31
- [209] Rawn, C. J., In *Electroceramics V*; Baptista, J. L., Labrincha, J. A., Vilarinho, P. M., Eds.; European Ceramic Society: Aveiro, Portugal, 1996; Vol. 2, p 67
- [210] <http://it.iucr.org/Ab/ch7o1v0001/sgtable7o1o062/>
- [211] Rawn, J., Birnie, D. P., Bruck, M. A., Enemark, J. H., Roth, R. S., *J. Mater. Res.* 13[1] (1998) 187
- [212] Okudera, H., Nakamura, H., Toraya, H., Ohsato, H., *Journal of Solid State Chemistry* 142 (1999) 336
- [213] MacLaren, I., Villaurrutia, R., Schaffer, B., Houben, L., Pelaiz-Barranco, A., *Adv. Func. Mater.* 22[2] (2012) 261
- [214] MacLaren, I., Wang, L. Q., Schaffer, B., Ramasse, Q. M., Craven, A. J., Selbach, S. M., Spaldin, N. A., Miao, S., Kalantari, K., Reaney, I. M., *Adv. Func. Mater.* 23[6] (2013) 683
- [215] MacLaren, I., Wang, L. Q., Morris, O., Craven, A. J., Stamps, R. L., Schaffer, B., Ramasse, Q. M., Miao, S., Kalantari, K., I., Sterianou, I., Reaney, I. M., *APL Materials* 1[2] (2013)
- [216] Gorla, C. R. , Emanetoglu, N. W., Liang, S., Mayo, W. E., Lu, Wraback, M., Shen, H., *J. Appl. Phys.* 85 (1999) 2595
- [217] Kim, K. H., Park, K. C., Ma D. Y., *J. Appl. Phys.* 81 (1997) 7764
- [218] Yang, G. Y., Dickey, E. C., Randall, C. A., Barber, D. E., Pinceloup, P., Henderson, M. A., Hill, R. A., Beeson, J. J., Skamser, D. J., *J. Appl. Phys.* 96 (2004) 7492
- [219] <http://www.mathworks.com/matlabcentral/fileexchange/22216-ploterr>